PNNL-14619

Pacific Northwest
National Laboratory
Operated by Battelle for the
U.S. Department of Energy

Microphysical Properties of Single And Mixed-Phase Arctic Clouds Derived From Ground-Based Aeri Observations

DD Turner

June 2003

Prepared for the U.S. Department of Energy
under Contract DE-AC06-76RL01830

DISCLAIMER

PACIFIC NORTHWEST NATIONAL LABORATORY
operated by
BATTELLE
for the
UNITED STATES DEPARTMENT OF ENERGY
under Contract DE-AC06-76RL01830

Printed in the United States of America

Available to DOE and DOE contractors from the
Office of Scientific and Technical Information,
P.O. Box 62, Oak Ridge, TN 37831-0062;
ph: (865) 576-8401
fax: (865) 576-5728
email: reports@adonis.osti.gov

Available to the public from the National Technical Information Service,
U.S. Department of Commerce, 5285 Port Royal Rd., Springfield, VA 22161
ph: (800) 553-6847
fax: (703) 605-6900
email: orders@ntis.fedworld.gov
online ordering: http://www.ntis.gov/ordering.htm


This document was printed on recycled paper.
(8/00)

MICROPHYSICAL PROPERTIES OF SINGLE AND MIXED-PHASE ARCTIC CLOUDS DERIVED FROM GROUND-BASED AERI OBSERVATIONS

by

David D. Turner

A dissertation submitted in partial fulfillment of the

requirements for the degree of

Doctor of Philosophy

(Atmospheric and Oceanic Sciences)

at the

UNIVERSITY OF WISCONSIN - MADISON

2003

MICROPHYSICAL PROPERTIES OF SINGLE AND MIXED-PHASE ARCTIC CLOUDS DERIVED FROM GROUND-BASED AERI OBSERVATIONS

David D. Turner

Under the supervision of Professor Steve A. Ackerman

At the University of Wisconsin - Madison

Abstract

A novel new approach to retrieve microphysical properties from mixed-phase clouds is presented. This algorithm retrieves cloud optical depth, ice fraction, and the effective size of the water and ice particles from ground-based, high-resolution infrared radiance observations. The theoretical basis is that the absorption coefficient of ice is greater than that of liquid water from 10-13 μm, whereas liquid water is more absorbing than ice from 16-25 μm. However, due to the strong absorption of water vapor in the rotational absorption band, the 16-25 μm spectral region becomes opaque for significant water vapor burdens (i.e., for precipitable water vapor over approximately 1 cm). The Arctic is characterized by its dry and cold atmosphere, as well as a preponderance of mixed-phase clouds, and thus this approach is applicable to Arctic clouds. Since this approach uses infrared observations, cloud properties

are retrieved at night and during the long polar wintertime period as well as during daytime periods.

The interactions among the clouds, atmosphere, and surface in the Arctic are extremely complex, and these interactions are less understood than at mid-latitudes. This lack of understanding is due to the small number of observations of cloud properties in the Arctic, which is primarily due to the difficulty in detecting and retrieving cloud properties from space. The retrieval algorithm developed here offers the necessary data set to study the interactions of the clouds with the surface and atmosphere and to validate existing and new satellite remote sensing techniques, especially during the polar winter. As an example, frequency distributions of the cloud properties retrieved during a 7 month Arctic experiment demonstrate many interesting features of Arctic clouds. These results demonstrate that approximately 50% of the clouds are mixed-phase, a lack of temperature dependence in the ice fraction for temperatures above 240 K, seasonal trends in the optical depth with the clouds being thinner in winter and becoming more optically thick in the late spring, and a seasonal trend in the effective size of the water droplets in liquid-only and mixed-phase clouds that is most likely related to aerosol concentration.

Acknowledgments

No one exists in a vacuum, and that is certainly true here. A great many people provided motivation, guidance, wisdom, and humor as I worked on this dissertation. The scientific objectives of the Department of Energy's Atmospheric Radiation Measurement (ARM) program provided the initial motivation for this research, and the support by the scientists, engineers, and staff in the ARM program has been tremendous. In particular, I would like to thank Tom Ackerman and Ted Cress for their enthusiasm and support that made my educational leave of absence from Pacific Northwest National Laboratory (PNNL) a reality. The Climate Physics group at PNNL, and especially Connor Flynn, are greatly appreciated for shouldering many extra tasks and projects that I was responsible for before I left on leave. Thank you all!

The energy and passion I found in the high spectral resolution group at the University of Wisconsin-Madison is outstanding. Hank Revercomb, Bob Knuteson, Dave Tobin, and Wayne Feltz played a significant role in my professional development, and I am glad to be able to count them among my friends. They gladly worked with me on a variety of AERI issues, but more importantly, they were an excellent example of how one should balance career and life.

A part of obtaining an advanced degree is learning, and there are too many people to list who assisted me in that process. However, I would like to thank Steve Ackerman for his time, energy, and talents in this journey, as I have greatly benefited from our many conversations. I would also like to thank Grant Petty and Allen Huang for helping me understand the intricacies of optimal estimation and how to correctly compute the covariance matrices required for this technique. Bryan Baum has also played a special role with his interest and forward thinking, forcing me to think about my research goals down the road.

This thesis utilized many data sets from different sources. The AERI data were collected as part of the ARM program during SHEBA, and the many fine folks who installed and maintained the instrument during that experiment deserve a hand on the back. Wayne Feltz downloaded radiosonde data from the JOSS archive, and his initial quality control was greatly appreciated. Janet Intrieri provided the high-resolution DABUL backscatter and

depolarization data and several helpful discussions regarding its interpretation. Matthew Shupe provided a wealth of data in the form of several different millimeter cloud radar retrievals of liquid and ice water paths for several case studies in Chapter 8. I look forward to working with Matthew more when the North Slope of Alaska data are processed with both of our algorithms. Xiquan Dong also provided results from his microphysical retrieval algorithm, as well as aircraft data, for a case study in a liquid water cloud that was particularly useful. Steve Vavrus modified the GENESIS climate model to use a stochastic routine for cloud phase based upon this work for which I am very grateful. Finally, Ping Yang enthusiastically provided the scattering properties from realistically shaped ice particles, and I look forward to continuing to work with Ping in the future. I am very appreciative of the efforts by all of these fine scientists.

Life without family and loved ones would not be life, and therefore I want to extend a thank you to those who have made my existence special. My parents, Dennis and Elaine Turner, provided a foundation upon which all else was built, and I want to thank you for the upbringing I had, the values you instilled in me at an early age, and the love that I feel every day. I could not ask for better parent-in-laws than George and Shirley Alexander, and I want to thank you for the support and love you have offered us during this journey. Our boys Jesse, Jack, and Jimmy have provided boundless joy and zeal for learning, and even at their young age deserve a thank you for helping keep me centered on what is important in life. And finally, my wife Shana deserves a tremendous thank you for her spirit, support, and guidance through this process. She is the glue that has held it all together.

This work was conducted as part of the ARM program. Funding for this research was provided via grants to the University of Wisconsin-Madison by the ARM program and from PNNL.

Table of Contents

List of Tables

List of Figures

Chapter 1

1. Introduction

When the Earth is viewed from space, the awesome complexity and variability of clouds is apparent. Clouds come in a variety of shapes, sizes, and textures, and are a visible signature of the weather on Earth. For centuries, humankind has looked at clouds as an indication of the current weather and the weather to come, as well as a source of beauty and inspiration.

Clouds are more than just one component of the weather, but also play a critical role in the climate of the Earth. Depending on its height and composition, a cloud can have a cooling effect by reflecting back to space the incoming solar energy or a warming effect by trapping infrared energy emitted by the Earth system. The role of clouds in climate and weather and the large variability among different cloud types have occupied thousands of scientists for hundreds of years.

Clouds are extremely complex. To make the problem tractable, scientists began by studying "simple" clouds; clouds that consist of only water or only ice (i.e., single-phase clouds), clouds that are "homogeneous" in time and/or space, clouds that are close to the surface, et cetera. In situ and remotely sensed data from these clouds provide the basis from which scientific understanding can be developed. The need for data has led to a host of experiments and measurement campaigns to gather data in clouds in various locations.

Naturally, there are many different sorts of clouds that are difficult to observe, and thus the knowledge of how these types of clouds impact the climate or weather is not as advanced as for clouds that are easier to sample. Clouds that have proven difficult to study

include high cirrus clouds (especially in the tropics where the cirrus can extend as high as 18 km above the Earth's surface) and polar clouds. The former is difficult to study because of the challenge of obtaining in situ observations in these clouds, the latter because of the presence of surface ice, persistent temperature inversions near the surface, and the relative thinness of the polar clouds makes them difficult to detect from satellite. Clouds that are of mixed-phase, i.e., clouds that are composed of both water droplets and ice crystals, are also not well observed. This is because of the inherent difficulties in gathering in situ observations in these types of clouds as well as the lack of remote sensing techniques to measure and characterize mixed-phase cloud properties.

In this dissertation, a new approach is developed to retrieve cloud properties from both single and mixed-phase clouds in the Arctic from infrared radiance observations. Chapter 2 starts with a review of Arctic clouds, discussing the role of these clouds in the Earth's climate and the difficulties in observing them. The importance of mixed-phase clouds and the role of aerosols in Arctic clouds are discussed. A review of different techniques used to retrieve the properties of mixed-phase clouds is also presented. The chapter ends by outlining three objectives of this research effort. An overview of the instrumentation used in this study is presented in Chapter 3. Chapter 4 provides a summary of the current state-of-the-art in clear sky infrared radiative transfer, which is a prerequisite to performing radiative transfer in cloudy skies. Chapter 4 outlines recent improvements to the radiation models and discussing some of the remaining issues that are still being addressed for clear skies. Chapter 5 discusses how clouds are modeled in the infrared, especially mixed-phase clouds. Chapter 6 demonstrates how cloud phase can be unambiguously determined from ground-based infrared radiance observations between 8 – 24 μm. A physical retrieval algorithm was developed to

retrieve microphysical cloud properties in single and mixed-phase Arctic clouds, and the details of this algorithm are presented in Chapter 7. Chapter 8 discusses the sensitivity and accuracy of the physical retrieval using both simulated data and case studies. Statistics of Arctic clouds from a 7-month experiment in the Arctic are presented and discussed in Chapter 9. The thesis concludes with a short summary of this work, the impact of it, and the future outlook using this approach.

Chapter 2

2. Background and Motivation

Clouds play an important role in Earth's radiative energy budget due to their absorption and scattering of solar and infrared radiation. One of the largest sources of error in the global climate models (GCMs) is due to the uncertainty in the cloud-radiative feedback mechanisms (e.g., Wetherald and Manabe 1988, Mitchell and Ingram 1992). GCMs are used to evaluate the sensitivity of the climate to various perturbations, such as the doubling of carbon dioxide. Uncertainties in the cloud-radiative interactions lead to very large differences in the simulated climate by different GCMs (e.g., Cess et al. 1990), making it difficult to draw firm conclusions regarding the sensitivity of the climate to the prescribed perturbation. Furthermore, it is hypothesized that cloud properties change as the climate changes (Lindzen 1990), and therefore a good understanding of the coupling between cloud radiative and physical properties is needed to accurately represent climate change.

Nonetheless, GCMs are being used to assess our understanding of the global climate system. An Intergovernmental Panel on Climate Change (IPCC) report has highlighted that the Arctic is very sensitive to doubling the carbon dioxide concentration (IPCC 1992). Although there is large uncertainty between the different GCMs used in this study, the models demonstrate that the Arctic will experience two to three times more warming than the mean global warming (IPCC 1992). However, Tao et al. (1996) have found that there are large 1-3 C biases (which change sign depending on the season) in the Arctic surface temperatures simulated by 19 GCMs compared to observations. The inability to simulate the current climate conditions of the Arctic casts doubt on the overall utility of GCMs in simulating

climate change. Tao et al. (1996) suggest that the highest priorities for improving the GCMs are the proper treatment of cloud-radiative interactions and the local surface-atmosphere interactions.

Due to its high latitude, the Arctic receives very little solar energy input, resulting in more energy being radiated to space than is input from the sun when averaged over the annual cycle. This energy difference is made up by energy transport from lower latitudes via the atmosphere and ocean. This results in the Arctic serving as a heat sink for the global climate system (Nakamura and Oort 1988). Figure 2.1 indicates schematically the energy balance of the Arctic. The import of heat energy is accompanied by large influxes of water vapor and aerosols from mid-latitudes, which modify the cloud radiative and physical properties. Large emissions of latent heat from open leads, polynyas, and other sources of open water can also effect the clouds above (Curry et al. 2000).

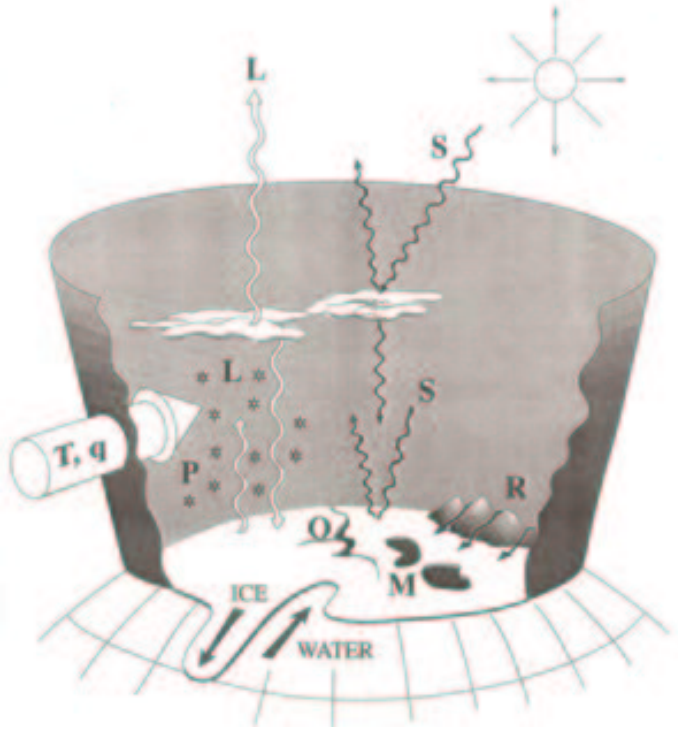

Figure 2.1: Energy budget of the Arctic. To first order, longwave cooling to space balances the advection of heat into the Arctic. S: Shortwave, L: Longwave, T: Temperature advection, q: moisture advection, O: sensible and latent heat from the ocean, M: melting show and ice, R: freshwater run-off. From the NSIDC Arctic Climatology and Meteorology Primer.

Clouds are inextricably linked to the surface

properties, and in particular to the snow/ice albedo feedback process (Curry et al. 1996). For example, melting may lead to an increase in the water vapor and hence to increased cloud formation, which may change the snow/ice albedo feedback because clouds also have a high albedo. Increased cloudiness can lead to warming of the surface, due to the emission of infrared radiation by the clouds. Thus, the net warming or cooling effect of the cloud depends on the exact microphysical (phase, size of the particles, etc.) and macrophysical (height, vertical extent, cloud fraction, etc.) properties of the cloud. To gain insight on how clouds interact with the radiative fields, as well as how they are linked with surface and other atmospheric processes, observations of both the macrophysical and microphysical properties of clouds in the Arctic are required.

Humankind has garnered incredible amounts of cloud data from satellite remote sensing instruments. Retrieval methods have provided estimates of cloud properties that have increased our understanding of the role clouds play in the earth's climate. However, retrievals of Arctic cloud properties from satellite remote sensors are greatly hampered by the highly reflective surface and the presence of a persistent temperature inversion. Furthermore, most Arctic clouds are optically thin and reside close to the surface, resulting in small temperature contrast. These difficulties result in the polar regions having the largest errors in International Satellite Cloud Climatology (ISCCP) cloud property and in the Earth-Radiation Budget Experiment (ERBE) cloud-radiation forcing data sets (Rossow and Garder 1993, Ramanathan et al. 1989). To improve satellite-based cloud property retrievals, extended cloud observations that span all seasons are required for validation.

In situ observations of cloud microphysical properties in the Arctic are sparse. There have been a few experiments wherein aircraft with various in situ probes have sampled Arctic

clouds in the spring or summer seasons (e.g., Koptev and Voskresenskii 1962, Jayaweera and Ohtake 1973, Herman and Curry 1984, Curry et al. 2000). There has only been one documented experiment that collected in situ observations of cloud properties during the autumn (Curry et al. 1997) and no published measurements of liquid water path and/or droplet size during the winter (Garrett et al. 2002). Moreover, accurate in situ measurements of mixed-phase cloud properties is challenging due to the way different instruments respond to ice and water, as well as the fact that supercooled liquid water often freezes to the probes (Curry et al. 1997). As a result, the seasonal variation of cloud properties from in situ observations in the Arctic is unknown.

The lack of cloud observations in the Arctic results in many unanswered questions, an overview of which is provided by Curry et al. (1996). One of the primary unknowns is the thermodynamic phase of Arctic clouds. The degree to which the radiation is modulated depends on the thermodynamic phase, size, shape, and density of the cloud particles, as these dictate the single scattering properties of the particles. The determination of the phase of the cloud particles (i.e., whether they are liquid water or ice) is a prerequisite to specifying the optical properties, as an incorrect phase assessment can lead to errors in the estimates of the single scattering properties. These errors lead to errors in the modeled radiative flux. For example, an incorrect determination of cloud phase can result in large (20%-100%) errors in the effective radius of the cloud particles and optical depth, which translate into errors in the downwelling longwave and shortwave fluxes of 5%-20% (Key and Intrieri 2000). The large errors in the longwave radiative flux at the surface can have important climatic affects by altering the freezing and melting rate of the ice in the Arctic, especially in the spring and autumn transition seasons (Jiang et al. 2000).

Simulations of climate are very sensitive to the specification of mixed-phase clouds within GCMs (Gregory and Morris 1996). In situ observations in the Arctic have shown examples where a predominately liquid water cloud existed at a temperature as low as –32 C and a completely glaciated cloud at a temperature as high as –14 C (Curry et al. 1996). There have been cases where ice crystals were present when the cloud was as warm as –4 C (Curry et al. 2000). Observations and simulations have shown that a mixed-phase cloud can persist for days at a time, even though the presence of ice and liquid water at temperatures below freezing is inherently unstable (Rauber and Tokay 1991, Pinto 1998, Girard and Blanchet 2001). This phenomenon is unique to the Arctic, and is linked to the relative scarcity of ice nuclei, strong radiative cooling of the clouds, and vertical structure of the influx of water vapor (Jiang et al. 2000, Pinto et al. 2001).

There is a strong seasonal fluctuation of aerosols into the Arctic from the mid-latitudes, with January-April typically having higher anthropogenic aerosols than other periods (Barrie and Hoff 1986, Sirois and Barrie 1999). Arctic clouds demonstrate a high sensitivity to changes in the anthropogenic aerosols (Garrett et al. 2002). Given the role that aerosols play in both single and mixed-phase clouds (Twomey 1977) and the strong seasonal fluctuation of these aerosols, it is hypothesized that the springtime mixed-phase clouds have a different microphysical composition than mixed-phase clouds in the autumn (Curry et al. 1996, Curry et al. 2000). To evaluate this hypothesis, as well as to evaluate and improve the cloud-radiative feedback mechanisms, long-term (i.e., multi-seasonal) data sets on cloud phase and other cloud microphysical properties must be compiled.

Two programs were developed in the 1990's to begin to address the incredible shortage of cloud data in the Arctic. The Surface Heat Budget of the Arctic (SHEBA)

experiment was a large, multi-agency, interdisciplinary experiment. During SHEBA, the Canadian icebreaker *Des Grosilliers* was frozen into the perennial icepack from October 1997 through September 1998, serving as a floating scientific research station to enhance the understanding of the thermodynamic coupling between the atmosphere, the sea ice, and the ocean (Uttal et al. 2002). The Department of Energy's Atmospheric Radiation Measurement (ARM) program also established a long-term (> 10 year) site at Barrow, Alaska in October 1997. This site is referred to as the North Slope of Alaska (NSA) Cloud and Radiation Testbed (CART) site. The programmatic objectives of ARM are to (1) relate the observed radiative fluxes (both spectrally resolved and as a function of position and time) to the temperature and composition of the atmosphere over a wide range of conditions, and (2) develop and test parameterizations that can be used to accurately predict the radiative properties and radiative interactions with water vapor and clouds in GCMs (Stokes and Schwartz 1994). Some specific objectives for the NSA site include (1) improved treatments of the radiative effects of mixed-phase and ice-phase clouds, aerosols, and cloud-aerosol mixtures, and (2) improved description of basic cloud microphysical properties and how they are influenced by atmospheric thermodynamics and aerosol characteristics (Stamnes et al. 1999). Figure 2.2 indicates the location of the ARM site and the path the *Des Grosilliers* traced during SHEBA. The ARM program contributed much of the passive ground-based remote sensing instrumentation used during SHEBA, and both experiments were equipped with similar active remote sensors. A full list of all of the instruments deployed as part of the NSA site is given by Stamnes et al. (1999) and a list of the instrumentation deployed at SHEBA is given by Uttal et al. (2002) and Curry et al. (2000).

Cloud phase can be determined from active remote sensors that are polarization sensitive (e.g., Sassen 1991, Sekelsky and McIntosh 1996). [CO_2 lidars can also be used to determine cloud phase, but a differential absorption approach is used (Eberhard 1995).] From polarization sensitive remote sensors, the cloud phase is determined by analyzing the change in the polarization of the backscattered energy, with respect to the polarization of the transmitted energy, that is induced by the shape of the scattering cloud particles. Spherical particles, such as suspended liquid water droplets, induce very little change in the polarization of the backscattered electromagnetic wave, typically on the order of 3%-7%, while ice crystals, due to their more complicated shapes, can induce significant 10%-50% changes in the polarization. One of the shortcomings of the instrumentation at the NSA site is the lack of an active polarization-sensitive instrument. The lidar deployed at the NSA site is a single-polarization elastic lidar (Campbell et al. 2002) and thus the phase of the scattering particles can not be inferred from this data. However, the lidar deployed during SHEBA was polarization-sensitive (Alvarez et al. 1998). Therefore, it is my

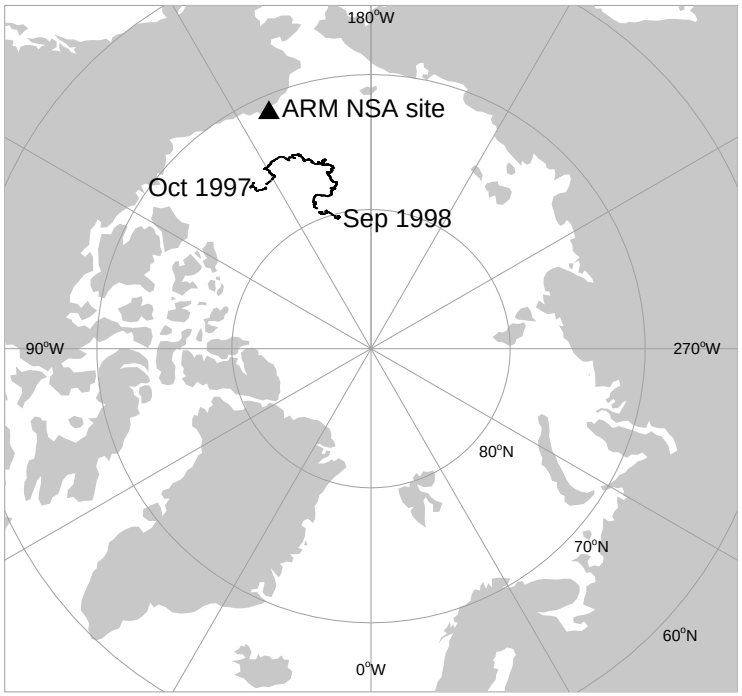

Figure 2.2: Location of the ARM North Slope of Alaska (NSA) site and the path traced by the Des Grosilliers *during SHEBA.*

goal to develop an algorithm to determine cloud phase from the passive remote sensors at SHEBA, using the collocated polarization-sensitive lidar for validation, with the long-term goal of being able to use the same algorithm to analyze the multi-year NSA data record.

Several methods exist for determining the phase of clouds from remote sensing measurements. The simplest method is to specify phase based upon the cloud boundary temperature directly calculated from infrared radiance observations (Rossow and Schiffer 1999). Other investigators have taken advantage of the differences in the refractive indices of ice and water as a function of wavelength. For example, Strabala et al. (1994) used observations at 8.5, 11, and 12 μm to ascertain cloud phase, where the absorption coefficient of ice is larger than that of water at 11 and 12 μm, but is nearly identical at 8.5 μm. Key and Intrieri (2000) modified the tri-spectral infrared method of Strabala et al. (1994) by using observations at 3.7 μm in addition to the observations at 11 and 12 μm from the AVHRR to determine cloud phase since the AVHRR does not have an 8 μm channel. Baum et al. (2000) extended the tri-spectral method by using MODIS Airborne Simulator (MAS) observations at 0.65, 1.63, and 1.90 μm, in addition to observations at 8.5, 11, and 12 μm, to ascertain cloud phase. Knap et al. (2002) have built upon the work of Pilewski and Twomey (1987a,b) to use reflectivity observations at 1.64 and 1.70 μm to determine cloud phase. All of the methods above utilized spectral regions where the absorption coefficient of ice was either larger than or the same as that of liquid water. However, Daniel et al. (2002) recently developed a technique to retrieve cloud phase from spectrally resolved observations from 850-1050 nm, where the ice absorption is larger than that of liquid water for a portion of the band, and less than that of liquid water in another portion of the band. This technique, along with most of the other methods (Key and Intrieri 2000, Baum et al. 2000, and Knap et al. 2002), utilize

channels that have a significant shortwave component, and are dependent on viewing and solar zenith angles. Since these techniques are restricted to daytime only, they cannot measure the seasonal cycle of cloud properties since they are not applicable during the polar winter.

The methods above were also developed for narrowband observations; i.e., measurements that have a spectral resolution of tens of wavenumbers or more. Because of the spectral width of these narrowband observations, the observations include contributions from line absorption (typically from water vapor), continuum absorption (which is the sum of the contribution of the absorption in the far wings of the lines), and cloud and aerosol absorption. However, high-spectral-resolution observations have the spectral resolution necessary to look between the absorption lines in "microwindows", which reduces the uncertainty in the cloud analysis from uncertainty in the strength and width of the individual absorption lines.

High-spectral-resolution infrared observations have been used for cloud studies for over a decade. Cloud heights can be accurately determined with the CO_2-slicing method applied to high-spectral-resolution radiance observations on the 15 μm absorption band of carbon dioxide (Smith and Frey 1990, Smith et al. 1999). Cirrus cloud properties have been retrieved using high-spectral-resolution nadir observations from 3-15 μm from aircraft in many experiments (e.g., Ackerman et al. 1990, Smith et al. 1993b, Ackerman et al. 1993, Ackerman et al. 1995, Smith et al. 1998). In addition, zenith observations of the 3-15 μm band from ground-based infrared interferometers have also been used to retrieve cloud properties (e.g., Smith et al. 1993b, Collard et al. 1995, DeSlover et al. 1999, Mahesh et al. 2001).

Many different passive remote sensors were deployed as part of the SHEBA and ARM experiments, including instruments that are sensitive to solar, infrared, and microwave radiation. Solar instruments, such as pyranometers and multi-filter shadowband radiometers, are limited to periods of daylight; therefore, these instruments are useless for many months during the winter and unable to provide yearly statistics of cloud properties. Infrared and microwave observations are made during both the daytime and nighttime periods. However, the microwave radiometers deployed during both the SHEBA and NSA experiments do not have channels at frequencies sensitive to ice. The Atmospheric Emitted Radiance Interferometer (AERI), which makes high-spectral-resolution infrared radiance observations, provides a unique set of measurements that is sensitive to water vapor, cloud ice, and cloud liquid water.

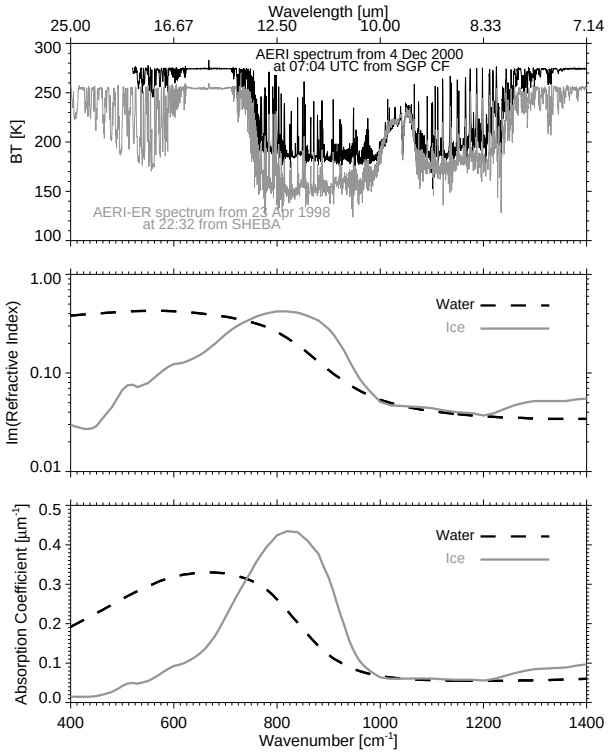

Figure 2.3: Example clear sky brightness temperature spectrum observed by the AERI in the Southern Great Plains (SGP) and during SHEBA (top). The imaginary refractive indices of water and ice (middle) and the associated absorption coefficients (bottom).

To determine cloud phase unambiguously with passive remote sensing instruments, the observations must encompass wavelengths where the absorption by ice and water 'flips' with respect to each other. For example, Figure 2.3 demonstrates that in the infrared between 8 and 25 μm the

absorption of ice is sometimes greater than water and at other wavelengths is less than water. By extending the AERI observations from the typical longwave limit of 16 μm, which was imposed primarily by detector technology, to 25 μm, the AERI instrument is able to make observations in spectral regions where ice is both more and less absorbing than water. Therefore, the AERI data offers the promise of unambiguous phase determination. Daniel et al. (2002) also retrieved cloud phase by using a spectral region where the absorption coefficient of ice and water flips (850-1050 nm), although as indicated earlier their results are restricted to daytime periods.

This study has three primary objectives. These objectives are to:

1. Determine if cloud phase can be determined unambiguously from high-spectral-resolution ground-based infrared radiance measurements (i.e., from AERI observations),

2. Develop a retrieval algorithm that utilizes these observations to retrieve cloud microphysical properties such as cloud optical depth, ice fraction, water content, and effective sizes of the ice and water particles,

3. Compile statistics on cloud properties derived from the SHEBA observations, both for the entire experiment and monthly, which can be used develop a basic description of Arctic cloud microphysical properties and begin to investigate some of the other uncertainties associated with Arctic clouds.

Naturally, these objectives must be tackled in sequential order, as the earlier objectives are required to accomplish the later ones.

Chapter 3

3. Instruments

3.1. Atmospheric Emitted Radiance Interferometer (AERI)

The AERI instrument (Figure 3.1) is a fully automated, ground-based, passive interferometer that measures downwelling infrared radiance with better than 1 wavenumber (cm^{-1}) resolution from 550- 3100 cm^{-1} (19 to 3.2 μm). The AERI was developed for the ARM program by the University of Wisconsin - Madison as a ground-based version of the high-spectral-resolution infrared sounder (HIS; Smith et al. 1993a, Revercomb et al. 1993). The instrument is based around a commercially available interferometer (Michelson series MR100 from Bomem, Inc. of Quebec, Canada). The maximum optical path delay is approximately ±1 cm, resulting in a maximum unapodized spectral resolution of 0.5 cm^{-1}. The output from the interferometer is directed to a pair of detectors. The HgCdTe detector, which is sensitive to longwave radiation from 5 - 19 μm, is placed behind the InSb detector, which is sensitive to radiation from 3.3 to 5 μm and is transparent to longer wavelength radiation. The detector "sandwich" is cryogenically cooled with a solid state Stirling

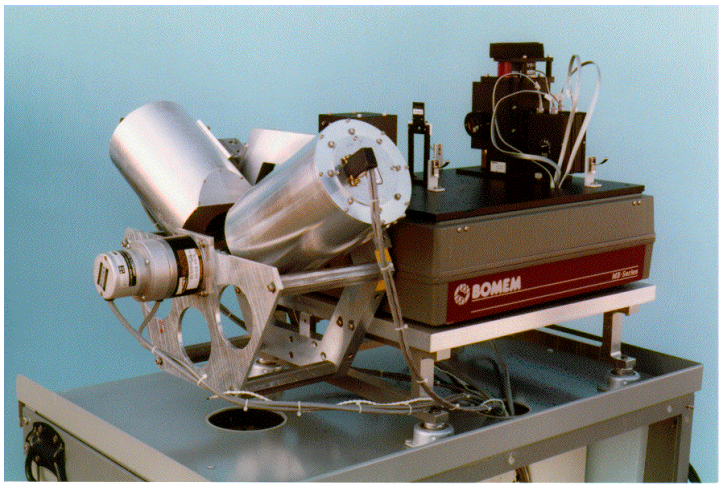

Figure 3.1: The Atmospheric Emitted Radiance Interferometer (AERI).

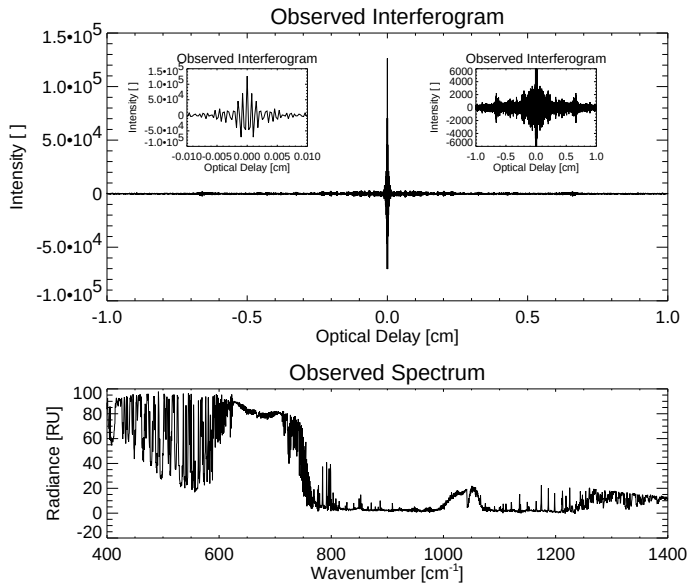

Figure 3.2: An observed interferogram (upper) and the corresponding spectrum from the AERI-ER at SHEBA. The inset images show 'zooms' of the interferogram in the x (left) and y (right) dimensions to demonstrate the detail and information in the data. A radiance unit (RU) is 1 mW / (m^2 ster cm^{-1}).

cooler, eliminating the need for liquid nitrogen. It takes approximately 1 second to collect a single interferogram, but the interferograms are usually co-added for several minutes to improve the signal-to-noise ratio. The standard integration time is 3.5 min for the sky dwell, and 2 min for each blackbody view, resulting in a sky spectrum approximately every 8 minutes. These averaging times were selected early in the ARM program to optimize the observed data for clear sky applications. A typical interferogram collected by an AERI instrument, along with the resulting radiance spectrum computed from the Fourier transform of the interferogram, is shown in Figure 3.2.

The cloud conditions over the instrument can change significantly in the 3.5 min period that the AERI is observing the sky. However, the instrument software automatically computes a "sky variability" spectrum as the difference in the standard deviation of the sky radiance minus the standard deviation of the hot blackbody radiance, which allows these periods of rapid changes in sky conditions to be identified. A sky variability spectrum is stored for each observed spectrum. Examples of typical sky variability spectra for a clear sky

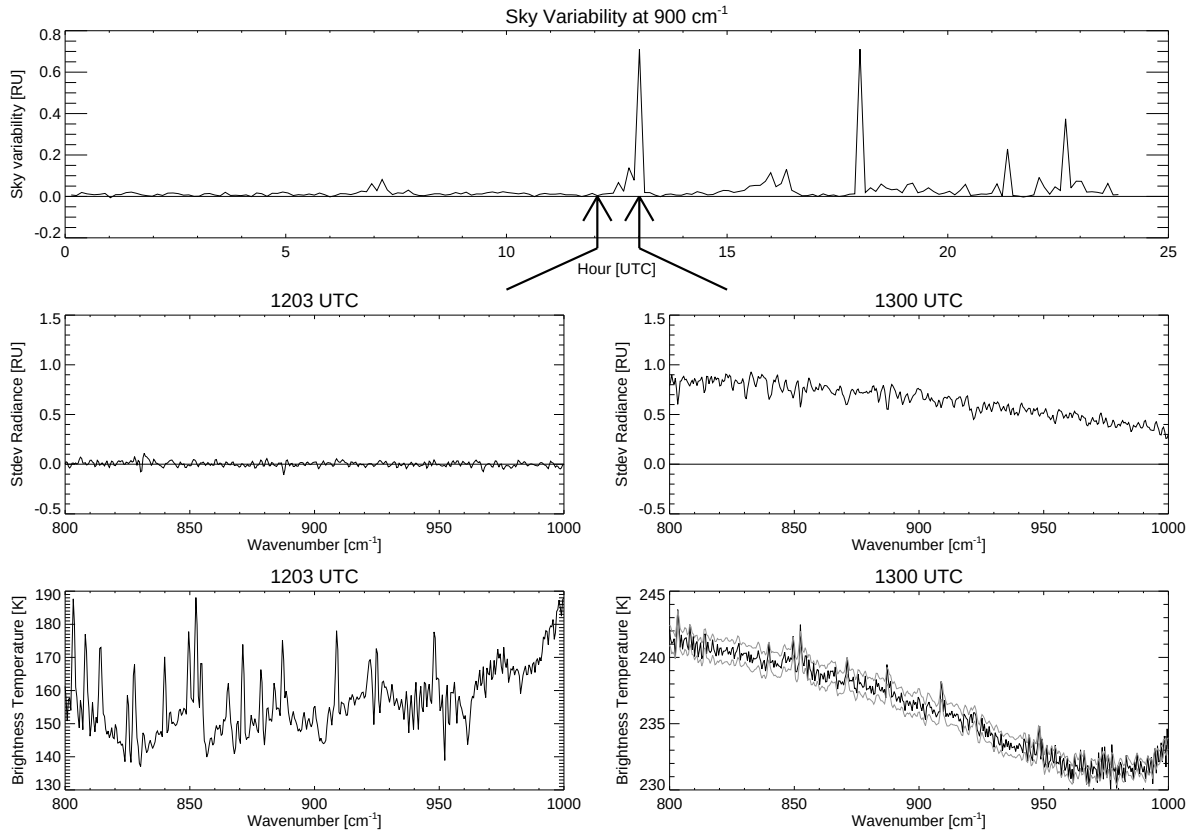

Figure 3.3: A time-series of the sky variability at 900 cm^{-1}, together with radiance sky variability spectra for two selected time periods. The sample at 1203 UTC is a clear-sky period, while the sample at 1300 UTC shows significant variability during the sky dwell. The bottom panels demonstrate the size of the uncertainty in the observed brightness temperature spectra for these periods for given radiance variability spectra.

dwell period and a sky dwell period where the cloud conditions are rapidly changing are given in Figure 3.3.

The interferometer has a finite optical delay (approximately 1 cm), and thus the interferogram is truncated at this point. This introduces an instrument line shape into the radiance spectrum. The line shape is well approximated by the sinc function $\sin(x)/x$, where x is the optical path delay. Before comparing monochromatic radiance calculations to the AERI observations, the calculations must be convolved with the sinc function (Figure 3.4) to properly reduce the spectral resolution of the calculation.

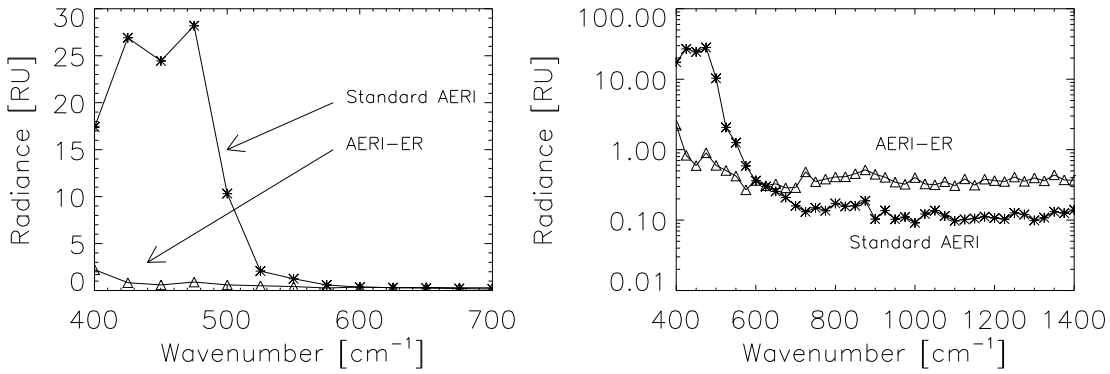

Figure 3.5: Typical random noise spectra for the normal AERI and the AERI-ER on a linear (left) and log (right) plot.

In very cold and dry atmospheres, such as in the Arctic, the spectral region from 17-25 μm, which is in the rotational water vapor absorption band, becomes transparent. The peak of the Planck function also shifts to longer wavelengths at cold temperatures, making measurements in this spectral region critical for energy balance studies in these cold and dry conditions. Observations are required to address the serious need for model validation in this spectral band (Sinda and Harries 1997), since there have been few observations of the atmospheric emitted radiance in this spectral band. Therefore, AERIs deployed to the Arctic have been modified to extend their spectral range from 550 cm^{-1} (19 μm) to 400 cm^{-1} (25 μm). This instrument modification results in slightly higher noise performance in the 8-13 μm window for the extended range (ER) systems as compared to a standard AERI instrument (Figure 3.5).

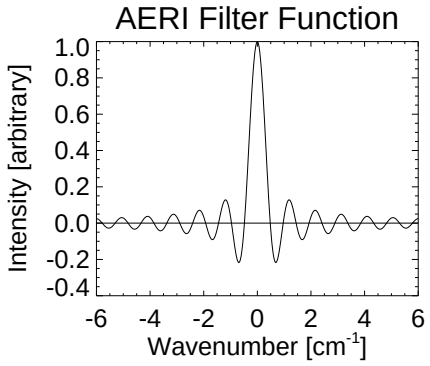

Figure 3.4: The AERI instrument function.

The calibration goal for the AERI is to

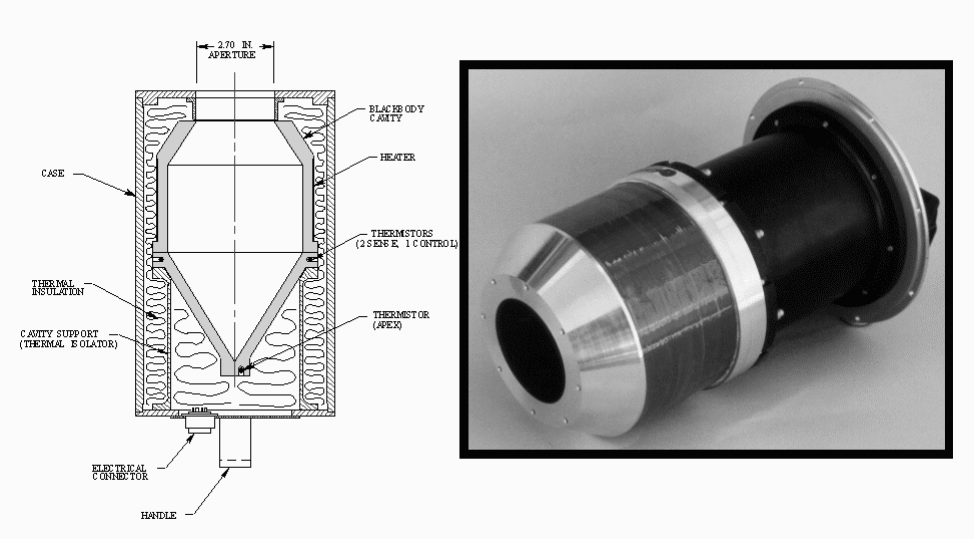

Figure 3.6: A schematic drawing and picture of the high-emissivity AERI blackbody calibration targets. Each AERI has two: one operating at ambient temperature and the other actively maintained at 60 Celsius.

observe downwelling atmospheric radiance with an accuracy of better than 1% of the ambient radiance (Revercomb et al. 1993). Two well-characterized blackbody targets (Figure 3.6) are used to achieve this accuracy, and a rotating gold-plated scene mirror is used to direct radiation from the target (either the sky or one of the blackbodies) into the interferometer. A typical measurement cycle consists of a 3.5-minute sky dwell period, followed by a 2-minute dwell period for each of the blackbody targets. The blackbodies are high-emissivity (greater than 0.995) targets that contain accurate NIST traceable temperature sensors (Best et al. 1997, Minnett et al. 2001). The temperature of one of the blackbodies is fixed at 60 C, while the other is allowed to float at the ambient temperature. One of the advantages of using an ambient calibration target is that much of the emission measured by the AERI is from the atmosphere very close to the instrument. Therefore, the calibration error is very small for temperatures very near the surface temperature.

The instrument measures interferograms, from which complex radiance spectra are computed using Fourier transforms. The interferograms, collected from both the sky and the blackbodies, are corrected to account for detector non-linearity, which is primarily due to detector saturation at zero path difference (ZPD). The complex spectra observed from the blackbodies at known temperatures are used to calibrate the atmospheric spectrum following Revercomb et al. (1988). The calibrated sky radiance is given by

$$N_\nu = \mathrm{Re}\left(\frac{C_\nu - C_{\nu,C}}{C_{\nu,H} - C_{\nu,C}} \right) \left(\hat{B}_\nu \left(T_H \right) - \hat{B}_\nu \left(T_C \right) \right) + \hat{B}_\nu \left(T_C \right) \tag{3.1}$$

where N_ν is the calibrated sky radiance, and C_ν, $C_{\nu,H}$, and $C_{\nu,C}$ are the detected counts for the sky and hot and cold blackbodies, respectively. The terms $\hat{B}_\nu(T)$ are the radiance terms computed from the observed temperatures of the hot (T_H) and cold (T_C) blackbodies. As the blackbody (BB) targets have an emissivity $\varepsilon_{\nu,BB}$ that is less than unity, these radiance terms are modified to account for the small amount of reflected energy that gets into the cavity as

$$\hat{B}_\nu(T_{BB}) = \varepsilon_{\nu,BB} * B_\nu(T_{BB}) + (1 - \varepsilon_{\nu,BB}) * B_\nu(T_{reflected}) . \tag{3.2}$$

Figure 3.7 provides an example of how well two AERI instruments agree with each other, demonstrating that the calibration is reproducible. More details on the AERI instrument and its calibration procedures are provided by Knuteson et al. (2003).

The calibration equation (3.1) is easily rewritten to investigate how small errors in the observed temperatures or in the blackbody emissivity model propagate into the observed radiance. Typical errors are 0.1 K in the reported temperatures of the blackbodies, 5.0 K error in the temperature of the surrounding support structures (from which the radiance that is reflected from the blackbodies comes), and 0.00026 errors in the emissivity of the blackbodies

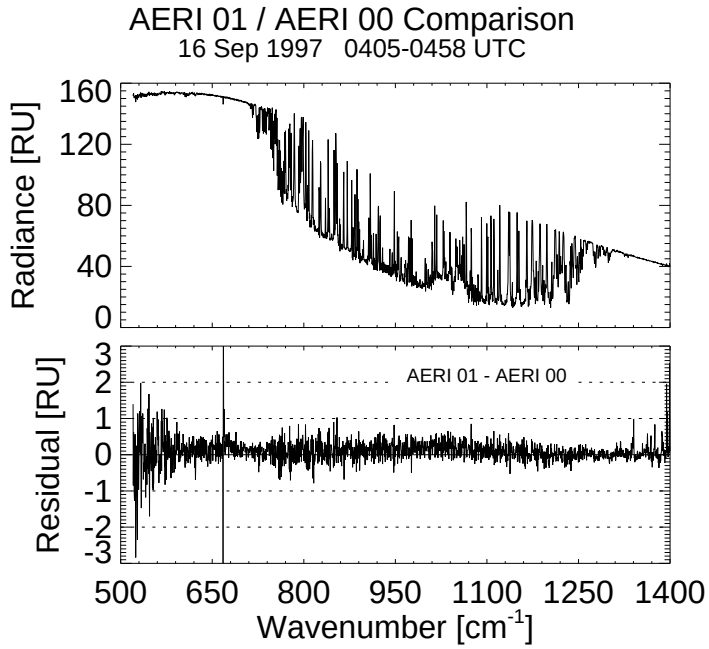

Figure 3.7: Typical comparison of spectra observed by two collocated AERI instruments at the ARM SGP site.

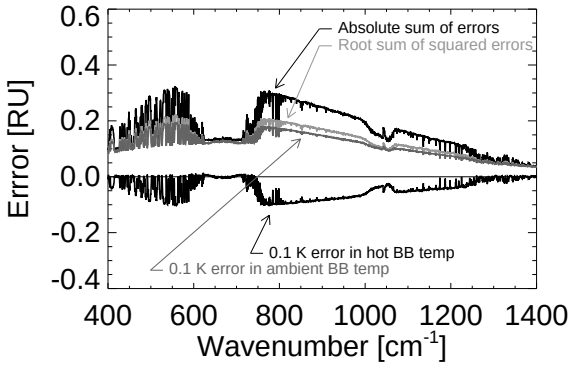

Figure 3.8: Uncertainty in the AERI spectrum given in Figure 3.2 for the typical uncertainties in the temperatures of the hot and ambient blackbodies. Typical uncertainties in the emissivity of these calibration targets result in errors that are negligible. The root sum square error (which is used as the typical uncertainty in the radiance spectrum) and the absolute sum of errors (worst case) are also shown.

themselves. The error spectra, including an absolute sum of errors and a root mean square error spectrum, are given in Figure 3.8 for the observed spectrum shown in the bottom of Figure 3.2. Note that the error spectra associated with the assumed errors in the reflected temperature and the emissivity errors have magnitudes less than 0.02 RU and thus are not shown. The importance of these uncertainties in the AERI observations to this study is discussed in Chapter 4.

3.2. Microwave radiometer (MWR)

The microwave radiometers (MWRs) used at the ARM facilities and at SHEBA are Radiometrics WVR-1100 radiometers (Figure 3.9). These instruments are 2-channel systems that measure downwelling radiation at 23.8 and 31.4 GHz every 20 s. Water vapor and liquid water burdens along a selected path (nominally zenith at the ARM sites) can be retrieved simultaneously from measurements at these two frequencies. Atmospheric water vapor observations are made near the "hinge point" of the 22.2 GHz water vapor line where the vapor emission does not change with pressure and hence is altitude independent. [The actual hinge point for the 22.2 GHz water vapor line is approximately 24.4 GHz (S.A. Clough, personal communication, 2001).] Water vapor emission dominates the 23.8 GHz observation, whereas cloud liquid water, which emits in a broad continuum that increases with frequency, dominates the 31.4 GHz signal (Figure 3.10). By observing these two frequencies, the precipitable water vapor (PWV) and liquid water signals can be separated using either physical or statistical retrieval techniques.

Figure 3.9: Radiometrics WVR-1100 microwave radiometer (MWR).

Operationally, the ARM program uses the "Liebe87" microwave absorption model (Liebe and Layton 1987) in a quasi-statistical approach to retrieve PWV and cloud liquid water for each 20-s observation. The retrieval method, which is summarized here, is provided in Liljegren and Lesht (1996). A historical database of radiosondes from the SGP region are used to drive the Liebe87 model to compute opacity and mean radiating temperatures in each of the two channels. Averages of the mean radiating temperature have been created for each month of the year, and these average values are used to derive linear relationships between the opacity in each channel with the PWV and cloud liquid water. These linear relationships are then used to retrieve PWV and cloud liquid water from the observed sky brightness temperatures, which are easily converted to opacity with the use of the appropriate monthly-averaged mean radiating temperatures.

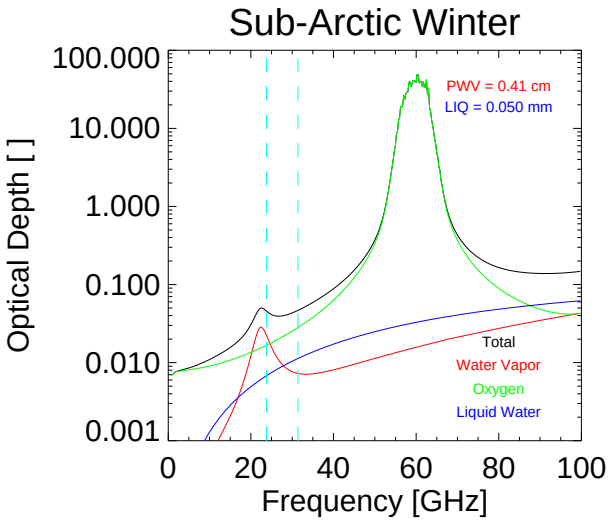

Figure 3.10: Optical depth spectra in the microwave for the subarctic winter atmosphere with a typical Arctic liquid water cloud overhead. The two frequencies of the ARM MWRs are indicated by the dashed vertical lines.

Calibration is crucial to the accurate retrieval of PWV and cloud liquid water from the MWR. The ARM instruments have a single ambient blackbody target that is viewed as part of every sky view sequence. The blackbody is viewed both normally and when a noise-diode, which inserts a fixed amount of additional energy into the system, is turned on. These two values allow the gain of the instrument to be determined, provided that the "temperature" of the noise diode is known. To determine this temperature, the ARM radiometers use the tip-

curve method (Han et al. 1994), whereby the instrument takes observations at a series of angles on either side of zenith in a vertical plane. If the sky is horizontally homogeneous, then the opacity, which varies linearly with airmass (cosine of the zenith angle), can be used to determine the gain of the system. This process allows the temperature of the noise diode to be determined from the raw voltage measurements made by the system. An automated routine was developed which collects tip-curve data whenever the sky is deemed to be clear and homogeneous; otherwise the system is placed in a zenith-only mode. This routine processes these tip-curves, allowing the calibration of the instrument to be continuously maintained (Liljegren 2000). This automated routine is able to maintain the calibration to 0.2 - 0.3 K RMS, which corresponds to an uncertainty in PWV of less than 0.3 mm. This auto-calibration algorithm was installed on the ARM MWRs in October 1998, but the SHEBA instrument collected tip-cal curves continually during its deployment so that its data could be post processed to ensure a consistent, high-quality, calibrated data set.

The strong temperature dependence of the dielectric constant of liquid water at microwave frequencies has been known for decades (Grant et al. 1957). The uncertainty in the dielectric constant directly impacts the uncertainty in the mass absorption coefficient of liquid water. Liquid water has been shown to exist at temperatures as low as –32 C (Witte 1968), which is much colder than the data collected in the laboratory to develop models of liquid water absorption in this spectral region (Westwater et al. 2001). The standard ARM retrieval of cloud liquid water utilizes the liquid water absorption model from Grant et al. (1957), which was developed from laboratory observations of liquid water above 0 C. Westwater et al. (2001) have shown that utilizing either the Rosenberg (1972) or the Liebe et al. (1991) models, which utilized data at -8 C and –4 C in their development, reduced the

original ARM retrievals by 20%-30%, which resulted in better agreement with in situ observations. However, large uncertainties remain in the liquid water absorption in the microwave region, which could be reduced by combining it with retrievals of liquid water in the infrared.

3.3. Radiosondes

The ARM program utilizes the Vaisala RS80-H radiosonde for all of its soundings, including those measurements made during SHEBA. These radiosondes incorporate the H-humicap capacitive moisture sensor that is more sensitive and stable than the more commonly used A-humicap (Antikainen and Paukkunen 1994). All soundings are done with a 350 g balloons and have a mean ascent rate of 5 m s^{-1}. The sensors measure temperature, relative humidity, pressure, and wind speed and direction, and the raw data are output with 1.5 s resolution. This high-resolution data is processed with the standard software provided by the manufacturer which quality controls (i.e., filters, edits, and interpolates) the data and outputs it to 2 s resolution. Typically 2-4 radiosondes were launched daily during SHEBA and 3-8 radiosondes are launched from the SGP site, but only there is only one launch per day at the NSA site.

Recent work by several groups has shown that a dry bias exists in Vaisala humidity measurements (Guichard et al. 2000, Wang et al. 2002, Turner et al. 2003a). Laboratory analyses have demonstrated that this dry bias is due to chemical contamination of the capacitive moisture sensor, and a correction has been developed to account for this (Wang et al. 2002). The correction also accounts for small errors in the temperature dependence of the

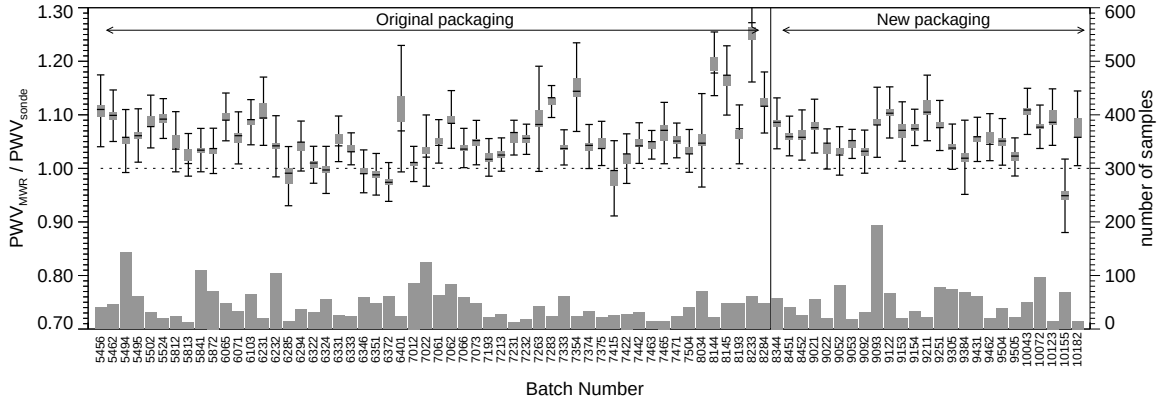

Figure 3.11: Comparison of the ratio of PWV from the MWR to the radiosonde from April 1994 to July 2000 from SGP. Data are included only if the radiosonde achieved a height of 10 km, the liquid water path retrieved from the MWR was less than 50 μm, and the number of samples (given by the histogram on the bottom) was more than 10 for each calibration batch. The error bars indicate 1 std dev about the mean ratio for the calibration batch, while the gray boxes are 1 std error of the mean. Dark horizonal lines indicate the median value for the batch. The transition from the original packaging, which is hypothesized to be responsible for the contamination dry bias, to the new packaging developed to remove the source of the contamination, is included. See Turner et al. 2003a for more details.

sensor and in the basic humidity calibration model, but these components are much smaller than the chemical contamination component for the RS80-H. Analysis of over 2000 radiosondes launched from the ARM SGP site have demonstrated a large sonde-to-sonde variation in the calibration of the water vapor observations (peak-to-peak differences greater than 25%) that is not accounted for by this correction (Figure 3.11, Turner et al. 2003a). Turner et al. (2003a) also demonstrate that Vaisala radiosondes exhibit a significant (~4% in PWV) diurnal bias that is not accounted for by the correction. Additionally, this correction introduces a small, height-dependent bias into the corrected radiosondes (Turner et al. 2003a). For these reasons, ARM does not apply this correction to its radiosonde data operationally.

The dry bias and the sonde-to-sonde variability make these data problematic for input into longwave radiative transfer models, as infrared radiation is very sensitive to perturbations in PWV. Launching two radiosonde sensor packages on the same balloon during special

water vapor IOPs demonstrated that the differences are, to first order, due to a height independent calibration factor error in the radiosonde moisture profiles (Revercomb et al. 2003). Therefore, a height-independent scale factor, which is the ratio of the PWV observed by the MWR and radiosonde, is computed and the radiosonde's mixing ratio profile is multiplied by this scale factor. This has been shown to significantly reduce the sonde-to-sonde variability in the moisture observations, remove the diurnal bias, and account for the dry bias at the SGP site (Turner et al. 2003a). However, Tobin et al. (2000) have shown that scaling the radiosonde profile to the MWR at SHEBA increases the variability in the calibration of the water vapor profile. Fortunately, Miller and Beierle (2000) have compared radiosonde water vapor observations during SHEBA with in situ observations made by aircraft, as well as water vapor observations by other sensors, and have concluded that a dry bias does not appear to exist in the SHEBA radiosonde data. Based on these results, radiosonde data from the SGP region will be scaled to agree with the MWR's observation of PWV, but radiosonde data from SHEBA will not be scaled.

3.4. Depolarization and Backscatter Unattended Lidar (DABUL)

During SHEBA, a polarization sensitive lidar was deployed near the AERI on the *Des Grosilliers*. The NOAA Environmental Technology Laboratory's (ETL) Depolarization and Backscatter Unattended Lidar (DABUL) is a compact, autonomous lidar system, designed to produce research-quality measurements of backscatter and depolarization ratio measurements from clouds and aerosols (Alvarez et al. 1998). The DABUL is a hardened and portable instrument that can be placed in a variety of field locations with minimal infrastructure. The

system transmits pulses of 523 nm light from a doubled Nd:YLF laser. Low pulse energies are used (less than 40 μJ per pulse) and the outgoing laser energy is expanded by the shared transmit/receive telescope (which has a diameter of 30 cm) to assure eye-safety. A high pulse repetition rate (over 1 kHz) and pulse averaging are used to achieve the required signal-to-noise ratio.

The DABUL's receiver only detects light for a single linear polarization, but the polarization of the outgoing light is rotated on alternating pulses by a Pockels cell. This allows both co-polarized and cross-polarized components of the backscatter to be observed. The depolarization ratio (i.e., the ratio of the cross to co-polarized signal as a function of range) provides information on cloud particle phase. The nominal vertical and temporal resolution of the DABUL is 30 m and 5 s, but temporal and vertical resolution can be traded off to improve signal-to-noise in lidar data. The DABUL data used in this study had vertical and temporal resolutions of 30 m and 10 min, respectively.

Depolarization ratio data, such as that collected by the DABUL, provide one way to ascertain the phase of detected cloud particles, up to the limit of signal attenuation. Spherical particles, such as liquid water drops, typically induce little to no depolarization in the forward or backward scattering directions, with values typically less than a few percent, yet have strong total backscatter returns. However, strong multiple scattering by the cloud droplets can induce an increasing depolarization ratio with range, as the scattering by spherical particles at angles other than 0 or 180 degrees does induce some depolarization that can be multiple scattered back into the field-of-view of the lidar. These cases can usually be identified by a very strong backscatter signal. Non-spherical particles, such as ice crystals, typically result in large depolarization ratios (between 10%-50%) depending on such factors as the ice crystal

habit, size distribution, and particle orientation (Sassen 1991). A special case occurs, however, if the ice crystals are coated with water or if water droplets coexist in the same volume as ice crystals (i.e., a mixed-phase cloud), as the depolarization ratio is smaller than that of pristine ice crystals of the same habit. Therefore, there is not a single depolarization threshold that can be used to unambiguously separate ice only clouds from mixed phase clouds.

3.5. Millimeter-wave Cloud Radar (MMCR)

NOAA ETL has also designed and built several millimeter-wave cloud radars for ARM, one of which was deployed during SHEBA. These radars were designed to have high reliability for long-term operations, yet also have excellent sensitivity to detect tenuous clouds overhead. These vertically pointing systems use a single-polarization, 35 GHz Doppler system that uses a low peak power but high duty cycle transmitter (Moran et al. 1998). A large high-gain antenna and pulse compression waveforms are used to increase the sensitivity of the radar. The radar sequences through a set of four modes in roughly 30 s, where each mode has been optimized for detection of different cloud systems, such as high thin cirrus, tenuous boundary layer clouds, thick convective clouds, etc. (Clothiaux et al. 1999). Reflectivity and cloud boundary data from the radar are combined with co-located lidar cloud boundary data to yield the best estimate of the cloud location above the SGP, NSA, and SHEBA sites (Clothiaux et al. 2000). Various retrieval algorithms have been developed to retrieve cloud microphysical properties from the reflectivities and moments observed by the radar (e.g., Frisch et al. 1995, Matrosov 1999, Shupe et al. 2001).

Chapter 4

4. Clear sky radiative transfer

4.1. Forward modeling: A bit of history

Longwave and solar radiative transfer are the prime physical mechanisms that drive the circulation and the temperature structure of the atmosphere, and therefore radiative processes play a central role in most climate change mechanisms (Luther 1984). Recognizing the importance of radiative transfer in climate modeling, the World Climate Research Program, the International Radiation Commission, and the U.S. Department of Energy (DOE) initiated an international radiative transfer model study in the mid 1980's. The Intercomparison of Radiation Codes in Climate Models (ICRCCM) compared results contributed by most of the world's major radiation modeling groups for a variety of specified atmospheres. The initial focus was on clear sky scenes, which are inherently easier to model than cloudy scenes. However, for the clear sky atmospheres, the differences in the longwave radiative fluxes approached 70 W m^{-2} (Ellingson et al. 1991, Ellingson and Wiscombe 1996), which is large compared to the total longwave downwelling flux at the surface (200 - 350 W m^{-2} depending on the atmospheric state). Even the line-by-line models differed by tens of W m^{-2}, but these large differences were due to different formulations of the water vapor continuum absorption. If the different line-by-line models used the same cut-off point for line absorption and the same continua model, the differences were less than 1% in the downwelling flux. Because of the uncertainty in the line absorption parameters, line shape, and continua (Luther et al. 1988), ICRCCM recommended that a dedicated field program be organized to simultaneously measure radiance at high spectral resolution along with the

atmospheric state data (profiles of temperature, water vapor, etc.) needed for the radiance calculations (Ellingson and Fouquart 1991).

This recommendation led to the formation of the DOE ARM program, which was originally scheduled for 10 years. A key component to the ARM program is the establishment of Cloud and Radiation Testbed (CART) sites in several locations worldwide (Stokes and Schwartz 1994). The CART sites are outfitted with a large suite of in situ and remote sensing instrumentation to collect both temporally and spectrally resolved radiance observations and measurements of the atmospheric state (and primarily the clouds and water vapor) which affect the radiance fields.

The long term ARM datasets, along with some focused field experiments funded in part by ARM, led to a series of incremental developments in the Line-By-Line Radiative Transfer Model (LBLRTM[1]; Clough et al. 1992, Clough and Iacono 1995). The LBLRTM is based upon the FASCODE model, and achieves high accuracy with computational efficiency. All of the parameters of the HITRAN database are used, including the coefficient for the self-broadening of water vapor, half-width dependence on temperature, and the pressure shift coefficient. A Voigt line shape is used for all pressures, with a line cutoff at 25 cm^{-1} from line center. A consistently defined water vapor continuum model (CKD; Clough et al. 1989) incorporates both the self-broadened and foreign-broadened components. The LBLRTM includes continua absorption by carbon dioxide, oxygen, and nitrogen. The LBLRTM has been used to generate a rapid radiative transfer model (Mlawer et al. 1997) used in the

[1] The LBLRTM, along with the line parameter database and the continuum model, are available from Atmospheric Research Incorporated's (AER) website (http://rtweb.aer.com).

community climate model CCM3 (Iacono et al. 2000) and other models. Therefore, it is important to validate the LBLRTM with direct observations.

In 1990 (i.e., before ARM), the most current spectroscopic line database was HITRAN 1986 (Rothman et al. 1987) and the current water vapor continuum model was CKD v0, which was derived from first principles (Clough et al. 1989). Utilizing these in the LBLRTM yields the "pre-ARM" observed minus calculated residual in Figure 4.1. The pre-ARM residuals represent an approximate 5.5-7.5 W m^{-2} difference in the longwave flux at the surface. In the early 1990's, the AERI transitioned from a capable instrument when manned

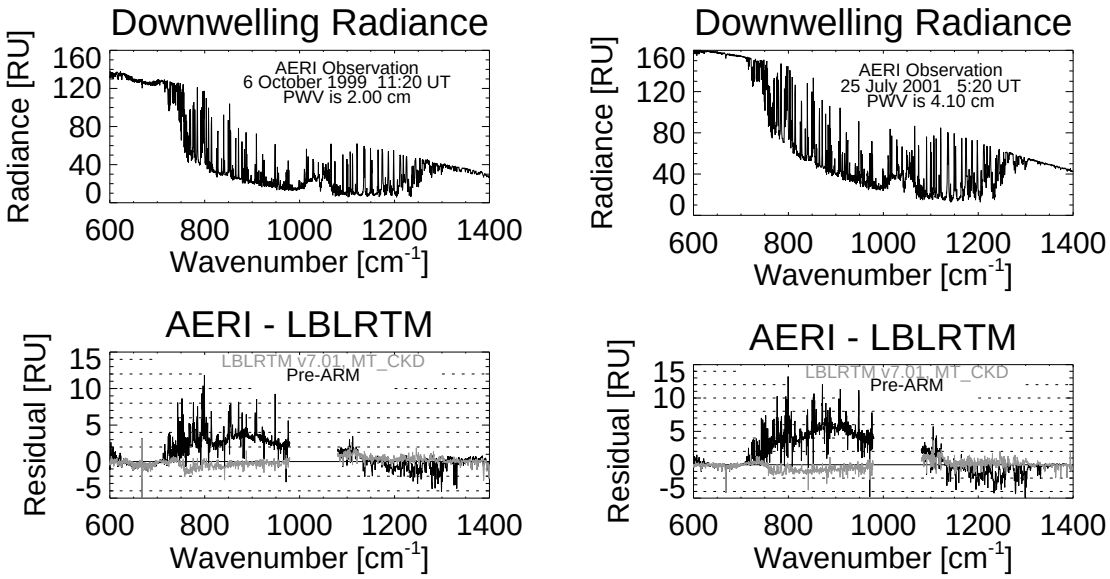

Figure 4.1: Observed AERI spectra for mid (2.0 cm, upper left) and high (4.1 cm, upper right) water vapor burdens, along with the observed minus calculated radiance residuals for two different line-by-line models. The 'pre-ARM' results (in black) demonstrate the state-of-the-art before ARM (i.e., in the early 1990's), using LBLRTM v5.10, HITRAN 1986, and CKD v0. In terms of downwelling longwave flux, the absolute errors associated with these calculations are approximately 5.7 and 7.6 W m^{-2}, respectively. The residuals in gray indicate the current state-of-the-art, using LBLRTM v7.01, HITRAN 2000, and MT-CKD. The absolute value of the residuals using this model translates into errors of 1.5 W m^{-2} in downwelling longwave flux. See Turner et al. 2003b for more details.

to a hardened, automated, field-deployable instrument, and was deployed at the ARM sites and at other locations during several intensive observation periods (IOPs). Data collected during the NOAA/ETL Pilot Radiation Observation Experiment (PROBE) in the moist tropical western Pacific Ocean in 1993 led to a marked improvement in the self-broadened water vapor absorption in the CKD model (Han et al. 1997). The data collected during SHEBA indicated that there were large errors in the foreign-broadened water vapor continuum which became very obvious in the low water regime in the Arctic (Tobin et al. 1999a). These experiments led to the release of the water vapor continuum model CKD 2.4. Using 240 carefully selected cases from the ARM SGP site that spanned a range of PWV, the water vapor continuum model was refined, resulting in the new continuum model MT-CKD 1.0 (Turner et al. 2003b). This continuum model was released in Jan 2003.

During the 1990's, laboratory observations of water vapor absorption lines, and especially weak absorption lines, continued to improve the strength and width parameters of these lines in the HITRAN database, with the latest release being HITRAN 2000. The impact on the model results from the pre-ARM calculation to the current state-of-the-art using HITRAN 2000 and MT-CKD 1.0 are also shown in Figure 4.1. These results demonstrate markedly better agreement in the AERI observations, with spectral residuals that translate into roughly 1.5 $W\,m^{-2}$ in downwelling longwave flux differences at the surface. More importantly, the spectral distribution of the calculated flux is now correct, which results in more accurate calculations of the divergence of net flux in the atmosphere (i.e., cooling rate profiles).

4.2. Comparisons between observations and calculations

A Quality Measurement Experiment (QME; Miller et al. 1994) for the downwelling infrared radiance at the ARM SGP site has been ongoing since 1994. This experiment has three objectives: 1) to validate and improve the absorption models and spectral line parameters used in line-by-line radiative transfer models, 2) to assess the ability to define the atmospheric state, and 3) to assess the quality of the radiance observations that serve as ground-truth for the model. Analysis of data from 1994-1997 suggested improvements in the atmospheric state (Turner et al. 2003a, Revercomb et al. 2003) as well as ways to reduce the uncertainties in the radiance observations. Analysis of the QME data from 1998-2001 (Turner et al. 2003b), where the uncertainties in the observed data were much less than in the 1994-1997 data, were important for the development of the MT-CKD 1.0 water vapor continuum model. However, this data set also demonstrated that a small positive observed minus calculated residual exists, which is especially apparent at low water vapor amounts (PWV less than 1.5 cm). A similar positive bias was also demonstrated in SHEBA data (Tobin et al. 1999a, 2000), although the source for the bias may be different for the two locales. Mean residual spectra for both SHEBA and SGP are given in Figure 4.2. For the low radiance conditions experienced at the surface in the Arctic, this approximately 1 RU difference between the observation and the calculation translates into an approximately 20 K difference in brightness temperature, making accurate retrievals of cloud properties for optically thin clouds problematic. Thus, the source of the bias needs to be determined and understood.

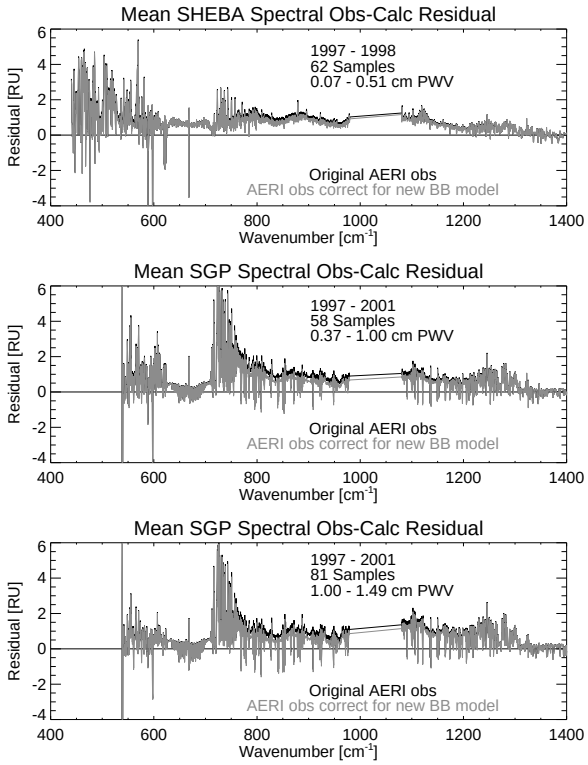

Figure 4.2: Mean observed-calculated downwelling radiance residuals from SHEBA (top) and from SGP for PWV less than 1 cm (middle) and from 1.0-1.5 cm PWV (bottom). The black residuals are for the original AERI observations, while the gray curves denote the residuals after the AERI observations have been corrected for a new blackbody emissivity model. See text for details.

One possible source of the bias could be the water vapor absorption used in the model, where either the PWV used in the calculation was underestimated or the continuum absorption incorrect. Self-broadened water vapor continuum absorption dominates the absorption in the 750-1000 cm^{-1} region and foreign-broadened water vapor absorption dominates the infrared emission from 1200-1400 cm^{-1}. However, even 100% errors in the two continuum components make negligible changes to the absorption computed by the LBLRTM in Arctic conditions because the atmosphere is so dry. By the same token, even 100% errors in the PWV used in the LBLRTM calculation, which are most likely outside the range of calibration errors expected in Vaisala radiosondes (Turner et al. 2003a), only account for perhaps one-third of the observed minus calculated residual at SHEBA (Figure 4.3).

One possible explanation for this 1 RU bias is that there is something unaccounted for in the AERI calibration. The blackbodies are painted with a flat black paint, and witness samples taken of the paint were applied to flat squares of aluminum to determine the paint

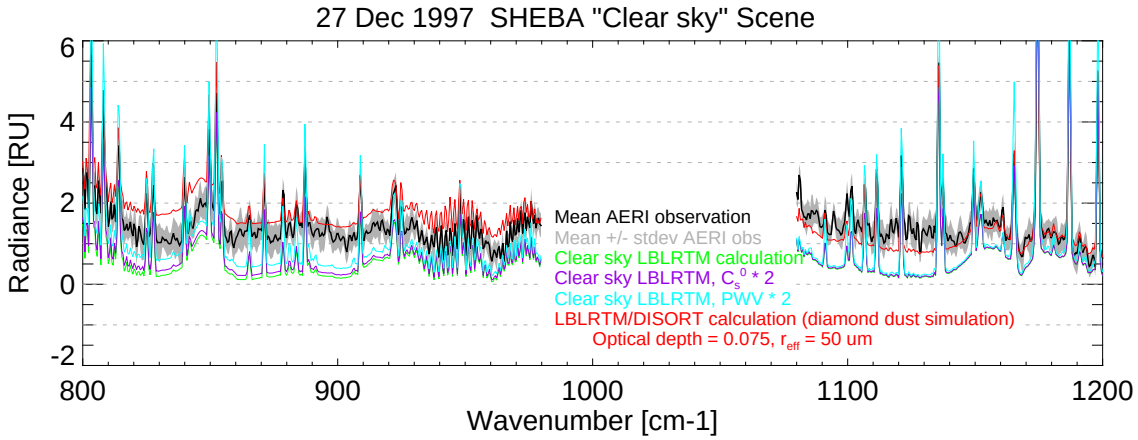

Figure 4.3: Perturbations of the LBLRTM calculations (increasing the PWV, increasing the water vapor continuum absorption, etc.) in an attempt to explain the approximate 1 RU bias in the 8-13 μm window. See text for details.

emissivity. This spectrum is shown in Figure 4.4. Given this paint emissivity p_ν, the cavity emissivity ε_ν is computed by

$$\varepsilon_\nu = \frac{p_\nu}{p_\nu + f(1-p_\nu)} \tag{4.1}$$

where $C_f = 1/f$ is the cavity factor. The cavity factor for the AERI blackbodies was determined to be 12.79 using the Jet Propulsion Laboratory Technical Report No. 32-1463. Recent Monte Carlo tests indicate that using Eq (4.1) to model the cavity effect of the blackbodies is the same as assuming that the instrument has a hemispherical field-of-view (FOV) of the inside of the blackbodies (R.O. Knuteson, personal communication, 2003). The AERI's field-of-view is

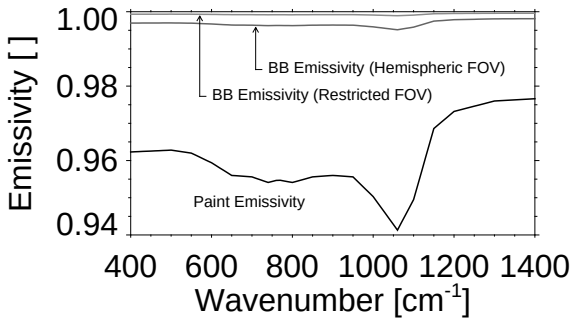

Figure 4.4: Emissivity of the paint measured on a witness sample, and the emissivity of the blackbodies, which are coated with this paint, for two different models.

actually 46 mrad FWHM, and thus the true cavity emissivity for this restricted FOV is much higher.

The clear sky AERI data used in both the SHEBA and SGP QME datasets were recalibrated to account for the new emissivity model for the blackbodies. First, the sky radiance was inverted using Eq (3.1) and the old emissivity model to get the real component of the ratio of the count differences, and then the new the sky radiance was computed using the new emissivity model. Changing the cavity emissivity model reduced the observed minus calculated residuals by 10-15% as shown in Figure 4.2, but a significant bias remains.

Knuteson et al. (1999) discovered (and corrected) a warm bias in the AERI prototype instrument that was initially deployed at the SGP site in 1994. This bias was caused by a slight obscuration of the sky view by the instrument's enclosure. Since the discovery of that obscuration, the AERI instruments were deployed with their foreoptics (scene mirror and calibration blackbodies) in the ambient environment to prevent that phenomenon from occurring again. However, in 1995, it was discovered that dust accumulating on the scene mirror of the AERI at the SGP site (since the mirror was in the ambient outdoor environment) was causing another calibration error. This error was the result of the scattering of the incoming radiation by the dust, effectively widening the instrument's FOV outside the aperture of the calibration blackbodies. To remedy this, an aperture of the same diameter as the entrance to the blackbodies was installed in the sky view port. The idea is that when the scene mirror gets dirty (which is likely since it is in an operational environment) and the FOV increases because of scattering off the scene mirror, the radiance contribution from the aperture of the blackbody will be matched by the contribution by the aperture of the sky port.

This will result in this contribution being canceled due to the differences taken in equation (3.1). It should be noted that the AERI's responsivity R, which is computed as

$$R = \frac{\mathrm{Re}\left(C_{v,H} - C_{v,C}\right)}{\hat{B}_v(T_H) - \hat{B}_v(T_C)}, \tag{4.2}$$

where the elements of the equation are the same as equation (3.1), provides a good measure of the cleanliness of the scene mirror, and is utilized by site operations staff as a indicator of when the mirror should be cleaned.

To verify that this FOV matching aperture does indeed account for the scattering off of a dirty scene mirror, an experiment was conducted on 6 January 2003 using the AERI at the University of Wisconsin – Madison. An Arctic airmass was over southern Wisconsin during this period, with a surface temperature of approximately -18 C and the PWV of 2.2 mm – conditions very similar to those found during SHEBA in the winter. During the experiment, downwelling radiance spectra were collected with the plate that contains the sky view aperture both on and off. This experiment was performed with both clean and dirty scene mirrors.

The results of this experiment are shown in Figure 4.5. When the mirror is clean, there is no difference between the spectra observed when the sky aperture plate is on or off (note that the spectra vary by approximately 0.5 RU at 833 cm^{-1}, but this is atmospheric variability as evidenced by the sample times of the spectra). When the mirror is dirty, there is a significant difference (over 2 RU at 833 cm^{-1}) between the spectra observed with the sky aperture in place versus when it was removed. Negative radiance resulted when the sky aperture was removed, indicating that the sky aperture is required. Furthermore, the radiance observed with the aperture installed and the dirty scene mirror is within 0.5 RU of the

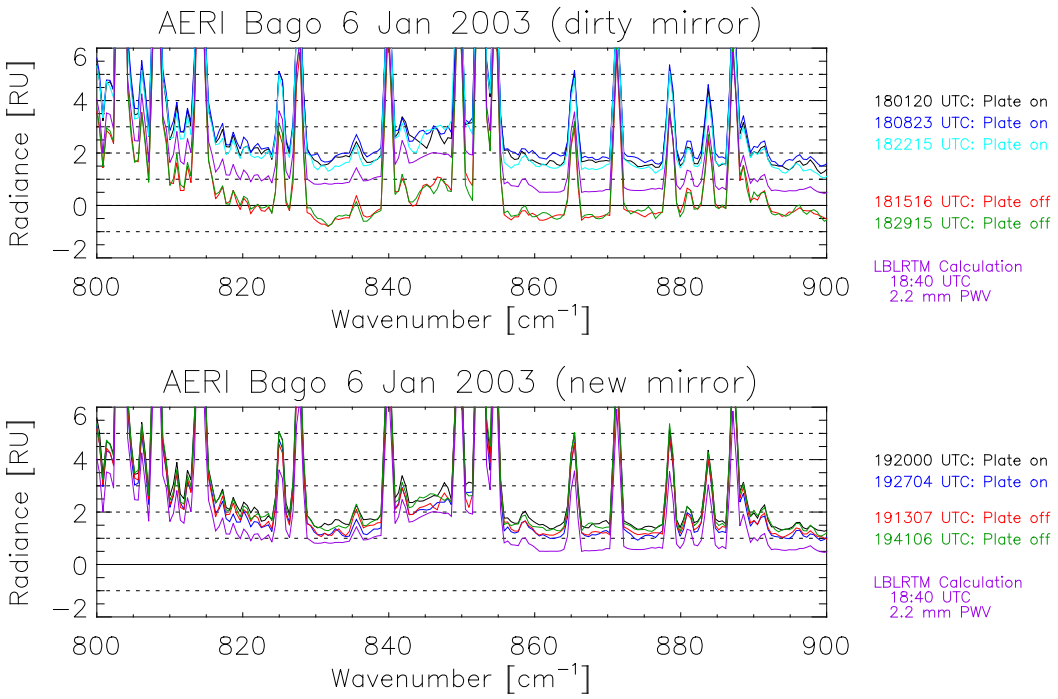

Figure 4.5: Spectra collected by the AERI at the University of Wisconsin-Madison on 6 Jan 2003 both with and without the sky aperture. Significant differences result when the scene mirror is dirty; however, when the scene mirror is clean the calibrated sky spectra are identical. The spectra collected when the mirror was clean (new) agree well with the data collected with the dirty mirror with the aperture in place.

radiance observed with the clean mirror, which could easily be explained by atmospheric changes that may have occurred in the 45 minutes (from 1830 UTC to 1913 UTC) it took to change the scene mirror. Therefore, the sky port aperture does not contribute a warm bias to the AERI and in fact is required for its accurate calibration.

It is possible that there is another obscuration in the sky FOV that would cause the warm bias in the SHEBA data. Tobin et al. (2000) used DABUL observations and variability tests on AERI data to select 62 clear sky scenes during SHEBA. Following Knuteson et al. (1999), the effective obstruction spectrum f_ν for each of these 62 cases is computed from

$$f_\nu = \frac{N_{obs} - N_{sky}}{B(T_{eff}) - N_{sky}} \tag{4.3}$$

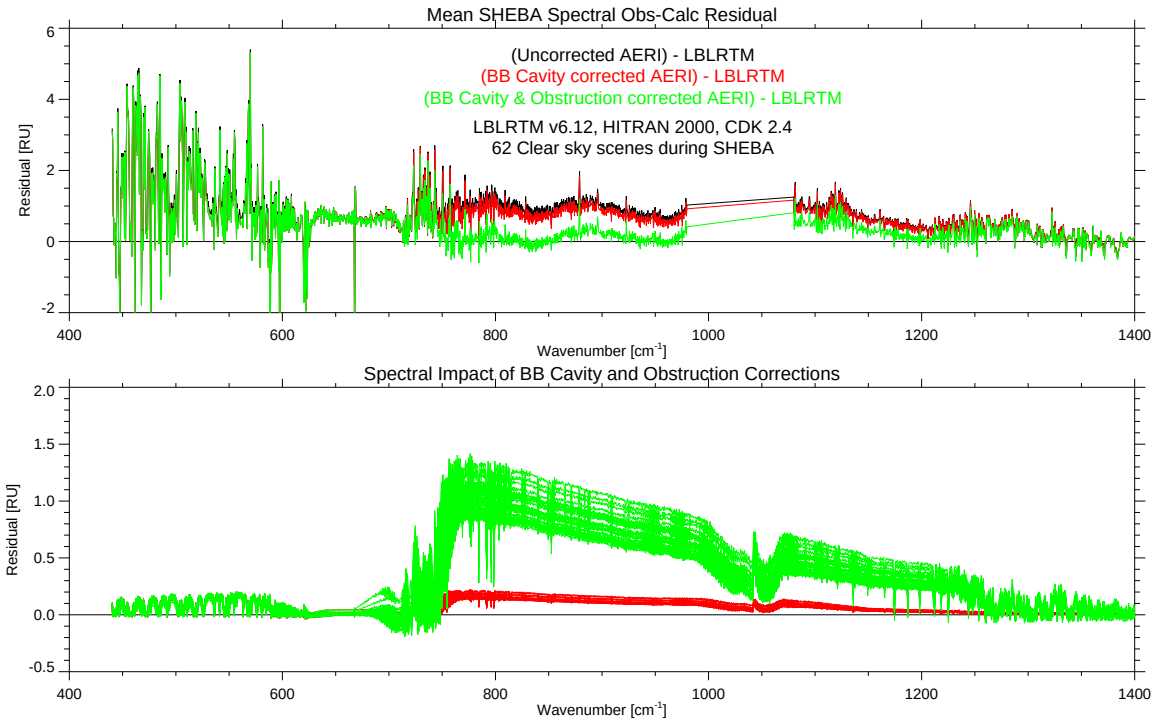

Figure 4.6: Mean AERI minus LBLRTM residuals for different corrected versions of the AERI observations (top), and the size and range of the different corrections (bottom) for 62 clear sky samples during the SHEBA experiment.

where N_{obs} is the observed (by the AERI) spectrum, N_{sky} is the "true" sky spectrum computed from the LBLRTM, T_{eff} is the effective temperature of the obstruction, and B is the Planck function. The temperature of the obstruction was taken to be the temperature of the blackbody support structure. The magnitude of f_ν compared to the magnitude of the correction discussed above for the improved blackbody model is shown in Figure 4.6. Note the relatively large spread in the obstruction correction f_ν. If the hypothesis that an obstruction is the source for the warm bias is true, then the variation in this correction should be correlated with either the instrument responsivity (4.2), temperature of the foreoptics, or perhaps PWV. However, as can be seen in Figure 4.7, the mean obstruction correction f_ν in a

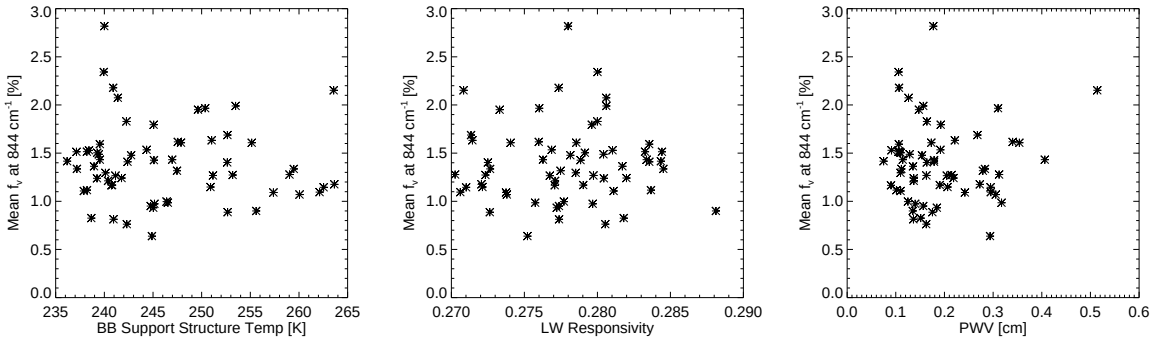

Figure 4.7: Correlation of f_ν at 844 cm^{-1} from equation (4.3) with the temperature of the blackbody support structure (left), longwave responsivity (middle), and PWV (right).

microwindow at 844 cm^{-1} is not correlated with any of these variables. Therefore, the hypothesis that there is an obstruction in the AERI's sky FOV during SHEBA was rejected.

Since trace gases and CFCs are not measured directly, climatological values are used in the LBLRTM calculations to account for the emission of these constituents in the infrared. CFCs, especially CFC-11 (CCl_3F) and CFC-12 (CCl_2F_2), are strong absorbers in the 8-13 μm region. However, these molecules absorb in bands that are not relatively smooth across the spectrum (Figure 4.8), and thus the relatively flat 1 RU bias can not be explained by errors in the amounts of these trace gases.

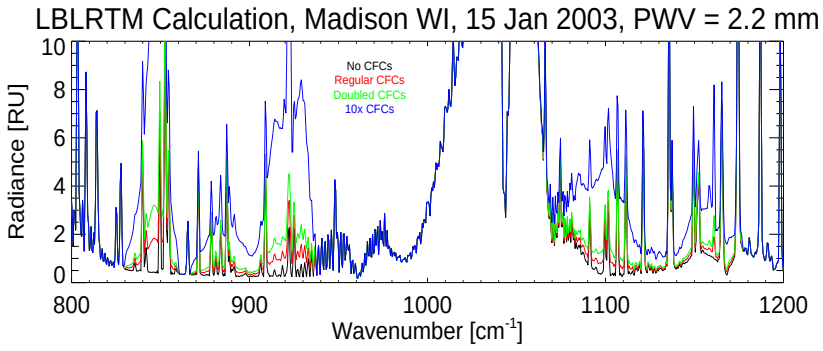

Figure 4.8: Downwelling radiance calculation in an Arctic atmosphere for different amounts of CFCs. Note that the spectral dependence of the CFC absorption occurs in discrete spectral regions.

Another possibility is that the emission source is in the atmosphere, either from thin cirrus, clear-sky ice precipitation (diamond dust), or

blowing snow. Diamond dust has been observed to exist quite frequently in the Arctic (Maxwell 1982, Curry et al. 1990). Using the LBLDIS model (discussed in Chapter 5), an iterative retrieval was used to retrieve the required optical depth and particle size for the diamond dust for the 62 (supposedly) clear sky SHEBA scenes. An example of the retrieval is shown in Figure 4.3. The retrieved particle size for each of the 62 cases was greater than 50 μm. The retrieved optical depths, which range from 0.05 to 0.10, are shown in Figure 4.9. These optical depths and particle sizes are reasonable values for diamond dust as well as for blowing snow, especially since the blowing snow will most likely be restricted to a very thin layer near the surface. If we assume that the spectral residuals shown in Figure 4.2 are due entirely to diamond dust then this implies diamond dust is present much more often than previously reported. Visual logs taken during the experiment reported diamond dust for some of these samples but not all, which suggests that diamond dust is not the source of the spectral bias in the residuals for all 62 of the samples. Finally, the spectral bias is about the same size at the SGP site, where diamond dust is certainly not a contributing factor. However, recent observations by the Atmospheric Infrared Sounder (AIRS) on the Aqua satellite over the SGP site also are slightly biased relative to the LBLRTM calculations (consistent with the AERI/LBLRTM comparisons), suggesting that there is an atmospheric component (most likely aerosols) that is not accounted for in the calculation (H.E. Revercomb, personal communication, 2003).

In summary, the approximate 1 RU bias between the AERI and the LBLRTM in clear sky conditions is probably not due to calibration errors in the instrument, but is most likely atmospheric absorption that is not accounted for in the calculation. The source of this absorption is probably different for the SHEBA data as compared to the SGP data, even

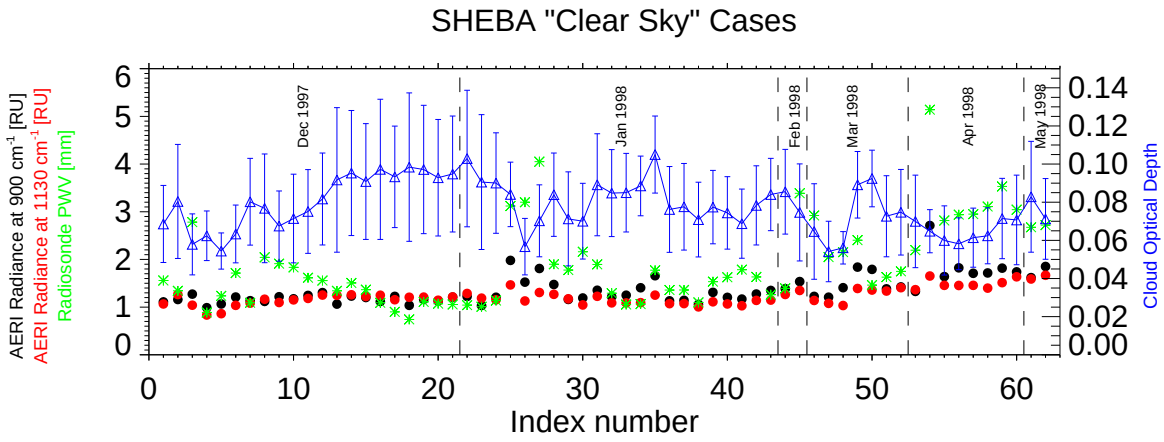

Figure 4.9: Optical depths retrieved from a simple two-channel retrieval assuming that diamond dust (i.e., ice crystals at the surface) are responsible for the approximately 1 RU bias in the 8-13 μm window. For all cases, the retrieved particle size was greater than 50 μm. Note that the optical depth is above 0.04 for all 62 clear sky cases.

though the spectral residuals between the observations and the calculations for the two locations are quite similar. The source of this bias remains under investigation.

Chapter 5

5. Cloudy sky radiative transfer

5.1. Forward modeling

Boundary layer clouds in the Arctic tend to be radiatively driven (Curry et al. 1996), and therefore these clouds are usually stratiform in nature. This structure allows the clouds to be modeled as plane-parallel clouds with less uncertainty than there would be if the clouds were convectively generated (Welch et al. 1980). To compute the radiation from a cloudy scene at high spectral resolution, the LBLRTM was coupled with the Discrete Ordinates Radiative Transfer model (DISORT; Stamnes et al. 1988). This routine, affectionately called LBLDIS, is able to compute the radiance emitted by the atmosphere at any altitude and viewing angle, and at arbitrary spectral resolution. The LBLRTM is used to calculate the monochromatic optical depths associated with the absorption by atmospheric gases in each vertical layer.

Since the calculations are performed with a computer, they are not truly monochromatic but are discrete. However, the LBLRTM computes optical depths with varying spectral resolution, as the Voigt half-width of the absorption lines changes rapidly with pressure, in order to maintain a nominal spectral sampling rate of four points per mean half width (Clough et al. 1992). For example, the spectral resolution for monochromatic optical depths for the U.S. Standard Atmosphere is approximately 0.01 cm^{-1} at the surface and 0.0008 cm^{-1} at 20 km.

The profiles of gaseous optical depth as a function of wavenumber are input into DISORT, along with the single scattering properties of the cloud layer(s), surface properties, etc., which then completes the radiative transfer calculation. The computed radiance must then be convolved with the AERI's instrument function (Figure 3.4) before the calculation can be compared with the observation.

5.2. Single scattering properties

The single scattering properties of cloud particles, the single scatter albedo, extinction coefficient, and asymmetry parameter, are required inputs to complete the radiative transfer in the cloudy scene. The single scattering properties of cloud particles are determined by the complex index of refraction ($m = m_r - im_i$), the particle size distribution, and the shape of the particles. In the infrared, the imaginary part of the refractive indices of liquid water and ice vary dramatically with wavelength, as shown in Figure 2.3. The absorption coefficient κ, which describes the cloud absorption and emission, is a function of wavelength λ and m_i and is given by (Bohren and Huffman 1983)

$$\kappa = 4\pi \frac{m_i}{\lambda}. \qquad (5.1)$$

The fact that the liquid water is more absorbing from 18-25 μm while the ice is more absorbing from 10-13 μm provide the basis for the discrimination of the cloud phase, as demonstrated in Chapter 6.

Historically, cloud particles have been treated as spheres so the scattering properties of these particles could be computed from Lorentz-Mie theory (Mie 1908), which is relatively

simple and well established. In fact, a well-tested and documented Fortran routine to compute the single scattering properties using this theory is available for general consumption (Wiscombe 1980). While the assumption of spherical shape is adequate for cloud water droplets, ice crystals are known to have shapes radically different than spheres. In the last several years, new computational procedures have been developed that allow the single scattering properties to be calculated for more realistic particle shapes (e.g., Yang and Liou 1996, Mishchenko et al. 1999, Baran and Havemann 1999, Yang et al. 2000, Yang et al. 2001, Yang et al. 2003b). In particular, Yang et al. (2001) have used a finite-difference time-domain (FTDT) procedure together with a stretched scattering potential method (SSPM) to compute the single scattering properties for hexagonal columns in the 8-13 μm region. A similar approach was used to compute single scattering properties for hexagonal columns for wavelengths longer than 15 μm (Yang et al. 2003c). Figure 5.1 presents a comparison of the single scatter albedo and asymmetry parameter integrated over gamma size distributions with different effective radii for ice in both the spherical and hexagonal column habits. Note that there is fair agreement between the two ice habits for both single scatter albedo and asymmetry parameter. This may be due to the fact that the aspect ratio is one for hexagonal columns with sizes less than 40 μm, and slowly changes from unity as the size of the maximum dimension increases (Yang et al. 2001). Observations by a Cloud Particle Imager (CPI) in springtime Arctic clouds indicate that many of the cloud ice particles are “spheroids” (Lawson et al. 2001) implying that the aspect ratio is close to unity, and thus the assumption made in the hexagonal column calculations appears valid for these clouds. However, Rangno and Hobbs (2001) presented in situ observations indicating that in an Arctic mixed-phase cloud, only 32% of the ice particles were pristine crystals, with the remainder being broken

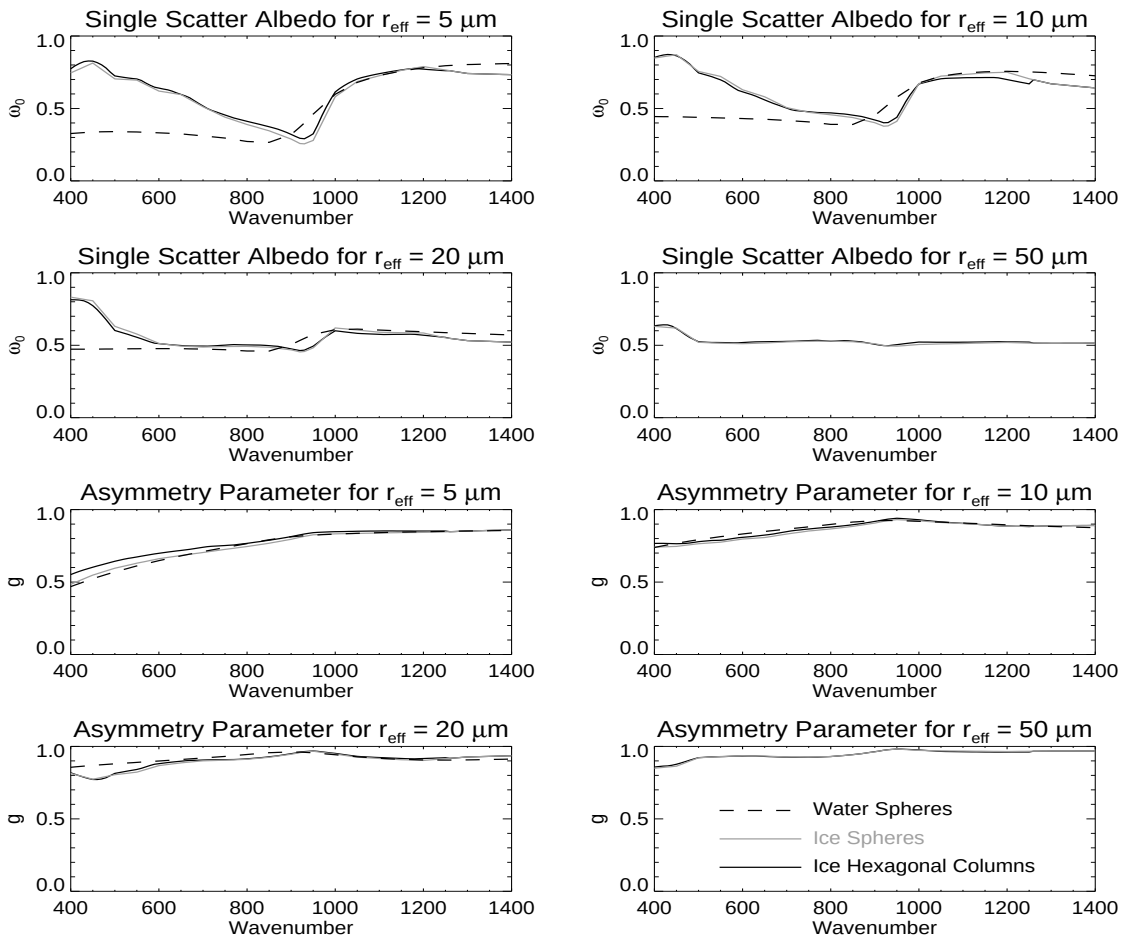

Figure 5.1: Spectral dependence of single scatter albedo and asymmetry parameter for water spheres, ice spheres, and hexagonal columns of ice for various effective radii.

pieces of needles or sheaths (10%), frozen drops (20%), aggregates or grauple (1%), or unidentifiable crystals (37%). Therefore, the assumption of a single crystal type in mixed-phase clouds is probably poor. Nonetheless, in this thesis, the ice particles will be assumed to be hexagonal crystals unless otherwise noted.

For sensitivity to phase determination, it is important that the single scattering properties for ice and water particles have differences in the spectral regions of the remotely sensed observations. Figure 2.3 demonstrates large differences between the imaginary refractive indices of water and ice, which translates into large differences between the

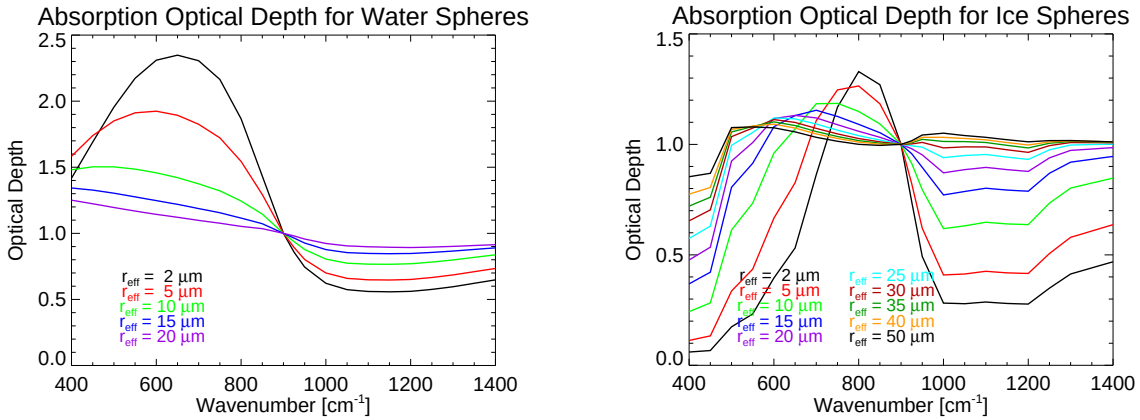

Figure 5.2: Absorption optical depth spectra for water (left) and ice (right) spheres for different effective radii.

absorption coefficients. In Figure 5.1, the single scatter albedo for water also demonstrates large differences between that for water and ice particles. Furthermore, Figure 5.1 also suggests that the single scattering properties change significantly with particle size. Therefore, is it possible to determine the phase of the cloud and also the effective size of the particles? Figure 5.2 illustrates that the absorption optical depth is a strong function of particle size for both ice and water particles, and therefore it may be possible to retrieve particle size for each habit from remote sensing observations that cover this spectral range. This possibility will be further investigated in Chapter 8. However, Figure 5.2 does illustrate the importance of the observations from 400-600 cm^{-1} (i.e., at wavelengths longer than 16 µm) for cloud phase determination.

Lorentz-Mie theory and the FTDT/SSPM provide the single scattering properties for cloud particles with a single phase. Mixed-phase clouds can be modeled in a variety of different ways. For example, a mixed-phase cloud could be treated as an internal mixture of ice and water, such as water coated ice particles, or could be modeled as an external mixture of ice and water particles. For the latter, there are three different ways to mix the particles;

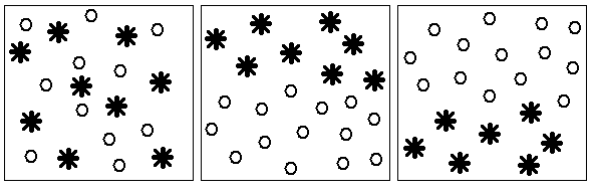

Figure 5.3: Three ways to model a mixed-phase cloud as an external mixture of ice (asterisks) and water (spheres) particles: uniformly mixed in volume, or as adjacent layers of ice over water or water over ice.

water and ice particles uniformly mixed in the same volume, an ice particle layer above and directly adjacent to a water droplet layer, and a water layer directly above and adjacent to an ice layer (Figure 5.3). Many mixed phase clouds consist of a thin liquid water layer with ice precipitating from the base, and thus treating the cloud as an external mixture is an adequate representation of these type of clouds. Furthermore, external mixtures allow the single scattering properties of the individual phases to be easily combined to create the single scattering properties for the mixed-phase cloud.

There are at least two different ways to combine the single scattering properties of the ice and liquid phases to create the scattering properties for a mixed-phase cloud. One way is to linearly combine the scattering properties as a function of cloud optical depth τ as demonstrated by Sun and Shine (1995):

$$\tau_m = \tau_i + \tau_w \tag{5.2}$$

$$\omega_{0,m} = \left(\tau_i \omega_{0,i} + \tau_w \omega_{0,w}\right) / \tau_m \tag{5.3}$$

$$g_m = \left(\tau_i \omega_{0,i} g_i + \tau_w \omega_{0,w} g_w\right) / \left(\tau_m \omega_{0,m}\right) \tag{5.4}$$

$$p_m = \left(\tau_i \omega_{0,i} p_i + \tau_w \omega_{0,w} p_w\right) / \left(\tau_m \omega_{0,m}\right) \tag{5.5}$$

where p denotes the scattering phase function and i, w, and m represent ice, water, and mixed-phase clouds, respectively. This method allows the scattering properties to be integrated over the size distribution of the individual phases a priori, and then the integrated scattering

properties are combined. Yang et al. (2003a) present an alternative method for deriving the scattering properties for the mixed-phase cloud by combining the scattering efficiencies of the ice and liquid phases before integrating over the combined size distribution. For this work, the mixed-phase clouds are modeled following the Sun and Shine method.

5.3. Cloud emissivity

Water vapor is an extremely strong absorber/emitter of radiation across the IR spectrum, and therefore any algorithm that attempts to ascertain cloud properties using observations in this spectral region must account for the water vapor. By utilizing cloud emissivity as the "observed" variable in any cloud property algorithm, the impact of changing water vapor burdens can be minimized. For downwelling radiation where a single, infinitesimally thin cloud exists and assuming the surface emissivity is close to unity (i.e., that the surface reflectance is close to zero), the radiative transfer equation is given by

$$\begin{aligned} R^{\downarrow} = \int_{p_s}^{p_c} B(T(p)) \frac{d\Im}{d\ln p} d\ln p + \\ \Im_{p_c}^{p_s} \varepsilon_c B(T_c) + \\ (1-\varepsilon_c - r_c) \int_{p_c}^{0} B(T(p)) \frac{d\Im}{d\ln p} d\ln p + \\ r_c \Im_{p_c}^{p_s} \left[B(T_s) \varepsilon_s \Im_{p_s}^{p_c} + \int_{p_c}^{p_s} B(T(p)) \frac{d\Im}{d\ln p} d\ln p \right] \end{aligned} \tag{5.6}$$

where ε_s and ε_c are the surface and cloud emissivities, B is the Planck function, $T(p)$ is the ambient temperature profile, T_s and T_c are the effective surface and cloud temperatures, p_c is the cloud base pressure, p_s is the surface pressure, $\Im$ is the transmission from the surface to

level p, $\Im_{p_c}^{p_s}$ is the transmittance from p_c to p_s, and r_c is the cloud reflectivity. The frequency dependence on all quantities other than T_c, T_s, T, and p is understood. The clear sky downwelling radiance is given by

$$\begin{aligned} R_{clr}^{\downarrow} &= \int_{p_s}^{0} B(T(p)) \frac{d\Im}{d\ln p} d\ln p \\ &= \int_{p_s}^{p_c} B(T(p)) \frac{d\Im}{d\ln p} d\ln p + \int_{p_c}^{0} B(T(p)) \frac{d\Im}{d\ln p} d\ln p \end{aligned} \tag{5.7}$$

and thus

$$\begin{aligned} &\varepsilon_c \left(\Im_{p_c}^{p_s} B(T_c) - \int_{p_c}^{0} B(T(p)) \frac{d\Im}{d\ln p} d\ln p \right) = \\ &R^{\downarrow} - R_{clr}^{\downarrow} - r_c \left(\left(\Im_{p_s}^{p_c} \right)^2 B(T_s) \varepsilon_s + \Im_{p_s}^{p_c} \int_{p_s}^{p_c} B(T(p)) \frac{d\Im}{d\ln p} d\ln p - \int_{p_c}^{0} B(T(p)) \frac{d\Im}{d\ln p} d\ln p \right) \end{aligned} \tag{5.8}$$

Since most of the water vapor is near the surface, the level-to-surface transmittance term $\Im_{p_c}^{p_s}$ typically can not be assumed to be unity. However, depending on the height of the cloud, the wavelength of radiation, and the amount of water vapor, we can often assume that $\int_{p_c}^{0} B(T(p)) \frac{d\Im}{d\ln p} d\ln p \approx 0$. Also, the atmospheric terms are typically much smaller than the surface term in the expression that is multiplied by the cloud reflectivity (on the right hand side), and thus can be neglected. These assumptions allows us to express the cloud emissivity, computed from downwelling radiance observations at the surface, as

$$\varepsilon_c = \frac{R^{\downarrow} - R_{clr}^{\downarrow} - r_c \left(\Im_{p_s}^{p_c} \right)^2 B(T_s) \varepsilon_s}{\Im_{p_c}^{p_s} B(T_c)}. \tag{5.9}$$

The level-to-surface transmission term complicates the derivation of the cloud emissivity. In the Arctic, this term is very close to unity for channels between 8-13 μm due to the very low amounts of water vapor present and thus can be assumed to be one. This term cannot be set to

unity in the 17-25 μm region due to the strength of the water vapor absorption in this spectral region.

5.4. Computing cloud reflectivity

Cloud reflectivity in the infrared is fairly small and generally assumed to be negligible (e.g., DeSlover et al. 1999, Smith et al. 1999). However, since Arctic clouds are close to the surface (usually within the lowest 1 km) and the surface emits a significant amount of radiation, the cloud reflectivity should not be ignored. To compute the cloud reflectivity, we hold the cloud properties constant and perturb the surface radiance term $\varepsilon_s B(T_s)$ in LBLDIS. Since the left hand side of equation (5.8) is unchanged for the two calculations (because the cloud properties are held constant), we can set the two calculations equal to each other and rearrange to solve for r_c as

$$r_c = \frac{R_1^{\downarrow} - R_2^{\downarrow}}{\left(\Im_{p_c}^{p_s}\right)^2 \left(B(T_{s,1})\varepsilon_{s,1} - B(T_{s,2})\varepsilon_{s,2}\right)} \tag{5.10}$$

where $R_1^{\downarrow}$ and $R_2^{\downarrow}$ are the downwelling radiance calculations for the corresponding surface conditions. This allows the spectral cloud reflectivity to be calculated. It should be noted that perturbing the surface temperature by 1, 10, or 20 K yields almost exactly the same reflectivity spectrum, as do reasonable (i.e., < 10%) changes in the surface emissivity.

The cloud reflectivity spectrum is a function of the single scattering properties of the clouds. Examples of cloud reflectivity spectra are given in Figure 5.4. Ice clouds have significantly more reflectance from 400-550 cm^{-1} than liquid water clouds, which is consistent

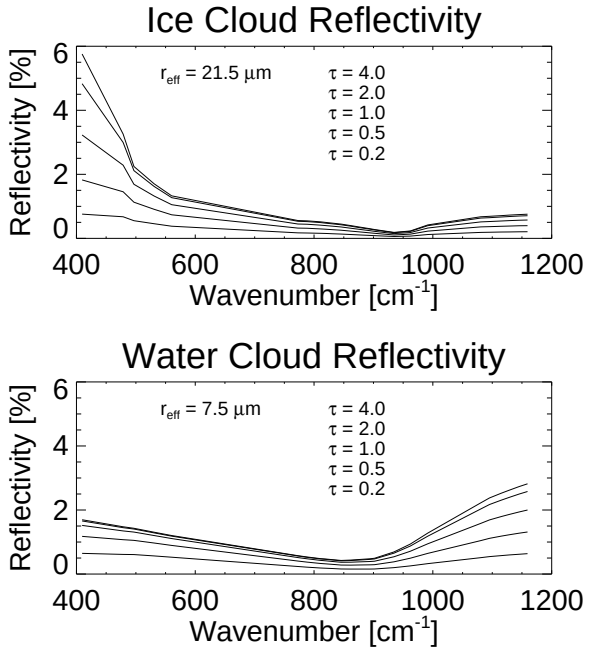

Figure 5.4: Cloud reflectivity spectrum for various optical depths for ice (top, r_e = 21.5 µm) and water (bottom, r_e=7.5 µm) clouds.

with the fact that ice is less absorbing in this spectral region. Also note that the reflectivity spectrum is a function of optical depth, but that the differences between the spectra at optical depths above 5 are very small. The reflectivity spectra associated with optically thick clouds are consistent with the results from Herman (1980), who indicated that the infrared broadband cloud reflectivity approaches a maximum value of 2% for optically thick clouds.

5.5. Minimum local emissivity variance (MLEV)

To calculate cloud emissivity from an observed radiance spectrum, a clear-sky radiance spectrum, the cloud-to-surface transmission spectrum, and the effective cloud temperature must be known. There are two options for the clear sky spectrum: use an observed clear sky observation that is close in time to the cloudy observation, or use a calculation from a model such as the LBLRTM. Since clouds in the Arctic are typically stratiform, they can exist for long periods of time and thus the latter approach is preferred.

Furthermore, the cloud-to-surface transmittance can not be observed directly from a remote sensing instrument and must be calculated.

There are multiple ways to estimate the cloud temperature. If active remote sensor (i.e., radar or lidar) cloud boundaries are available, as well as a thermodynamic profile (which is required for the calculation anyway), then an effective cloud temperature can be assigned. However, the assigned temperature may not be consistent with the radiation observed by a ground-based instrument, because the effective temperature observed by the AERI will shift towards the lower cloud boundary as the optical depth of the cloud increases. This is due to the "linear-in-optical depth" nature of the radiative transfer in a medium (Wiscombe 1976, Ridgway et al. 1991, Clough et al. 1992). A more consistent approach is to compute the cloud effective temperature directly from the observed radiance spectrum. An iterative technique of this nature has been developed called the minimum local emissivity variance (MLEV) method (Tobin et al. 1999b, Huang et al. 2001, 2003). The MLEV method is independent of cloud boundary information and can be used to determine cloud temperature where neither a lidar nor radar is available. The basic technique is illustrated in Figure 5.5. A spectral region is chosen that has both weak and strong water vapor absorption lines, such as between 780-800 cm^{-1}. The cloud emissivity is then computed using (5.9) for a range of temperatures, say from 200 – 320 K by 0.1 K increments, and assuming that $\Im_{p_c}^{p_s}$ is unity. Figure 5.5 demonstrates how the absorption features associated with water vapor are translated into the emissivity spectrum when the temperature used to compute ε_c is either too high or too low. For each temperature, the standard deviation of the mean emissivity is computed across the spectral region. The temperature that has the lowest standard deviation yields the effective cloud temperature. This method assumes that the cloud emissivity is smoother spectrally compared

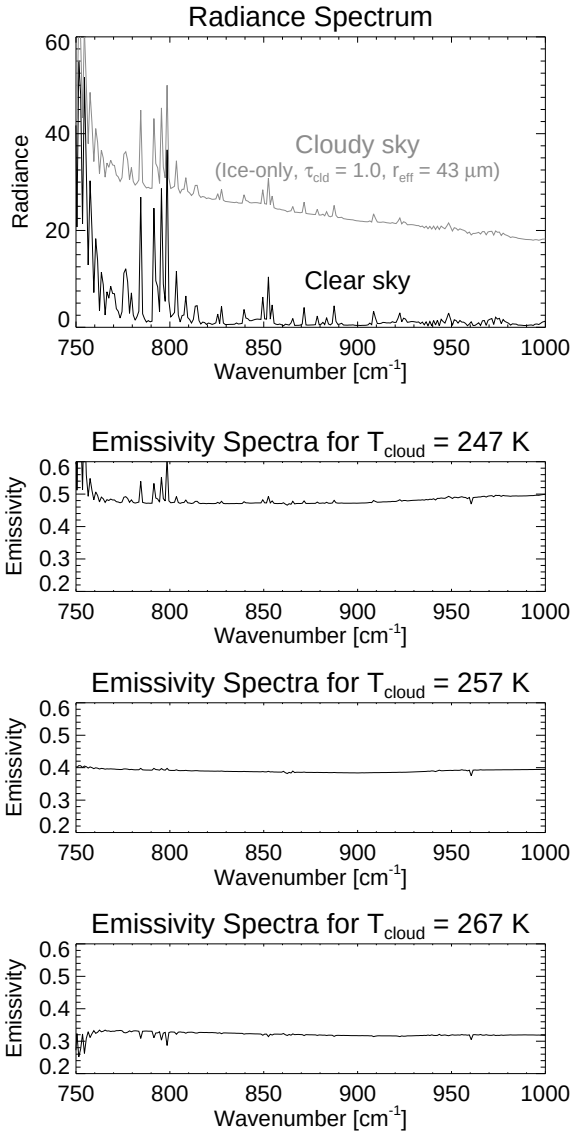

Figure 5.5: Downwelling radiance spectrum for a clear and cloudy scene, along with the cloud emissivity derived at three different temperatures. Note the disappearance of the line absorption structure from 780-800 cm^{-1} when the cloud temperature is accurately determined. This is the concept of the MLEV method.

with the gaseous absorption. If the derived cloud temperature is one of the bounds of the iteration (i.e., either 200 or 320 K) then the MLEV routine did not converge to a solution and thus another method must be used to determine the cloud temperature.

The MLEV technique is an excellent way to get estimates of the cloud temperature when the assumptions are valid. However, the assumption that the transmission between the surface and the cloud equals 1 across the MLEV range breaks down on the absorption lines themselves. As the cloud moves higher into the troposphere, more water vapor exists between the cloud and the surface, and this non-negligible absorption causes biases in the MLEV results. From the ground-based sensor point of view, the MLEV method may overestimate the cloud temperature (the size of the overestimate depends on how much water vapor is between the cloud and surface), resulting in an underestimate of the cloud emissivity.

However, since the total water vapor is relatively small in the Arctic and most Arctic clouds have bases less than 1 km above ground level (Intrieri et al. 2002), estimating the cloud temperature with the MLEV method is very appealing.

5.6. Sensitivity to size distribution

The use of remote sensing observations to retrieve cloud microphysical properties typically involves many assumptions. One of these assumptions is the form of the size distribution of the cloud particles. For spherical particles, the effective radius is defined as

$$r_{eff} = \frac{\int r^3 n(r) dr}{\int r^2 n(r) dr}. \tag{5.11}$$

It has been shown (e.g., Mitchell 2002) that clouds that have identical effective radii and identical integrated water paths can have widely different values for the extinction and absorption scattering efficiencies when integrated over different size distributions. However, radiative transfer codes such as DISORT often use single scatter albedo, which is defined as

$$\omega_0 = \frac{\overline{Q}_{sca}}{\overline{Q}_{ext}} = \frac{\int (Q_{ext}(r) - Q_{abs}(r)) r^2 \, n(r) \, dr}{\int Q_{ext}(r) \; r^2 \, n(r) \, dr} \tag{5.12}$$

in the radiative transfer calculations, rather than the scattering efficiencies. Are these differences in the scattering efficiencies important in the retrieval of cloud properties in the infrared?

To address this question, four different size distributions were constructed to have widely varying widths and mode radii so that the effective radius of each was 7.0 μm and the ice water path of 99.0 g m^{-3}. Spherical ice particles were used in these size distributions. This

combination of effective radius and ice water path results in an optical depth of approximately 1 at 900 cm^{-1}. The U.S. Standard Atmosphere was used to define the atmospheric state, the cloud was inserted at 2.1 km, and the downwelling radiance was computed for each size distribution using LBLDIS. From the downwelling radiance calcuations, the cloud emissivity spectra were computed, assuming that the cloud temperature was the geometric mean temperature. The differences in the emissivity spectra, shown in Figure 5.6a, demonstrate that there are differences in the emissivity spectra but that these differences are at most 0.03 between the widest distribution (i.e., the one with the most large particles) and the narrowest. Note that the differences in the emissivity between any of the two size distributions are relatively constant across the spectrum. The experiment was repeated for a larger effective radius of 24.0 μm and an ice water path of roughly 277 g m^{-3} (which again has an optical depth of approximately 1 at 900 cm^{-1}) and yielded similar results (Figure 5.6b). However, this case shows some spectral variation in the emissivity between the narrowest and widest size distributions. This spectral signature is due to the fact that the widest size distribution (the lognormal size distribution with a sigma value of 2.0) has a much larger number of small particles that are required compensate for the large particles in the distribution to yield an effective radius of 24.0 μm. These results suggest that while there is some slight sensitivity to the size distribution of the cloud particles, little error is added to the emissivity spectrum by an incorrect assumption regarding the shape of the size distribution. This is especially true given the uncertainty in the calculated cloud emissivity spectrum, which typically ranges from 2%-6% across the 8-13 μm window for reasonable uncertainties in the observations (Chapter 8).

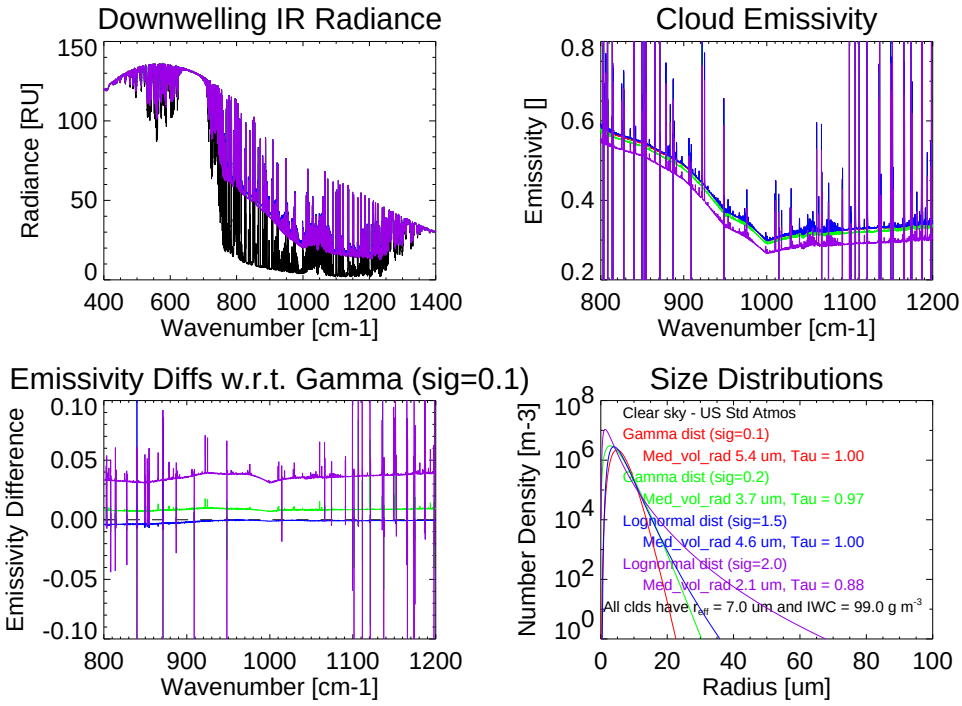

A

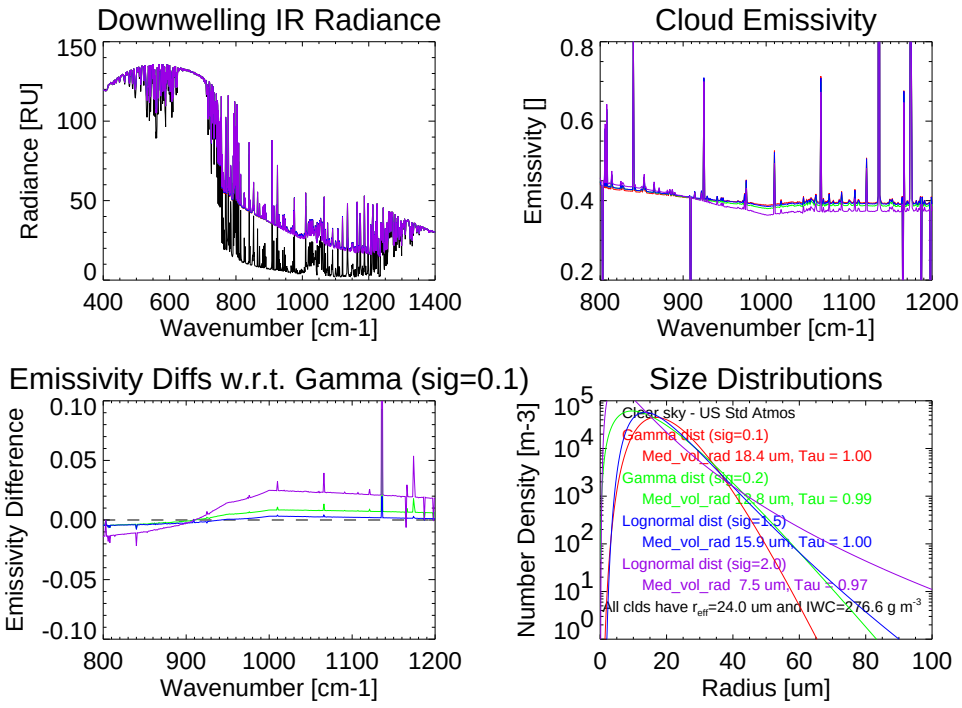

B

Figure 5.6: Sensitivity of the downwelling radiance spectra and cloud emissivity spectra to changes in the cloud particle size distributions. In each case, all of the clouds have same effective radius and ice water content (IWC). A*: r_e = 7.0 μm and IWC = 99 g m^{-3}.* B*: r_e = 24.0 μm and IWC = 276.6 g m^{-3}.*

Chapter 6

6. Cloud Phase Determination

6.1. Three-channel threshold test

Chapter 5 reviewed how one could compute the downwelling radiance at high spectral resolution for a cloudy sky scene using DISORT and LBLRTM. Since water vapor is highly absorbing in the infrared, the radiance at the surface from two atmospheres with identical clouds but differing amounts of precipitable water vapor will differ; therefore, for cloud studies it is more convenient to work with the cloud emissivity spectrum. To compute the cloud emissivity the effective temperature of the cloud must be known, but this can be computed directly from the observed radiance data for most Arctic clouds.

Cloud phase determination from remote sensing data takes advantage of the differences in the absorption coefficient of ice and liquid water across the spectrum. From 8 – 10 μm, the absorption coefficient is almost identical for liquid and ice (Figure 2.3), and thus the emission from two clouds where the particle distribution and number density were the same would be identical in this spectral region. From 10-13 μm, ice is more absorptive than water, which various studies (e.g., Baum et al. 2000, Strabala et al. 1994) have suggested for phase discrimination. However, absorption is also a strong function of particle size, and smaller particles (either ice or water) typically have larger absorption in this region, and thus it is difficult to determine whether the enhanced signal at 12 μm is due to ice particles or small liquid water droplets based upon observations in the 8-13 μm window alone. The

spectral region from 16-25 μm is rather unique across the spectrum, as it is one of the relatively few areas where water is more absorptive than ice and the atmosphere is transparent enough for remote sensing. Another such spectral region that is currently being exploited is between 850 – 1050 nm (Daniel et al. 2002).

As shown in Figure 2.3, both the standard and extended range AERIs make observations in the 16-25 μm window. However, Figure 2.3 also suggests that the window becomes less transparent to cloud radiation as the PWV increases. Figure 6.1 shows clear-sky brightness temperature spectra from the SGP (where the range of PWV is larger than in the Arctic), demonstrating how the microwindows in the far IR, including the most transparent one centered at 560 cm^{-1} (17.8 μm), close as the PWV increases. When the PWV is approximately 1.0 cm, the brightness temperature difference (BTD) between the center of the microwindow at 560 cm^{-1} and the nearby opaque lines is approximately 25 K, and the BTD decreases to less than 20 K for PWV greater than 1.5 cm. Therefore, any cloud retrievals that

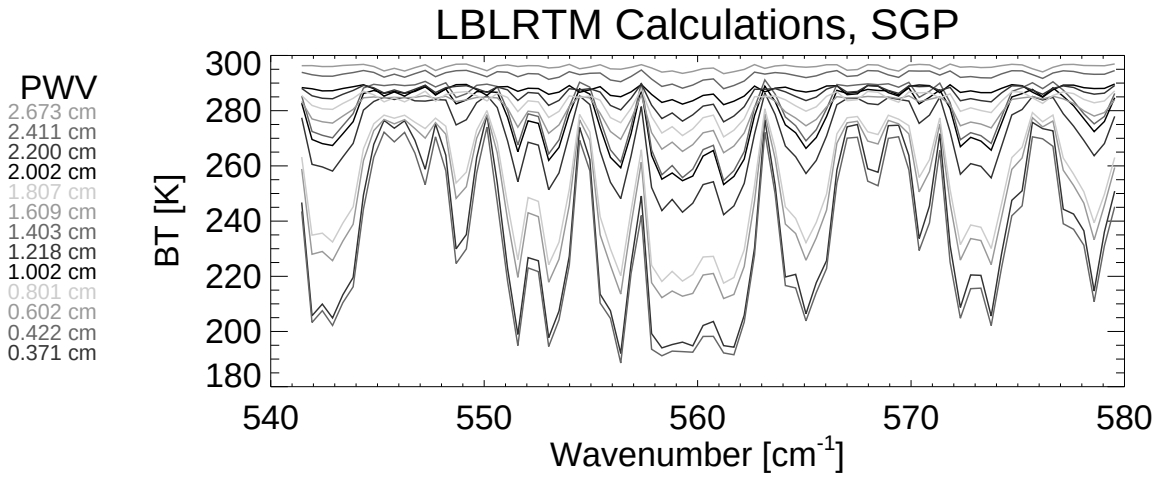

Figure 6.1: Observed brightness temperature spectra centered around 17.8 μm (560 cm^{-1}) for various water vapor burdens. Note how the 17.8 μm microwindow starts to close as the PWV exceeds 1 cm.

utilize ground-based observations in this spectral region will probably be restricted to conditions where the PWV is less or equal to about 1.0 cm. PWV below these amounts are typically found in the Arctic for most of the year with the exception of some summertime periods (Serreze et al. 1995). However, cloud property retrievals that use upwelling radiation (i.e., observations from aircraft or satellites) in this spectral band will be less sensitive to PWV as a large fraction of the water vapor will be below the cloud.

Radiance observations in the 16-25 μm window, in addition to observations in the 8-13 μm window, allow cloud phase observations to be determined unambiguously. Radiance from two cloudy scenes was computed using the LBLDIS model where both clouds have approximately the same optical depth ($\tau_{cloud} \approx 2.0$ at 900 cm^{-1}), the same particle size distribution, and approximately the same effective radius (10 μm). One cloud consisted of spherical ice particles and the other water droplets. The downwelling radiance and brightness temperature spectra for each are shown in Figure 6.2. The emissivity of both clouds is approximately the same from 800 – 1250 cm^{-1} (where the absorption coefficients are the same), but the cloud emission is larger for the water cloud from 400-600 cm^{-1} than the ice cloud. The large radiance difference (approximately 10-15 RU) between the water and ice clouds in the 400-600 cm^{-1} range is significantly larger than the uncertainty in the AERI-ER radiance observations (Figure 3.5).

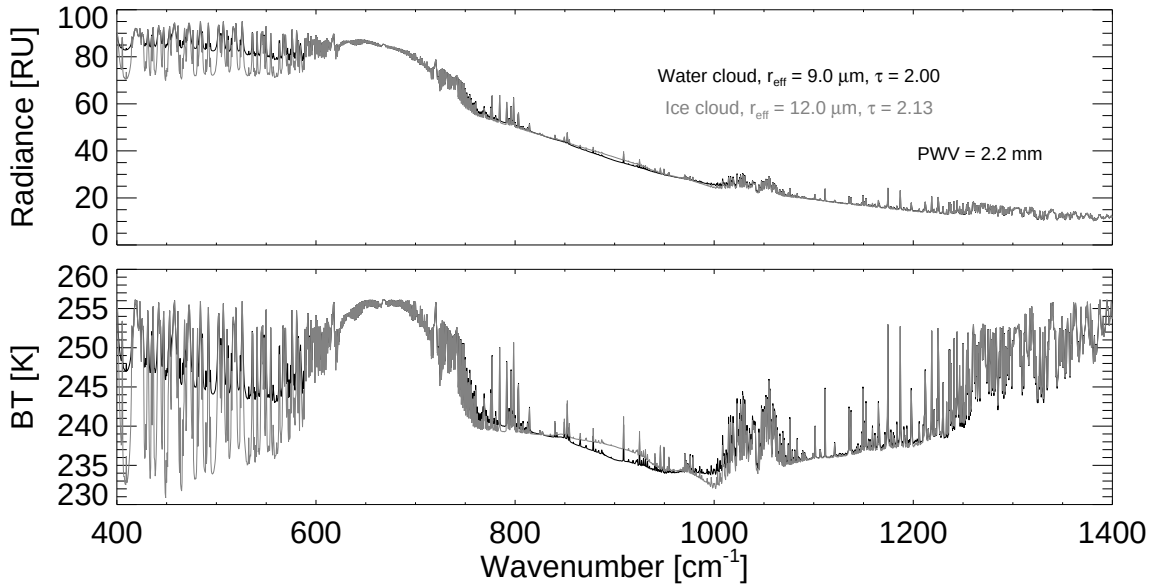

Figure 6.2: Downwelling radiance (top) and brightness temperature (bottom) spectra for a ice (gray) and water (black) cloud. The observations between 400-600 cm^{-1} are required for unambiguous phase determination.

Errors in the determination of the cloud's phase can have a large effect on the outgoing top-of-the-atmosphere and the downwelling longwave flux at the surface, due to the difference in the absorption coefficients in the 16-25 μm region. Table 6.1 demonstrates the differences in the these fluxes between ice and water clouds, assuming that the ice and water clouds have optical depths and particle sizes such that the downwelling longwave flux at the surface between 8-13 μm is identical for each cloud (such as the example in Figure 6.2). Note that the differences are largest when the optical depth of the cloud at 900 cm^{-1} is approximately unity, and that the differences decrease to zero as the cloud becomes totally opaque or transparent. The maximum cooling rate difference is also largest for a cloud with an optical depth of approximately 1. A large fraction of the clouds in the Arctic are semi-transparent in the infrared (Chapter 9), and thus accurate phase determination is critical to accurately calculate the radiative energy budget, and thus for detecting climate trends. For

example, when the optical depth of the cloud is approximately 1, a doubling of carbon dioxide results in an approximate 4.9 W m^{-2} change in the outgoing longwave flux. Therefore, errors in the radiative budget due to the incorrect determination of the cloud phase are larger than the signature of climate change by CO_2 doubling.

Table 6.1: Flux calculations were made using the RRTM (Mlawer et al. 1997), a rapid radiative transfer model that has been extensively validated with the LBLRTM in clear skies. The RRTM uses non-gray parameterizations for both water clouds (Hu and Stamnes 1993) and ice clouds (Fu et al. 1998). As in Figure 6.2, the effective radius of the water and ice particles is 9 μm and 12 μm, respectively. The IWP was set to yield the approximate optical depths, and the LWP was selected such that the difference in the surface downwelling flux from 8-13 μm for the ice and water clouds was zero. The flux and cooling rate differences (diffs) were computed as ice cloud minus water cloud, and the relative differences are given in parentheses in terms of percent. The cloud was modeled as a 100 m thick cloud at 700 m AGL.

IWP [g m^{-2}]	Optical Depth	TOA Flux Diff [W m^{-2}]	Surface Flux Diff [W m^{-2}]	Maximum Cooling Rate Diff [K day^{-1}]
120.0	~16	0.08 (0.0%)	-0.02 (0.0%)	-0.2
29.6	~4	1.72 (0.8%)	-2.21 (-1.0%)	-1.8
14.8	~2	5.31 (1.9%)	-4.14 (-1.9%)	-5.2
7.4	~1	7.15 (2.0%)	-4.75 (-2.3%)	-7.1
3.7	~0.5	6.39 (1.5%)	-3.90 (-2.1%)	-6.5
1.8	~0.2	4.17 (0.9%)	-2.50 (-1.4%)	-4.4

Downwelling radiance spectra were computed with the LBLDIS model for a large set of different single-phase clouds (ice or water). The optical depths ranged from 0.1 to 8, and the particle effective radii ranged from 3-15 μm for water droplets, and 7-50 μm for ice particles. Cloud emissivity spectra were computed and examined. The calculations were only made in a selected set of microwindows (see Table 6.2) to avoid line absorption by water vapor and other atmospheric gases. Examples of some of these spectra are shown in Figure 6.3.

Table 6.2: Center wavelength and wavenumber ranges for each microwindow used in the threshold-based phase determination algorithm.

Center wavelength [μm]	Wavenumber range [cm^{-1}]	Center wavelength [μm]	Wavenumber range [cm^{-1}]
20.13	495.5-498.0	11.44	873.2-875.5
18.84	529.9-531.5	11.09	898.5-904.7
17.85	558.5-562.0	9.12	1095.0-1098.2
12.02	830.0-834.5	8.97	1113.5-1116.1
11.83	843.0-847.5	8.12	1231.3-1232.2

Several spectral features are apparent in Figure 6.3. First, the slope of the emissivity spectra from 800-900 cm^{-1} is much steeper for the liquid-only clouds than for the ice-only clouds. This is due to the fact that the water droplets used in these calculations are smaller than the ice particles (which is typical in the atmosphere), as ice-only and water-only clouds with identical effective sizes would have approximately equal slopes in this spectral region (Figure 6.2). Since the liquid water absorption is much stronger than ice absorption in the 16-

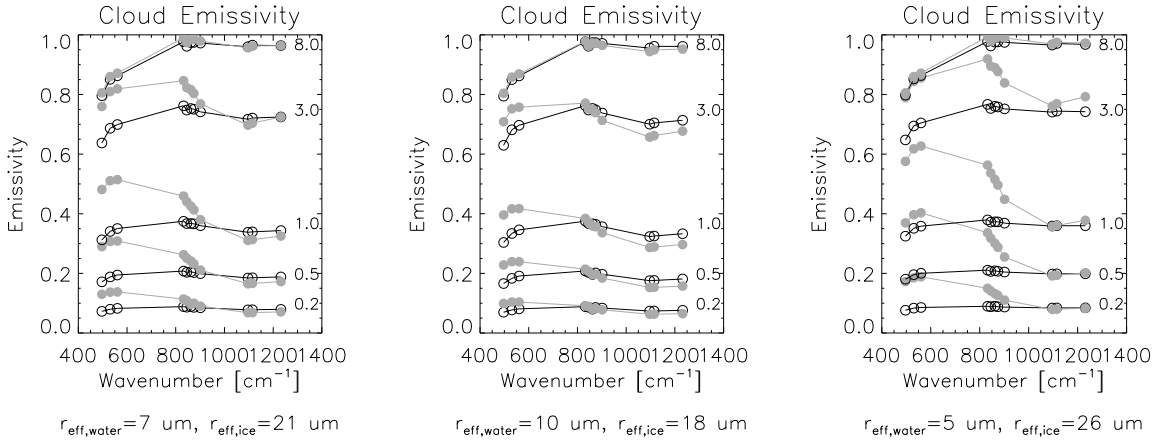

Figure 6.3: Cloud emissivity spectra, calculated in selected microwindows, for various clouds. The particle sizes for the ice (open circles) and water (solid circles) are given at the bottom, while the optical depth (at 900 cm^{-1}) for each cloud is given on the right.

25 μm window, there are differences in the values of the cloud emissivity between 850 cm^{-1} and 550 cm^{-1} for water and ice clouds.

These simulations were used to develop three criteria for determining whether a cloud observed by the AERI was ice-only, liquid-only, or mixed-phase. The first test (Figure 6.4, left) determines the phase by considering the slope of the emissivity in the four microwindows in the 11-12 μm region. If the slope of the emissivity in this spectral region is considerably negative, then the effective size of the cloud particles is small and the cloud is classified as a liquid water cloud. If the slope is close to zero, then the cloud particles are large and the cloud is identified as an ice-only cloud. Clouds with intermediate slopes are identified as mixed-phase clouds.

While particle size is a good indicator of cloud phase, particle size alone should not be used for phase determination as some ice clouds are composed of very small ice particles and thus have very steep slopes in this spectral region (Smith et al. 1993b, Smith et al. 1998). To

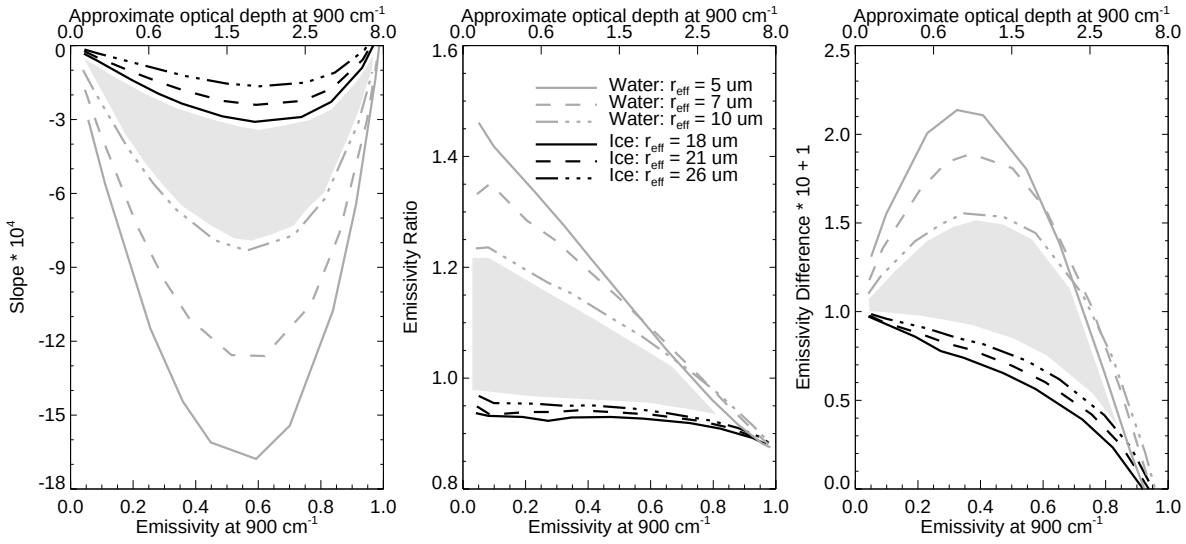

Figure 6.4: Threshold regions for the three tests to determine cloud phase. See text for details.

eliminate any ambiguity of cloud phase with particle size, the other two tests utilize observations in the 16-25 μm region together with observations in the 10-13 μm region. The second test (Figure 6.4, center) determines cloud phase based on the value of the ratio of the mean cloud emissivity in the 17-19 μm region to the mean cloud emissivity in the 11-12 μm region. If the ratio is below approximately 1.0, the cloud is identified as an ice-only cloud, but if the ratio is quite large then the cloud is identified as a liquid water cloud. Again, the intermediate region is associated with mixed-phase clouds. This test is quite sensitive to cloud with small optical depth (and hence small values of emissivity at 900 cm^{-1}). The third test (Figure 6.4, right) uses the difference of the mean emissivity between 17-19 μm and 11-12 μm. This test provides improved sensitivity to clouds of intermediate optical depth, as compared to the second test. Note that both the second and third tests are true phase tests, because as the curves associated with larger water droplets move towards the center, the curves associated with the smaller ice crystals move away from the center and thus there is no convergence on particle size.

The algorithm combines these three tests to yield a single cloud phase determination. If any two tests agree on cloud phase, then the cloud is classified as that phase, but if all three disagree then the cloud's phase is identified as ambiguous. All three tests become insensitive to cloud phase when the optical depth becomes larger than approximately 6, so clouds that have an emissivity at 900 cm^{-1} larger than 0.95 are classified as opaque.

6.2. Validation with simulations

To evaluate the phase determination algorithm, observations were simulated from a number of different cloud conditions. The optical depth of the clouds ranged from 0.1 to 8.0. For each optical depth, the fraction of the optical depth that was due to liquid water ranged from 0.0 (ice-only cloud) to 1.0 (liquid-only cloud) in increments of 0.1. The simulated data set was arranged so that the first case was a clear sky case, the next 11 cases were ice-only clouds where the optical depth slowly increased over the range, followed by the 11 cases of liquid-only clouds for the same optical depths. The next eleven segments each have nine cases, where the total optical depth for the segment is fixed (starting at 0.1, 0.2, 0.5, up to 8.0) and the fraction of the optical depth associated with ice starts at 0.1 and increases to 0.9. The ice and liquid optical depths for the cases just described are shown in the bottom of Figure 6.5. The atmospheric state used in the model runs is from a radiosonde observation at SHEBA on 25 April 1998; the precipitable water vapor is 2.44 mm. The clouds are placed between 600-700 m where the temperature is –16 C. Gamma size distributions with effective radii of 21 and 7 μm are used for the ice and water particles, respectively, as suggested by in situ observations made in May 1998 at SHEBA (Figure 6.6) by the Cloud Particle Imager (Lawson et al. 2001).

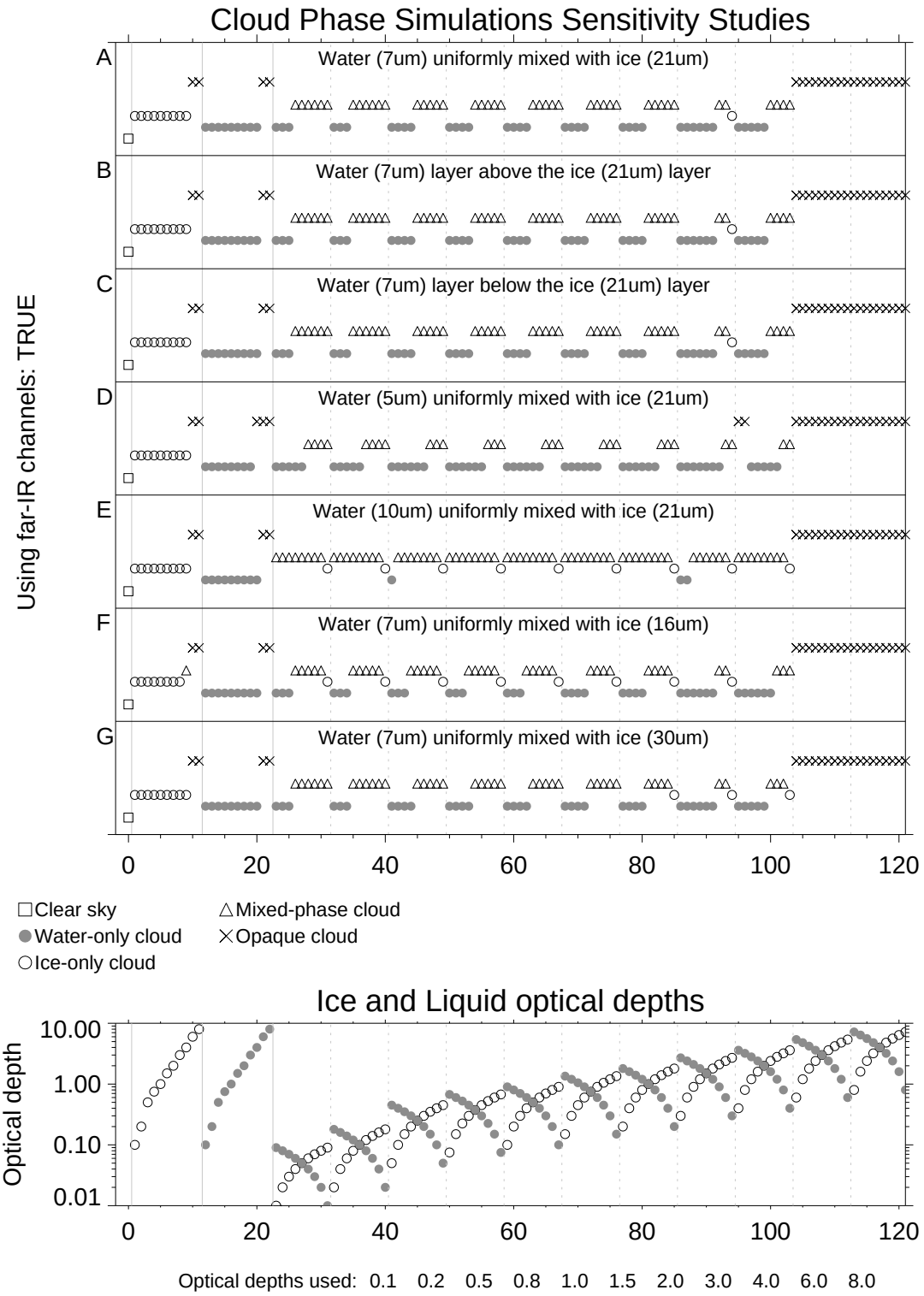

Figure 6.5: (A-G) Results from the phase determination algorithm for 122 different simulated clouds (bottom panel), for changes in cloud layering or particle size. See text for details.

Panel A in Figure 6.5 demonstrates the results for the phase determination algorithm for this case. When the cloud is entirely ice, the phase correctly determined for all optical depths less than 5, after which the cloud is classified as opaque. Similarly, the liquid water clouds are correctly determined for optical depths less than 5. In this simulation, the mixed-phase clouds were modeled as an external uniform mixture of ice and water particles in the same volume (Figure 5.3). For these mixed-phase clouds, the algorithm correctly classifies the cloud as mixed-phase for the entire range of optical depths, as long as the fraction of the optical depth due to the ice particles is significant (i.e., greater than ~40%). When the fraction of the optical depth due to liquid water is greater than 60%-70%, the cloud is misclassified as a liquid water cloud.

Additional sensitivity studies were performed to further evaluate the algorithm's performance (Figure 6.5). For the same simulation setup as before, the composition (layering of the mixed phase cloud or effective particle size) of the clouds were altered. With the

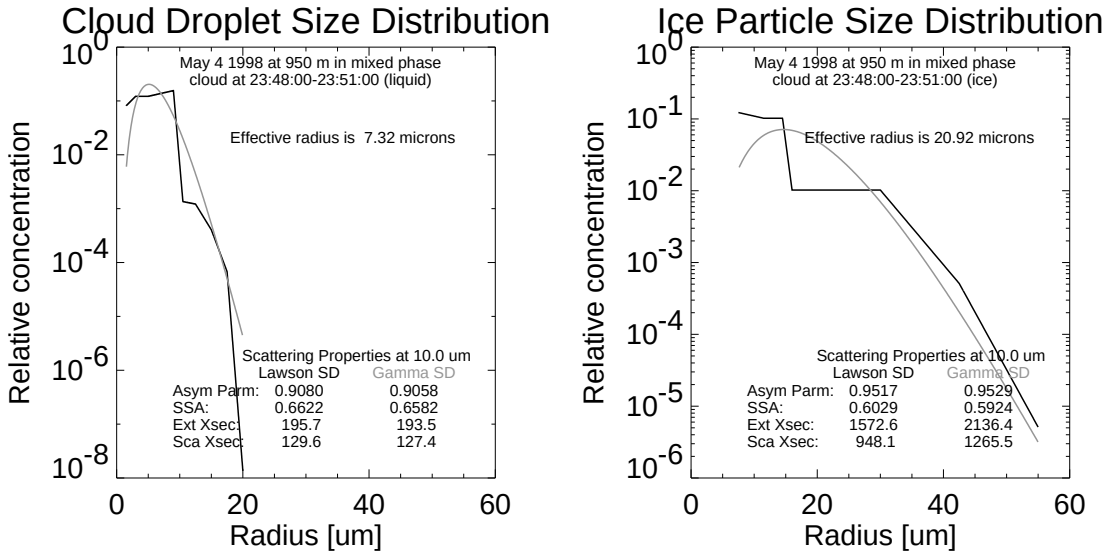

Figure 6.6: Size distributions of water (left) and ice (right) particles in a mixed-phase cloud observed by the Cloud Particle Imager (CPI) over the SHEBA ship on 4 May 1998. The observed size distributions are well approximated by a gamma size distribution.

results in Figure 6.5a providing a baseline, the results from the algorithm for these changes in layering and particle size were evaluated. In many mixed-phase clouds, the particles are not uniformly mixed in a volume, as this is inherently unstable due to the difference in the saturation vapor pressure of ice and water when both are at the same temperature. Instead, many mixed phase clouds have a two-layered structure, with a liquid water layer directly adjacent to an ice layer. The simulation results in Figure 6.5b and c demonstrates that as long as both layers have the same temperature, the algorithm is relatively insensitive to the vertical organization of the particles. However, the algorithm does show some sensitivity to the size of the water droplets, as would be expected given the series of curves associated with the different size water droplets in Figure 6.4. If the effective radius of the water droplets is known or can be predicted (e.g., from climatology), the phase algorithm could be optimized to improve these results. However, the algorithm correctly classifies the majority of the clouds in these simulations.

6.3. Validation via case studies

The phase determination algorithm was applied to data collected by the AERI-ER at the SHEBA site from November 1997 to May 1998. The co-located DABUL (located within 100 m of the AERI) was used to evaluate the validity of the phase determination algorithm. Three case studies on April 26th, April 23rd, and April 21st are presented to demonstrate the algorithm's ability to ascertain cloud phase.

April 26th presents a relatively simple cloud scene over the *Des Grosilliers*, which was stationed at 76.00°N, 165.34°W. The winds were primarily westerly at the surface at about 3.5 m s^{-1}, and the surface temperature was approximately –20 C. An upper air high west of the ice camp helped to prevent thick cirrus clouds from moving over the site. Figure 6.7 shows the clear sky conditions during the beginning of the day gave way to a low, overcast cloud around midday; the cloud descended from approximately 800 m to 500 m by the end of the day. These clouds strongly scattered the laser radiation, yet have a small depolarization ratio (less than 10%) and thus are considered to be liquid water clouds. The clouds on this

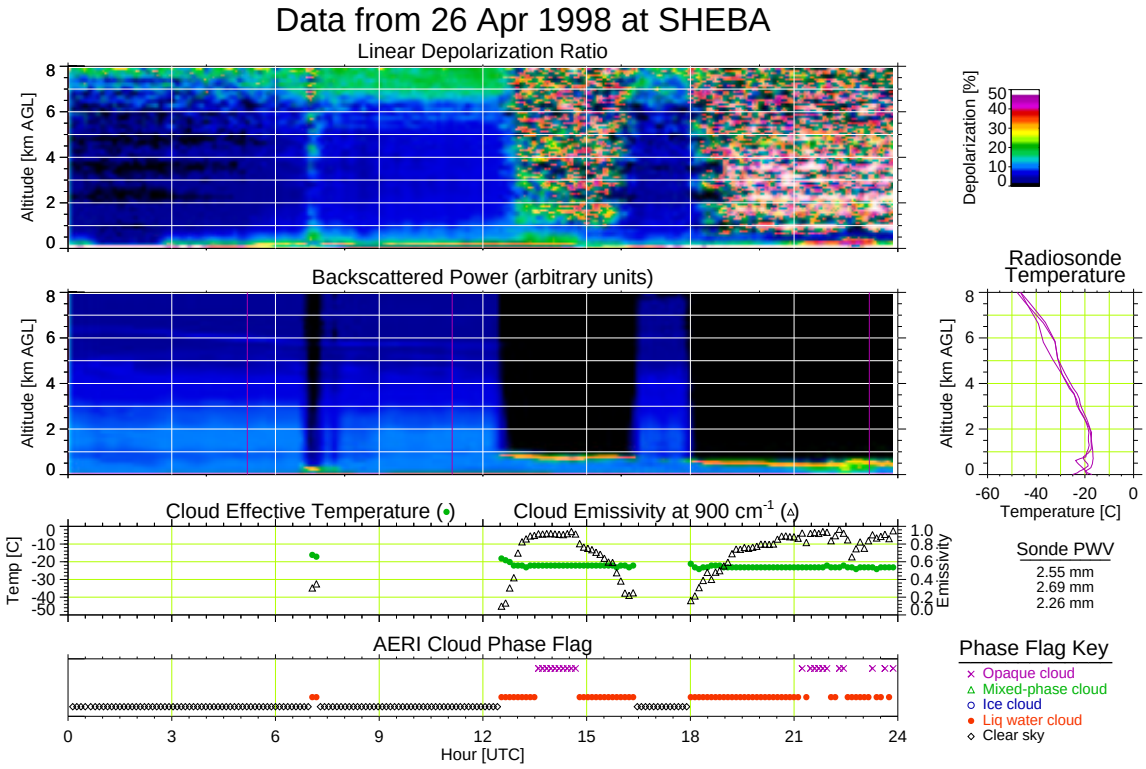

Figure 6.7: Time-height plot showing depolarization ratio and backscattered power observed by the DABUL on 26 April 1998. The purple vertical lines on the backscattered power figure indicate radiosonde launch times; the temperature profiles and observed PWV from these are shown on the right. The cloud temperature, retrieved using the MLEV technique, along with the cloud emissivity at 900 cm^{-1}, is also indicated. At the bottom of the image is the output of the 3-threshold AERI cloud phase determination algorithm, color-coded to indicate the phase of the clouds. See text for details.

day generally have an optically thickness greater than 3, the point at which the laser beam becomes fully attenuated by the cloud as indicated by the decrease in signal to noise above the cloud in the depolarization ratio. This cloud is correctly classified as a liquid-water only cloud by the AERI phase algorithm, except where the optical depth becomes larger than 5 and the algorithm indicates that the cloud is opaque. Note that the temperature of the cloud retrieved via the MLEV technique is about -21 C from 1300 – 1600 UTC, and about –23 C from 1800 – 2400 UTC, which agrees well with the temperature from the radiosonde profile at the cloud height (Figure 6.7). The temperatures from the MLEV technique are also very consistent about these values, even though the cloud emissivity varies greatly.

April 23rd shows a transition in the cloud scene over the SHEBA ship. A strong surface high started moving over the ice camp from the northwest heading towards the Beaufort Sea. The resulting winds were northerly at 5 to 7.5 $m\,s^{-1}$ and the temperatures remained fairly constant all day. The moving pressure center resulted in the clearing of the mid-level and low-level clouds by midday. The DABUL observations in Figure 6.8 show that a cloud system with relatively high depolarization values existing from the beginning of the day until about 1030 UTC, with a few relatively cloud free periods in between. These images indicate what appear to be precipitation bands of falling ice particles reaching the surface. The AERI was down for the first few hours of this day. After it returned to operation, the clouds in this period were classified as being ice-only clouds, and the one clear sky period from 0515 to 0645 UTC corresponds well with the break in the clouds observed by the DABUL. A second cloud was observed by both systems from 1500 – 1600 UTC. This cloud was classified as a liquid-water cloud by the AERI algorithm, which agrees well with the

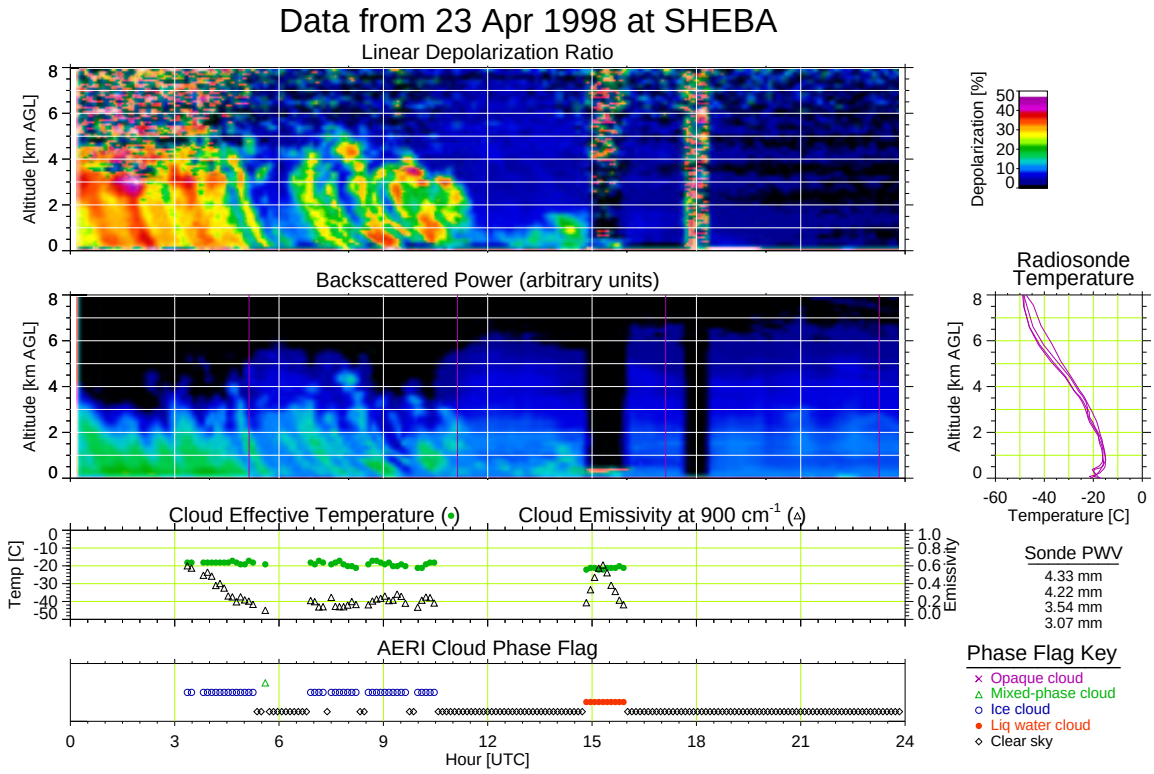

Figure 6.8: Same as Figure 6.7 for 23 April 1998.

diagnosis from the DABUL, as liquid water clouds have strong backscatter and low depolarization ratios.

On April 21st, the cloud scene was more complicated. A surface high was located in the eastern Beaufort Sea, a small surface low was just northeast of the ship, and a larger low pressure center was far south of the ship along the Asian coast of the Bering Sea. The winds were light and easterly at the surface, while upper level winds above the ship were from the southwest. Two cloud layers are apparent in the DABUL data (Figure 6.9). A thick (4-5 km) cloud layer with a base at roughly 2 km was present from about 0900 UTC to the end of the day, with a few breaks in the layer near the end of the day. This layer has a relatively high depolarization ratio, indicating that ice particles are present in this layer. The lower layer at 200 m from approximately 1500 to 2400 UTC (with some temporal gaps) has very low (<

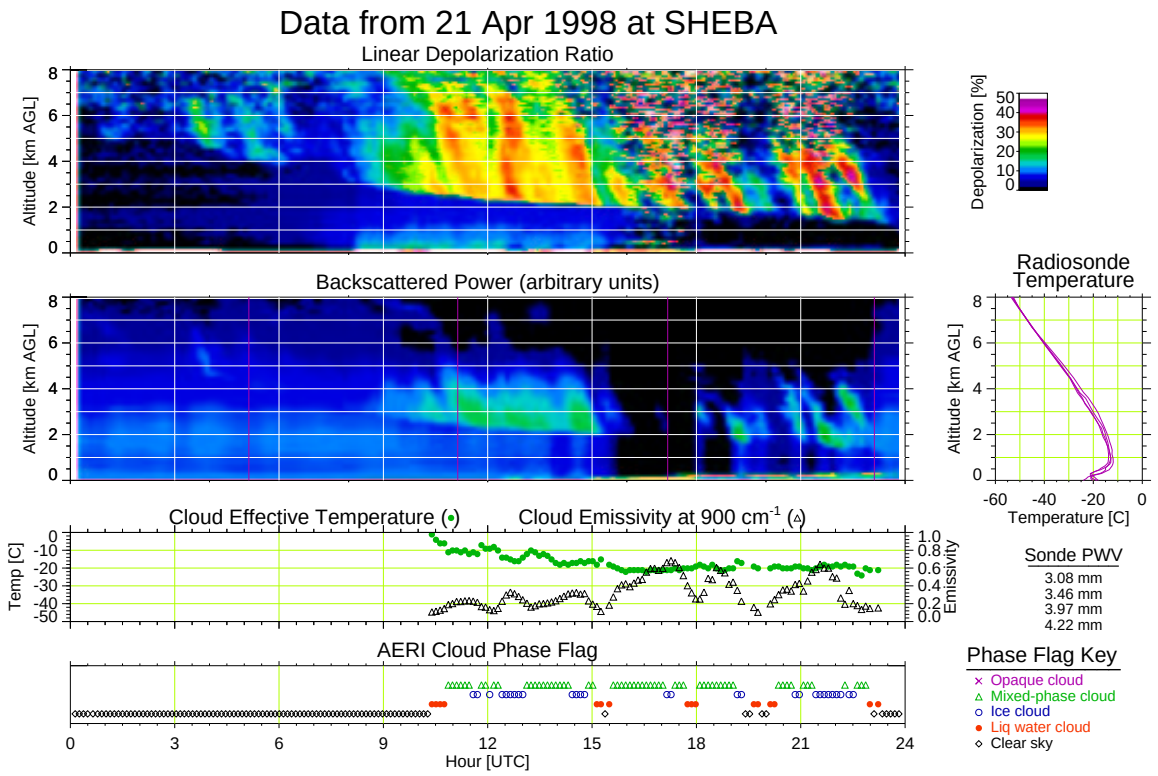

Figure 6.9: Same as Figure 6.7 for 21 April 1998.

10%) depolarization ratios and high backscattered power, which suggest that the scattering is due to liquid water particles. The AERI phase algorithm indicates that the upper layer is a mixed-phase cloud from 0900-1500 UTC, except for the regions of the most intense depolarization where the AERI algorithm indicated that the cloud was composed of only ice particles (such as between 1230-1300 and 1415-1500). When there are breaks in this upper layer above the lower level cloud (i.e., the lower level cloud is the only cloud layer in the vertical column), the phase algorithm indicates that the lower layer is liquid water, which agrees well with the DABUL observations. When both layers are present simultaneously, the algorithm classifies the scene as mixed phase, as the spectral signature of both ice and liquid water are present.

6.4. Results from SHEBA

While the case studies provide examples of how the phase algorithm works in particular situations, a more quantifiable evaluation is required before this algorithm is used to evaluate larger data records that do not have supplemental information on cloud phase such as data from the ARM NSA site. The DABUL and the AERI were both operational for most of the SHEBA experiment, and thus we can compare the cloud classification from these two systems to indicate when they agree and when they do not. The DABUL data, which were retrieved from the University Corporation for Atmospheric Research's (UCAR) Joint Office for Science Support (JOSS) archive, were filtered to merge any two cloud layers that were separated by less than 100 m into a single layer. To simplify the analysis between the DABUL and AERI techniques, coincident samples were analyzed only when both methods identified a cloud, the cloud was a single layer cloud, and the cloud was not opaque as determined by the AERI's algorithm. Approximately 630 hr of data met these requirements. While clouds that have depolarization values less than approximately 10% are most likely liquid water clouds, it is not possible to set a threshold to distinguish between ice-only clouds and mixed-phase clouds. Therefore, the results were broken into three categories: clouds that have mean depolarization less than 10%, mean depolarization values between 10% and 30%, and clouds that have a mean depolarization above 30%. In each category, the percentage of time when the AERI reported liquid water, mixed-phase, and ice clouds is given. These results are presented in Table 6.3. For the clouds that have mean depolarization values greater than 10%, the AERI phase algorithm reports mixed-phase or ice clouds approximately 80% of the time. For clouds that might be considered to be liquid water clouds via analysis from only

the DABUL's depolarization values, the AERI phase algorithm classifies the clouds as liquid water 50% of the time. These values indicate that the AERI phase algorithm has considerable skill in determining cloud phase for single layer clouds.

Table 6.3: Number of coincident samples in each category of mean depolarization value reported by the DABUL for single-layer, non-opaque clouds. F_water, F_mixed, and F_ice are the fractions of the time in each category that the AERI phase determination algorithm reported water, mixed-phase, or ice clouds, respectively.

DABUL Depol.	Number of samples	F_water	F_mixed	F_ice
< 10%	3286	51%	19%	26%
10% - 30%	1265	28%	27%	45%
> 30%	718	8%	21%	71%

The cloud phase statistics determined by the AERI were averaged to provide monthly statistics for the SHEBA experiment; these results are presented in Table 6.4. The results indicate that December, January, and February were considerably less cloudy than the other months. These statistics also indicate that the frequency of water, mixed-phase, and ice clouds is almost identical for the months from December through February, but that the percentage of opaque clouds, which is at a minimum in December, increases to 30% by February. Ice clouds are more prevalent in November and April, and liquid water clouds are more dominant in May.

Table 6.4: Monthly statistics on the number of hours, and the fraction reported as clear, liquid-phase, mixed-phase, ice-phase, or opaque by the AERI algorithm for 7 months during SHEBA..

Month	Hours	F_clear	F_water	F_mixed	F_ice	F_opaque
November	715.6	36%	12%	13%	22%	18%
December	722.0	76%	5%	4%	8%	8%
January	720.1	63%	8%	5%	5%	19%
February	440.9	50%	5%	3%	6%	30%
March	740.6	39%	12%	8%	9%	28%
April	709.8	32%	11%	10%	22%	26%
May	482.9	16%	32%	8%	14%	31%
TOTAL	4648.2	45%	11%	8%	14%	21%

A monthly breakdown of the DABUL data, which is consistent with Intrieri et al. (2002), is provided in Table 6.5, which provides an alternative mechanism for evaluating the AERI phase determination algorithm. Note that significantly fewer data were collected during February, as the lidar was offline for repair. These results show that the clear sky fraction is slightly overestimated by the AERI method as compared to the lidar. This overestimation is due to the cloud detection routine used by the AERI phase algorithm, which requires the cloud have an effective emissivity of at least 5% at 900 cm^{-1}. Therefore, this technique falsely classifies very thin clouds (typically higher cirrus clouds) as clear sky. Table 6.4 and Table 6.5 also suggest that the majority of the clouds classified as opaque by the AERI algorithm from March through May are liquid water clouds, as the sum of the opaque and liquid-water fractions is approximately the same as the fraction where the lidar's depolarization is less than 10%. These results demonstrate that the AERI-based algorithm described in this chapter has considerable skill in determining the cloud phase.

Table 6.5: Monthly statistics on the number of hours of data collected by the DABUL during SHEBA that were either reported clear or had a single cloud layer. The cases that had only a single cloud layer were then separated into bins with mean depolarization values of less than 10%, between 10% and 30%, and over 30%. Note that the lidar was offline for repair for a large part of February.

Month	Hours	Clear	Depol < 10%	10% < Depol < 30%	Depol > 30%
November	461.2	36%	19%	30%	15%
December	536.7	65%	6%	20%	9%
January	663.3	59%	19%	15%	8%
February	44.3	59%	41%	0%	0%
March	517.5	29%	46%	17%	8%
April	526.2	20%	51%	21%	8%
May	387.2	10%	76%	10%	4%
TOTAL	3136.4	39%	34%	18%	9%

Chapter 7

7. Physical Retrieval Algorithm

7.1. Theory

Chapter 6 has convincingly demonstrated that the AERI observations can be used to unambiguously determine the cloud phase for a wide range of Arctic clouds. Thus the first goal outlined in Chapter 2 has been met, and we are ready to move towards the second goal – the retrieval of cloud microphysical properties from the AERI observations.

For radiative transfer, the most important microphysical parameter is the cloud phase, but the water paths and the effective particle size of both the cloud liquid and ice are also required. If the effective size of the particle is large with respect to the wavelength and the particle is spherical, then a simple relationship exists between water path (*WP*), visible optical depth (τ_{vis}), and effective radius (r_e)

$$WP = \frac{2\tau_{vis} r_e \rho}{3} = \frac{2\tau_{IR} r_e \rho Q_{e,vis}}{3 Q_{e,IR}} \tag{7.1}$$

where ρ is the density of the substance (liquid or ice). Since we are working at an infrared wavelength, the particles are not typically much larger than the wavelength, but this is easily accounted for by multiplying by the ratio of the extinction efficiencies in the visible ($Q_{e,vis}$ = 2) and the extinction efficiency at the infrared wavelength ($Q_{e,IR}$). Note that the extinction efficiencies Q are integrated across the size distribution spectrum. Therefore, to retrieve liquid and ice water path, it is sufficient to retrieve the total optical depth, ice fraction, and the effective sizes of the two phases.

A second consideration in the design of this retrieval algorithm is the desire to propagate uncertainties in the observations into uncertainties in the retrieved parameters; i.e., to provide error bars on the retrieved values. By computing the uncertainty in the retrieved parameters, insight can be gained on the amount of information for each parameter in the radiance spectra. Many other groups demonstrate the uncertainty in their retrieved parameters via a small handful of case studies, but this technique is not robust and may not indicate the true uncertainty in any given retrieval.

Therefore, I set forth to retrieve the total cloud optical depth (τ), the fraction of the total optical depth that is ice (f_i), and the effective radii of the water and ice particles ($r_{e,w}$ and $r_{e,i}$, respectively) from the observed cloud emissivity spectrum. The retrieval technique uses optimal estimation following Rodgers (2000). If we let **X** be the 4x1 vector of the retrieved parameters (also called the state vector) and **Y** be the observed emissivity spectrum (Nx1 vector), then an iterative physical retrieval can be implemented as

$$\mathbf{X}^{n+1} = \mathbf{X}_a + \left\{\gamma \mathbf{S}_a^{-1} + \mathbf{K}_{\varepsilon X}^T \mathbf{S}_\varepsilon^{-1} \mathbf{K}_{\varepsilon X}\right\}^{-1} \left\{\mathbf{K}_{\varepsilon X}^T \mathbf{S}_\varepsilon^{-1} \left(\mathbf{Y} - F(\mathbf{X}^n)\right) + \mathbf{K}_{\varepsilon X} \left(\mathbf{X}^n - \mathbf{X}_a\right)\right\}, \quad (7.2)$$

where n is the iteration number and $\mathbf{S}_\varepsilon$ is the error covariance matrix of the observed cloud emissivity spectrum **Y**. The superscripts ^{T} and $^{-1}$ indicate matrix transpose and inverse, respectively. The forward model F is DISORT, where the gaseous optical depth profiles computed before the retrieval is run with the LBLRTM. The factor γ is a weighting factor and is typically set to 1. The *a priori* state vector $\mathbf{X_a}$ and its covariance $\mathbf{S_a}$ will be discussed later.

The Jacobian $\mathbf{K}_{\varepsilon X}$ is the sensitivity of the emissivity spectrum to the state vector. The Jacobian, which is a Nx4 matrix, is given by

$$\left(\mathbf{K}_{\varepsilon X}\right)_{ij} = \frac{\partial \boldsymbol{\varepsilon}_i}{\partial \mathbf{X}_j}. \tag{7.3}$$

Since radiative transfer in the infrared is nonlinear, the changes in the emissivity to changes in the state vector will also be nonlinear. Due to the nonlinearity of the problem, this Jacobian can not be precomputed, and thus finite differences are used to estimate this Jacobian for each iteration.

The benefit of equation (7.2) is that the 1-σ error estimates $\mathbf{e}_x$ for the state vector $\mathbf{X}$ can be found from

$$\mathbf{e}_X \mathbf{e}_X^T = \left\{\gamma \mathbf{S}_a^{-1} + \mathbf{K}_{\varepsilon X}^T \mathbf{S}_\varepsilon^{-1} \mathbf{K}_{\varepsilon X}\right\}^{-1}. \tag{7.4}$$

This matrix also indicates the covariance between the retrieved parameters.

Correct determination of the covariance matrix $\mathbf{S}_\varepsilon$ is critical for an accurate retrieval and estimation of the errors. The emissivity is seen to be a function of the observed and clear-sky radiance, effective cloud temperature, and the cloud-to-surface transmittance in equation (5.9). The uncertainty in the observed radiance observations is assumed to be wavelength independent (i.e., each channel has random uncorrelated noise). However, the uncertainty in the clear-sky radiance, which is primarily due to the uncertainty in the water vapor profile used in the calculation, is highly correlated with wavelength, as is the uncertainty in the cloud radiance. Therefore, care must be taken when these uncertainties are propagated into the emissivity uncertainty.

The basic observed variables that are needed to compute emissivity are the observed radiance spectrum **I**, the effective cloud temperature **T**, and the total precipitable water vapor

in the column **P**. Denoting the LBLDIS model by the operator *F*, the Planck function by the operator *B*, and the emissivity calculation by the operator *G*, we can write

$$\boldsymbol{\varepsilon} = G(\mathbf{I}, B(\mathbf{T}), F(\mathbf{P})). \tag{7.5}$$

Using the standard technique to propagate errors (Bevington and Robinson 1992), the error in ε is

$$\sigma_\varepsilon^2 = \left(\frac{\partial \varepsilon}{\partial I}\right)^2 \sigma_I^2 + \left[\left(\frac{\partial \varepsilon}{\partial B}\right)\left(\frac{\partial B}{\partial T}\right)\right]^2 \sigma_T^2 + \left[\left(\frac{\partial \varepsilon}{\partial F}\right)\left(\frac{\partial F}{\partial P}\right)\right]^2 \sigma_P^2, \tag{7.6}$$

or in matrix form, covariance matrix $\mathbf{S}_\varepsilon$ is

$$\mathbf{S}_\varepsilon = \mathbf{K}_{\varepsilon I}\mathbf{S}_I\mathbf{K}_{\varepsilon I}^T + \mathbf{K}_{\varepsilon B}\mathbf{K}_{BT}\mathbf{S}_T\mathbf{K}_{BT}^T\mathbf{K}_{\varepsilon B}^T + \mathbf{K}_{\varepsilon F}\mathbf{K}_{FP}\mathbf{S}_P\mathbf{K}_{FP}^T\mathbf{K}_{\varepsilon F}^T. \tag{7.7}$$

The matrix $\mathbf{K}_{\mathbf{ab}}$, which defines any arbitrary Jacobian in equation (7.7), is given by

$$\left(\mathbf{K}_{ab}\right)_{ij} = \frac{\partial \mathbf{a}_i}{\partial \mathbf{b}_j} \tag{7.8}$$

for any vectors **a** and **b**.

$\mathbf{S_I}$, $\mathbf{S_T}$, and $\mathbf{S_P}$ are error covariance matrices of the basic observed variables of downwelling radiance, cloud temperature, and PWV. $\mathbf{S_T}$ and $\mathbf{S_P}$ are 1x1 matrices. Since the error in the PWV is generally unknown, we will extrapolate the analysis of the SGP data to the Arctic and assume a 5% uncertainty in the PWV; i.e., $\mathbf{S_P}$ = 0.05 * PWV. Since we assume the errors in the observed radiance spectrum are wavelength-independent, $\mathbf{S_I}$ is a diagonal NxN matrix. The noise-equivalent radiance spectrum is computed for each sky dwell period and is stored in the AERI dataset, and these values are used to populate this error covariance matrix.

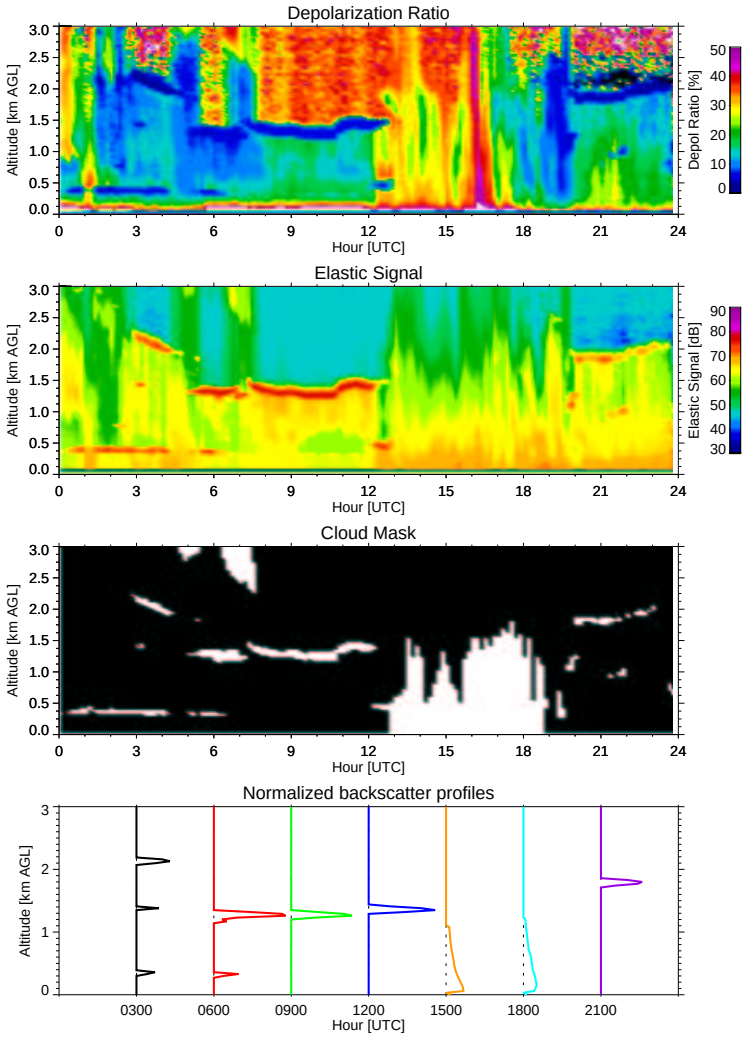

Figure 7.1: Depolarization ratio, backscatter, and cloud mask from the DABUL observations on 13 April 1998. Normalized backscatter profiles every 3 hours illustrate the weights that are used to compute the effective cloud temperature for the retrieval.

The uncertainty in cloud temperature is dependent on the method used to derive the effective cloud temperature. Given the potential bias of the MLEV derived cloud temperature (Chapter 5) and the presence of the collocated DABUL, the lidar's cloud boundaries was used together with a coincident radiosonde profile to estimate cloud temperature. Assuming that the aerosol extinction-to-backscatter ratio is constant with altitude, the uncalibrated lidar backscatter profile is divided by the square of the molecular density, yielding a quasi-extinction profile. This extinction profile is used to weight the cloud temperature in regions where the cloud mask indicates cloud exists in the vertical column, thereby yielding an estimate of the cloud temperature for all scenes (Figure 7.1). However, since Arctic clouds can often exist in multiple layers (Intrieri et al. 2002), the uncertainty in the cloud temperature was specified to be a function of the separation between the layers. For a single layer cloud or

for scenes where the maximum separation between cloud layers is less than 500 m, the uncertainty in the cloud temperature is set to 0.5 K; i.e., $\mathbf{S_T} = 0.5$. If the maximum separation is between 500 m and 2 km, then the cloud temperature uncertainty is set to 2.0 K. For cases where the maximum separation is between 2 and 6 km, the uncertainty is 5.0 K, whereas the uncertainty is set to 10 K if the maximum separation between cloud layers is more than 6 km.

Many of these Jacobians can be analyzed analytically, but there are a few that are more easily found numerically. For instance, $\mathbf{K_{\varepsilon B}}$ is a diagonal NxN matrix, since any change in the cloud radiance at wavelength *j* does not affect the emissivity at wavelength *i* (for $i \neq j$), and $\mathbf{K_{\varepsilon B}}$ is computed as

$$\left(\mathbf{K}_{\varepsilon B}\right)_{ii} = \frac{\partial \boldsymbol{\varepsilon}_i}{\partial \mathbf{B}_i} = \frac{-\left(\mathbf{I}_i - \mathbf{R}_i\right)}{\mathbf{J}_i \mathbf{B}_i^2}, \tag{7.9}$$

where **J** is the cloud-to-surface transmission. However, the Jacobians $\mathbf{K_{BT}}$ (a Nx1 matrix) or $\mathbf{K_{RP}}$ (a NxN matrix) are more easily found via perturbation of the Planck function and the LBLRTM, respectively. The Jacobians needed to compute $\mathbf{S}_\varepsilon$ are given in Appendix A.

7.2. Use of the a priori state vector

Equation (7.2) has built into it an *a priori*, or the best estimate of the state before the measurement is made. Often, the *a priori* $\mathbf{X_a}$ is developed from climatology, but since there is little data on the seasonal variation of cloud optical depth, ice fraction, or particle size, the *a priori* and its covariance matrix $\mathbf{S_a}$ are crudely estimated. The default particle sizes for water and ice are 7 and 21 μm, respectively, as suggested by the CPI observations given in Figure 6.6, but the associated uncertainties in these values are set to be 10 and 20 μm, respectively,

as to not be a real constraint. The total cloud optical depth can be approximated as a simple polynomial function of the cloud emissivity at 900 cm^{-1}, and the initial guess of the ice fraction is taken to be 50%. These values provide estimates for the optical depths for the water and ice components in $\mathbf{X_a}$. The associated uncertainties in optical depth are set to 5, which is large enough as to not be a serious constraint on these retrievals. The off diagonal elements in $\mathbf{S_a}$ are assumed to be zero.

The advantage of using the *a priori* in this formulation is that additional knowledge can easily be added to the retrievals. For example, if the cloud temperature is above 0 C, then it is highly unlikely that the cloud will contain any significant amount of ice, and therefore the *a priori* can be used to "turn off" the ice component of the retrieval. By setting the optical depth due to ice in $\mathbf{X_a}$ to zero and its associated variance in $\mathbf{S_a}$ to a value very near zero (such at 1e-10), the retrieval is effectively a single-phase retrieval and is only able to retrieve the optical depth and particle size of the water component. Likewise, if the cloud is colder than -40 C, then the retrieval automatically converts to an ice-only retrieval.

7.3. Implementation

The equations in section 7.1 provide the framework for the physical retrieval. The retrieval algorithm was implemented in Fortran (DISORT) and C (everything else). A flow-chart diagram is given in Figure 7.2. The code is controlled by an ascii parameter file, which indicates where the input AERI and lidar data are located. The location of the monochromatic optical depths, which were computed via the LBLRTM a priori, is also listed in this file. This file also contains system constants, such as the maximum number of iterations to allow and

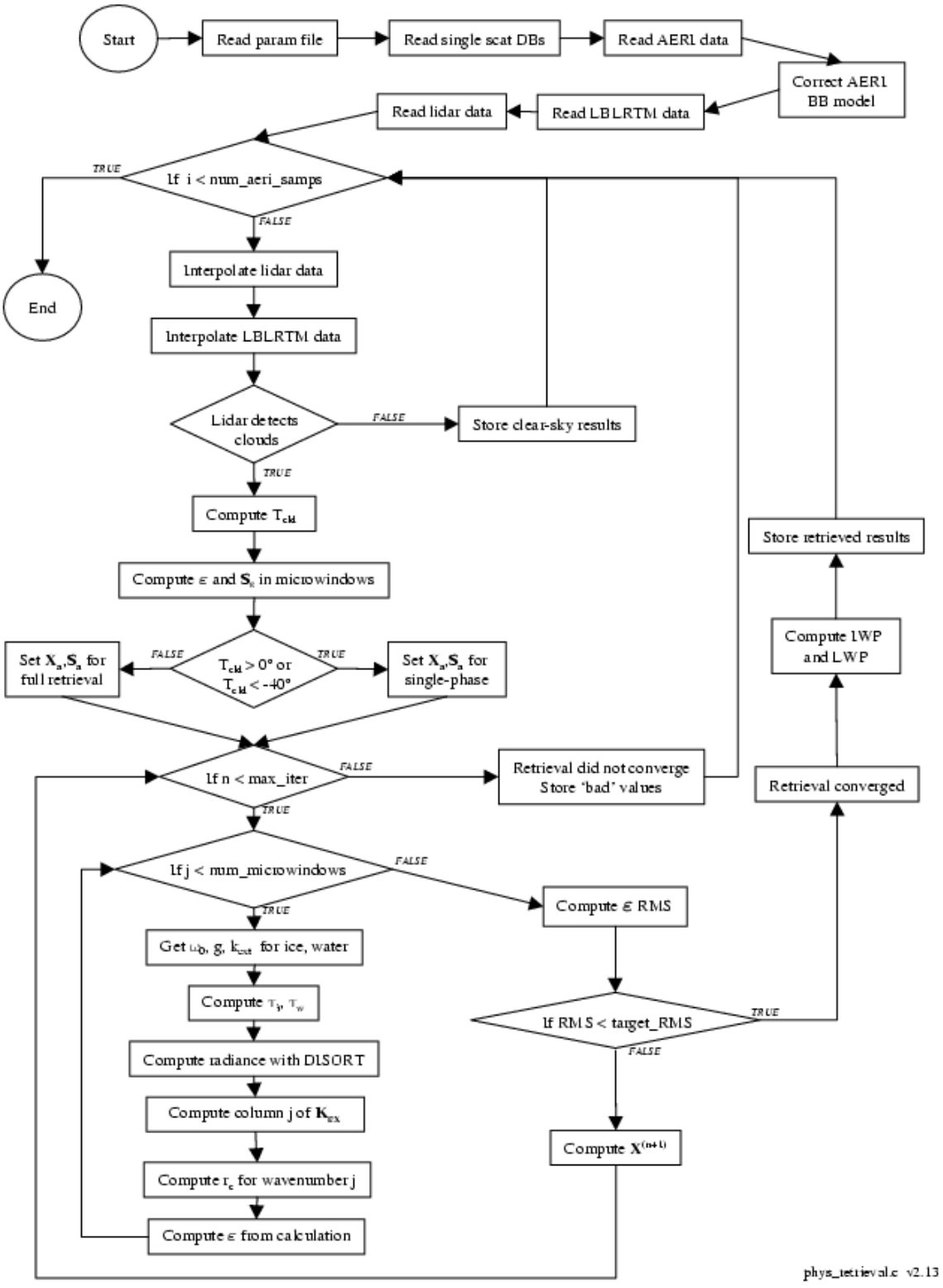

Figure 7.2: Flow chart for the physical retrieval algorithm.

the target root-mean-square (RMS) difference (in brightness temperature) that needs to be reached to consider the retrieval as "converged." Finally, the initial *a priori* values for $\mathbf{X_a}$ and $\mathbf{S_a}$ are set in this file. Therefore, the user can specify if the retrieval is to be a "full" or a single-phase (ice or water only) retrieval, or can easily update the *a priori* values as more information on the basic climatology becomes known over time.

Before the retrieval algorithm is run, the gaseous optical depth profiles must be calculated with the LBLRTM. For each sounding launched on the day of interest (as well as the days just before and after), the LBLRTM is run twice: once for the nominal sounding and once where the PWV has been arbitrarily increased by 5%. This is required since the Jacobian $\mathbf{K_{FP}}$ in Eq (7.7) is computed via perturbation. Note that $\mathbf{K_{FP}}$ is reasonably unsensitive to the size of the PWV perturbation as the low amounts of water vapor in the Arctic result in almost negligible contribution by self-broadened water vapor continuum absorption. The dominant source of absorption in the microwindows used in this study is from the foreign-broadened water vapor continuum, which is proportional to the water vapor density and hence approximately linear.

The single scattering property databases, which are read directly after the parameter file, are also created before the retrieval is run. They contain the extinction coefficient, asymmetry parameter, single scatter albedo, and the scattering, absorption, and extinction efficiencies integrated over different size distributions at periodic wavelength intervals across the infrared spectrum. For each wavelength, a set of size distributions using the same functional form (i.e., lognormal, gamma, etc.) was generated with increasing effective radius. Water droplets are modeled as a collection of spheres using Mie theory (Wiscombe 1980). The ice crystals were modeled as both spheres (again using Mie theory), hexagonal columns

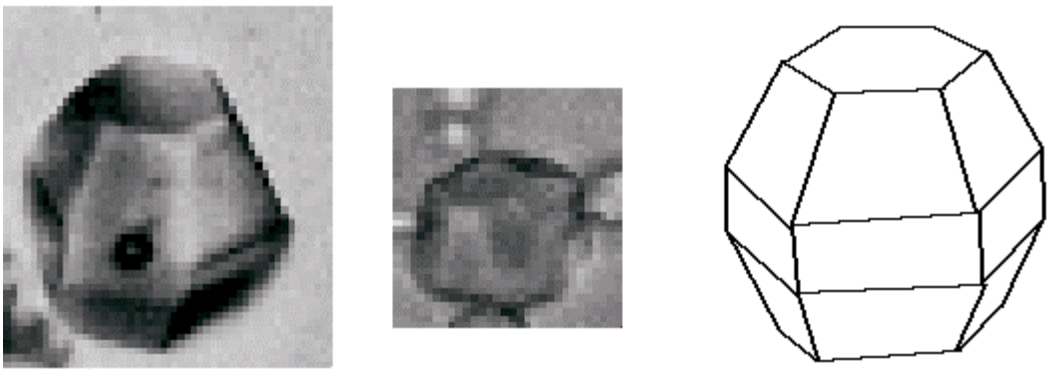

Figure 7.3: Example images and a schematic drawing of a droxtal. From Yang et al. 2003b.

(Yang et al. 2001), or droxtals (Figure 7.3, Yang et al. 2003b, Ohtake 1970) for crystals smaller than 16 μm and hexagonal columns for larger crystals. The user selects the habit for the ice particles the retrieval should use via the ascii parameter file. Warren (1984) and Downing and Williams (1975) provided the indices of refraction for ice and water, respectively. Note that gamma size distributions were utilized for this thesis, due to the good fit to the CPI observations (Figure 6.6) and the relative insensitivity to the shape of the size distribution (Figure 5.6). However, the manner in which these scattering databases where implemented allows an unlimited number of different databases, each one incorporating different size distributions and/or habits, to be utilized in this algorithm.

Using equation (7.1) the liquid and ice water paths can be computed, if the particles are spheres. However, ice particles are typically not spheres, and thus to make the code robust and able to compute the ice water path for any crystal habit, the volume for each size distribution (which is normalized to have $N = 1$) and effective radius is also stored in the scattering databases. The ice water path (IWP) can then be derived from the following relation

$$IWP = N(r_e, \tau, z) V_0(r_e) \rho_i z \qquad (7.10)$$

where r_e and τ are from the retrieval, ρ_i is the density of the ice, N is the number density of the particles in the cloud, V_0 is the volume of the size distribution for the retrieved effective radius (which is obtained from the scattering database), and z is the thickness of the cloud as measured by the lidar. The "volume-based" IWP derived using equation (7.10) is identical to the IWP derived using equation (7.1), the "spherical" algorithm, for ice spheres. However, there are slight differences in the uncertainties of the IWP derived from the two methods, primarily because of the added uncertainty in V_0. Figure 7.4 demonstrates the uncertainty in IWP for the two IWP formulations as a function of the uncertainty in r_e assuming no error in τ. In general, the uncertainty in IWP is about 5% larger for a given uncertainty in r_e using the volume-based algorithm opposed to the spherical equation. Note that a 5% uncertainty in τ translates into a 5% uncertainty in IWP for both of the IWP algorithms.

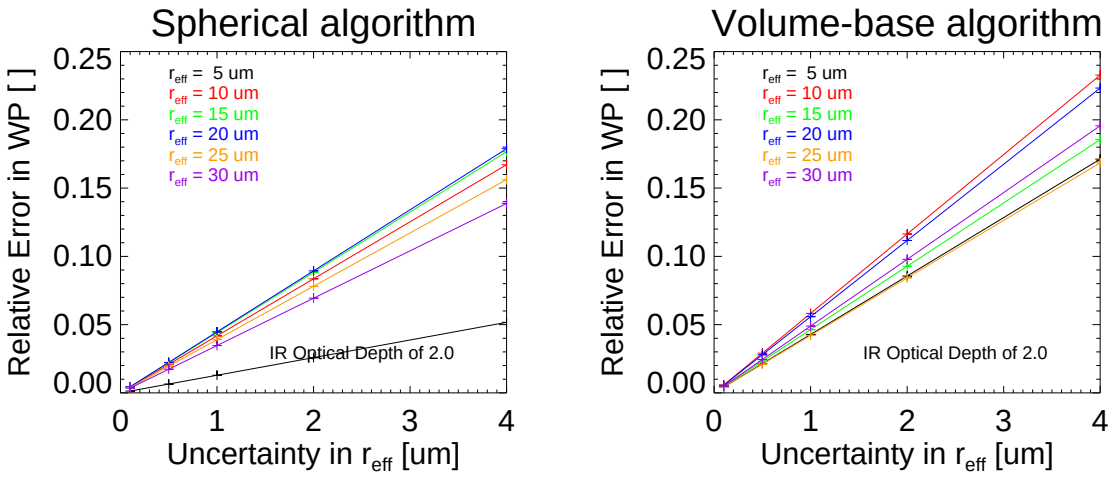

Figure 7.4: Relative error in the derived water path as a function of the uncertainty in the effective radius of a distribution of spherical particles. The two techniques, described in the text, give very similar results for spheres.

After reading the parameter file, the algorithm proceeds to read in the data for the particular day, including the AERI, lidar, and LBLRTM data. The AERI data files include an estimate of the noise level in the radiance observations, and these values are used in the computation of $\mathbf{S}_\mathbf{I}$ in Eq (7.7). It should be noted that the atmospheric state data (temperature, pressure, and water vapor profiles) are read in directly from the LBLRTM output, so that the same profiles used to compute the gaseous absorption are used in the retrieval algorithm.

At this point, the initialization of the algorithm is complete, and we loop over the AERI observations. For the current AERI observation, the closest lidar sample is selected that is within 20 minutes; if the closest lidar sample is outside the 20-min window from the AERI observation then no retrieval is performed. The lidar data are then used to compute the quasi-extinction weighted cloud temperature, as specified earlier in this chapter. If the cloud mask specifies no cloud for this sample, then the scene is flagged as clear and the algorithm moves to the next AERI sample.

The monochromatic optical depth data computed by the LBLRTM are then linearly interpolated (at each level) to the AERI sample time. Interpolating the gaseous optical depths in this manner essentially is the same as assuming that the airmass, and in particular the PWV, varies linearly between radiosonde launch times.

If a cloud was detected, then the emissivity spectrum and its covariance matrix $\mathbf{S}_\varepsilon$ are computed. At this stage, the cloud reflectivity is assumed to be zero to ease the computation of $\mathbf{S}_\varepsilon$. This assumption introduces little error in the computation of $\mathbf{S}_\varepsilon$, since the reflectivity is generally less than a few percent. Note that $\mathbf{S}_\varepsilon$ is constant for this AERI sample; therefore, the inverse of $\mathbf{S}_\varepsilon$ is only computed once per AERI observation. The number and location of the microwindows used in the retrieval is somewhat arbitrary (i.e., similar results can be obtained

with different sets of microwindows), as long as channels are chosen in all three 'primary' spectral regions (8-10 μm, 10-13 μm, and 17-25 μm). The set of microwindows channels used for the physical retrievals performed for this thesis is given in Table 7.1. However, since the location and number of microwindows can be modified easily, the 3-channel phase threshold algorithm outlined in Chapter 6, which was defined for a distinct set of microwindows, is not utilized to get a first guess for f_i in the physical retrieval. Instead, f_i is assumed to be 0.50. The initial values for the effective radii or the ice and water particles are taken from the *a priori*. The first-guess for the 900 cm^{-1} (11 μm) total optical depth is derived from a simple lookup table that related ε to τ, where the lookup table was developed from simulations in Chapter 8.

Table 7.1: Center wavelength and wavenumber ranges for each microwindow used in the physical retrieval.

Center wavelength [μm]	Wavenumber range [cm^{-1}]	Center wavelength [μm]	Wavenumber range [cm^{-1}]
20.90	477.5-479.5	11.19	891.9-895.8
20.13	495.5-498.0	11.09	898.2-905.4
18.84	529.9-531.5	10.70	929.6-939.7
17.85	558.5-562.0	10.39	959.9-964.3
12.94	770.9-774.8	10.09	985.0-998.0
12.69	785.9-790.7	9.25	1076.6-1084.8
12.33	809.0-812.9	9.13	1092.1-1098.8
12.20	815.3-824.4	8.97	1113.3-1116.6
12.03	828.3-834.6	8.86	1124.4-1132.6
11.83	842.8-848.1	8.73	1142.2-1148.0
11.60	860.1-864.0	8.63	1155.2-1163.4
11.43	872.2-877.5		

The algorithm uses this first guess as the starting point for the physical retrieval. For the given particle sizes, the single scattering properties of the ice and water particles at each

wavelength are interpolated from the single scattering property databases, and these are used to compute the optical depth for each phase at the given wavelength from the reference (900 cm^{-1}) wavelength. These scattering properties, along with the gaseous optical depth profiles computed using the LBLRTM, are input into DISORT and the radiance is computed. Given the current estimate of the state vector **X**, the surface temperature is perturbed by 10 K and the downwelling radiance recomputed with DISORT. From these two downwelling radiance values, the cloud reflectivity at this wavenumber is computed using equation (5.10). DISORT is then called 4 additional times, where each time one of the elements in the state vector is perturbed by 5%. It should be noted that since the extinction coefficient k_e is a function of particle size, the extinction coefficient used when computing $\partial\varepsilon/\partial r$ must be scaled by the ratio of the extinction coefficient at the reference wavelength λ_0 at the nominal particle size r and the perturbed particle size $\hat{r}$:

$$k_e = k_e(\hat{r},\lambda)\frac{k_e(r,\lambda_0)}{k_e(\hat{r},\lambda_0)}. \qquad (7.11)$$

This maintains a constant optical depth at the reference wavelength (900 cm^{-1}) which is essential for the proper computation of the Jacobian.

After looping over all of the microwindows, the cloud emissivity $\mathbf{Y_{calc}}=F(\mathbf{X}^n)$ can now be computed, including the cloud reflectance spectrum. Using the Jacobian $\mathbf{K_{\varepsilon x}}$, which was computed row-by-row for each microwindow, the updated value of **X** can be computed from equation (7.2). The calculated emissivity spectrum is compared to the observed emissivity spectrum to compute the root-mean-square (RMS) difference. The RMS value will be used to test for convergence of the algorithm. If the RMS is less than the target RMS, then the

algorithm is deemed to have converged and the retrieved cloud properties and their uncertainty estimates are stored. Otherwise another iteration is performed, wherein the updated version of the state vector **X** is used as the first guess. Each parameter in the new state vector is checked to ensure that it is in a valid range; i.e, the optical depths of ice and water must be greater than zero, and the effective radii of the water and ice particles must lie in the range 2-25 μm and 5-95 μm, respectively. This continues until either the algorithm converges or the maximum number of iterations is reached. If the latter condition occurs, "bad" values are stored in the output file to indicate that the algorithm detected cloud but that it was unable to converge. This procedure continues until all of the AERI samples have been processed.

In practice, it has it has been difficult to determine a RMS threshold that works well for all cases. It seems that the RMS value is dependent on the phase of the cloud, and thus the threshold is somewhat scene dependent. As a work-around, the code can also be specified to perform a set number of iterations (typically 10), and the $\mathbf{X}^i$ (for iteration i) that yielded the lowest RMS difference between the observed and calculated emissivity spectrum is used as the solution. This approach is more expensive computationally, but it mitigates the scene dependence of the convergence threshold.

As indicated in Chapter 3, interferograms are usually co-added for several minutes to improve the signal-to-noise ratio in the AERI observations. If the cloud conditions are rapidly changing during the instrument's sky dwell period, then there should be additional uncertainty in the retrieved microphysical cloud properties, as compared to case where the cloud conditions are unchanging during the sky dwell period. However, it is inappropriate to assume that the uncertainty is uncorrelated across the spectrum and use the sky variability

spectrum to populate only the diagonal entries of the associated covariance matrix. However, at this time, the proper formulation of the covariance matrix that captures the scene variability has remained elusive, and instead the sky variability value at 900 cm^{-1} is stored in the netCDF output file for each sample. Post-processing analysis will then apply a threshold to this sky variability field to eliminate cases where the scene is changing during the sky dwell period.

In addition to the retrieved parameters (τ_i, τ_w, $r_{e,i}$ $r_{e,w}$, LWP, and IWP) and their uncertainties and the sky variability field, many other variables are written into the output netCDF file to assist in the analysis of these results. These variables include both the MLEV-derived and lidar-weighted cloud temperatures, the PWV for the scene, the number of iterations the algorithm required for convergence, the observed emissivity spectrum, and the state of the AERI's hatch. The three components of the error in the emissivity spectrum are also captured in the output netCDF file. These three components are easily identified in equation (7.7) as the uncertainty in the AERI observations, cloud temperature, and PWV amount, respectively. These variables are analyzed to identify strengths and weaknesses of the physical retrieval algorithm (Chapter 8) and can be used to investigate the algorithm's performance for any particular retrieval. In addition, the state vector and the cloud emissivity spectrum calculated from it are also stored for each iteration, allowing the progression of the algorithm to be investigated for any sample. Finally, the cloud reflectance spectrum is also output.

Chapter 8

8. Retrieval algorithm validation

8.1. Validation approaches

There are two complementary ways to validate any retrieval algorithm. The first is to compare retrieved results from real data with either in situ observations or against other retrievals of similar variables. Validation using this approach is limited by the actual conditions encountered during the focus period studied, and therefore the results may not be representative of all the conditions that the retrieval algorithm may encounter in routine operations. This approach also suffers from lack of knowing exactly what is "truth," as both in situ observations and data from other retrieval algorithms have their uncertainties, biases, and general limitations.

The second way is to use simulated data to test the algorithm. In this manner, the extremes of the possible input space are more easily tested than with direct observations. Additionally, since the input data was simulated, the true properties of the atmosphere and clouds are known exactly. This approach does not lend itself easily into discovering possible biases in the retrieval algorithm, as the forward model used in the retrieval algorithm is typically the same forward model used to create the simulated input data. Therefore, the two methods of validation, both simulations and comparisons to real data, must be used to fully characterize any retrieval algorithm.

There are many questions that are most easily answered using simulations. For example, what is the sensitivity of the physical retrieval algorithm outlined in Chapter 7 to the

cloud optical depth τ, the ice fraction f_i, and the particle sizes $r_{e,w}$ and $r_{e,i}$? What are the limits of the retrieval; e.g., what is the maximum optical depth that can be retrieved? Can the phase of the cloud really be ascertained with any certainty? What is the dominant error in the observed cloud emissivity? These, and other similar questions, are addressed using simulations.

8.2. Validation with simulations

8.2.1. GENERAL RESULTS

The LBLDIS model was used to simulate over 100 different Arctic clouds. The primary atmosphere used in these simulations was specified by a SHEBA radiosonde on 25 April 1998 that had a PWV of 2.45 mm, but other Arctic atmospheres were also utilized with very similar results. Only single-layer clouds were simulated. The clouds were primarily placed at 600 m, which corresponds roughly to the peak of the cloud height distribution as suggested by Intrieri et al. (2002). The retrieval algorithm showed very little sensitivity with height; i.e., if the same cloud placed at different altitudes, the retrieved microphysical properties were nearly identical as long as the specified cloud temperature was correct for each case.

The simple threshold-based cloud phase determination algorithm (Chapter 6) was limited to optical depths less than approximately 5. Therefore, one question is whether or not this is the limit for the full physical retrieval, since it is using many more microwindows. Figure 8.1 shows multiple brightness temperature spectra calculated using LBLDIS for both water and ice clouds for a range of optical depths. Note that there is less than 3 K difference

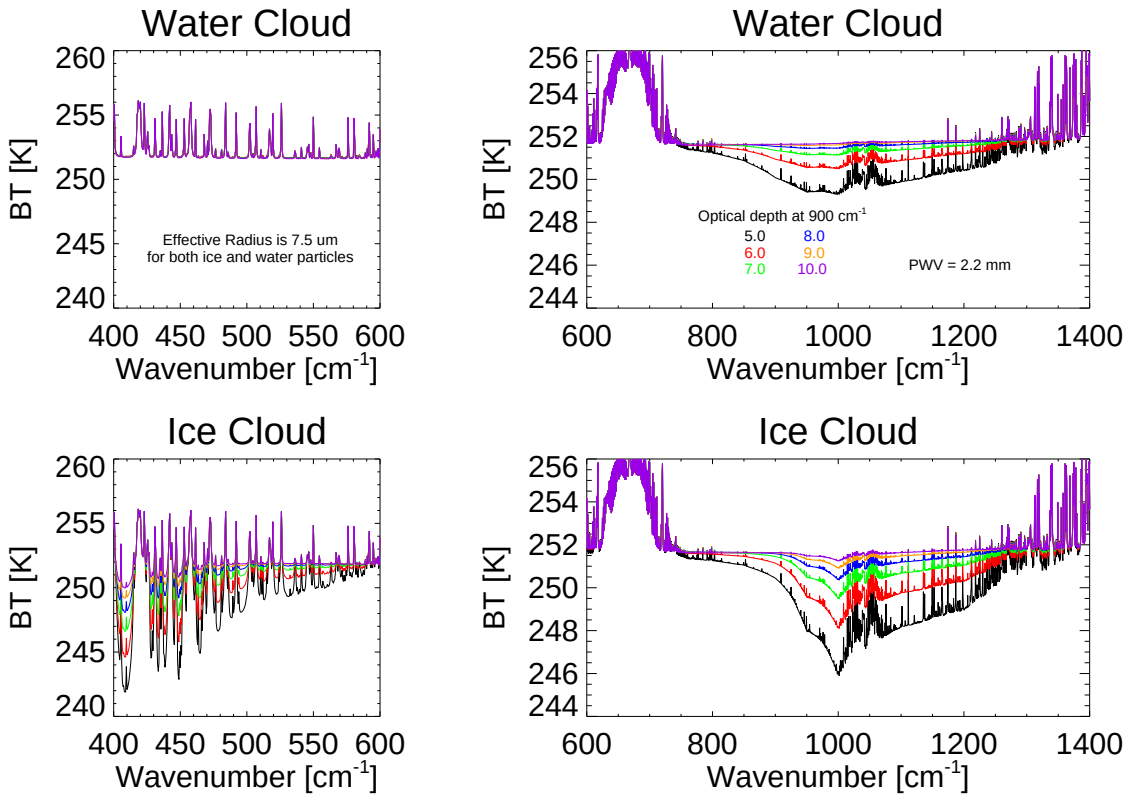

Figure 8.1: Brightness temperature spectra for optically thick water (top) and ice (bottom) clouds.

between the spectra at 950 cm^{-1} for the water clouds with $\tau = 5$ and $\tau = 10$. This suggests that $\tau = 5$ is certainly near the limit of the retrieval algorithm for liquid water clouds, and in fact the uncertainty in the retrievals of optical depth for liquid water starts to increase dramatically as τ becomes larger than 3 due to the decreased sensitivity in the Jacobian $\mathbf{K}_{ex}$. However, there is better sensitivity to the optical depth of the ice particles at these larger optical depths (Figure 8.1), especially in the 400-600 cm^{-1} region where the absorption due to ice is smaller. This translates into somewhat smaller uncertainties in the retrieved optical depth for ice clouds when $\tau > 3$ as compared to liquid water clouds.

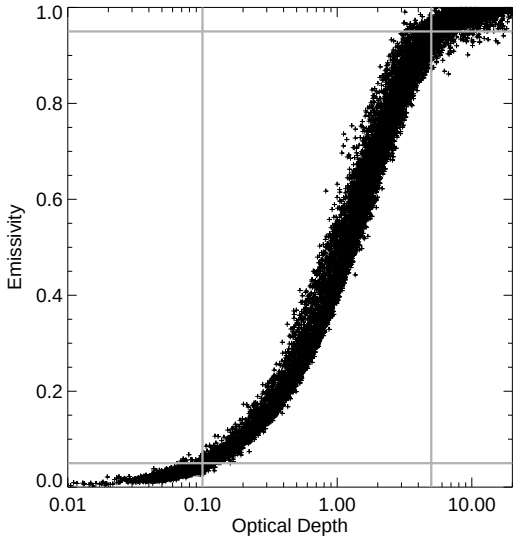

Figure 8.2: Relationship between cloud emissivity and cloud optical depth for clouds at SHEBA.

Real data can be used to gauge the range of optical depths over which the algorithm is truly sensitive. Figure 8.2 shows a scatter plot of retrieved optical depths at 900 cm^{-1}, which is near the minimum shown in Figure 8.1, versus the cloud emissivity at the same wavelength. If we restrict our analysis to data where the cloud emissivity is between 0.05 and 0.95, the analysis is limited to clouds whose optical depths range from about 0.1 to approximately 5. It should be noted that the spread in this data is primarily due to differences in the phase of the clouds that make up this data set, with liquid water clouds having higher emissivity for lower optical depths, as suggested by Figure 8.1.

Simulations were used to determine the dominant source of error in the observed cloud emissivity spectrum. An example of the three components that contribute to this uncertainty for a mixed-phase cloud with $\tau = 1$ is shown in Figure 8.3. [Note that the emissivity error plotted in this figure is relative; i.e., $\sigma_\varepsilon / \varepsilon$.] The assumed 5% uncertainty in PWV dominates the uncertainty in ε for the longer wavelengths (wavenumbers less than 750 cm^{-1}) for all values of τ. For clouds with an optical depth of approximately 0.5, the contribution of the instrument noise in the AERI-ER (not to be confused with the sky variability measured by the AERI) and a 0.5 K uncertainty in cloud temperature is roughly equivalent. The uncertainty in

the AERI observations becomes the dominant term for channels above 750 cm^{-1} when τ < 0.5, whereas the uncertainty in cloud temperature is the dominant term above 750 cm^{-1} when the τ > 0.5. When the uncertainty in the cloud temperature becomes larger than 2 K (see Chapter 7), this term is the dominant term in the uncertainty of the emissivity across the spectrum. Therefore, the real observations (Chapter 9) are screened before analysis to only use observations where the temperature uncertainty is less than or equal to 2 K.

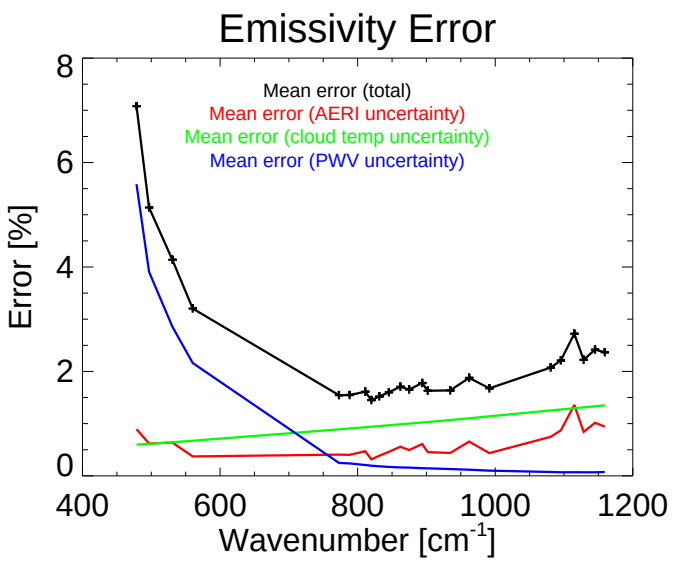

Figure 8.3: Typical emissivity error spectrum, broken into its three components, for a cloud with an optical depth of 1. The error is the relative error; i.e., $\sigma_\varepsilon / \varepsilon$.

8.2.2. Evaluation of biases in the observations

The uncertainty in the cloud temperature is relatively flat across the spectrum, and correspondingly, small biases in the cloud temperature used in computing the emissivity translate into relatively flat biases in the computed emissivity. Therefore, small positive (negative) biases in the cloud temperature result in negative (positive) biases in the total optical depth. This is demonstrated in the MLEV example in Figure 5.5. Small biases in the cloud temperature do not affect the spectral signature of the cloud emissivity, and thus the

retrieved ice fraction and particle sizes are essentially unaffected by small biases in cloud temperature.

Water vapor absorption is a strong function of wavelength, with the absorption being much stronger in the 400-600 cm^{-1} region than in the 800-1200 cm^{-1} region. This is illustrated in Figure 8.3, where a 5% uncertainty in PWV dominates at the longer wavelengths. The typical range of PWV in the Arctic is from 1-15 mm, and over this interval the microwindows in the 400-600 cm^{-1} spectral region go from fairly transparent to almost opaque. Since this spectral region is critical for the correct determination of cloud phase, the ice fraction is very sensitive to biases in PWV. Uncertainties in the water vapor continuum model when this research began prevented the simultaneous retrieval of PWV and cloud properties from the AERI spectrum. The release of the new MT-CKD model (Chapter 4) reduces the uncertainty in the water vapor continuum, and thus future work will incorporate the simultaneous retrieval of PWV with the cloud properties.

Simulations were also conducted to evaluate the impact on the retrieved cloud properties for the small 1 RU bias that may exist in the AERI observations (Chapter 4). These simulations suggested that a bias of this size only affects the retrievals if the cloud optical depth is less than 0.2, wherein the bias is approximately 25%-50% of the signal (this is also suggested by Figure 4.9). At these small optical depths, there is little information on particle size and ice fraction (as will be discussed later). As τ becomes larger, a small 1 RU bias in the AERI observations becomes negligible.

8.2.3. EVALUATION OF THE SKILL OF THE PHYSICAL RETRIEVAL

To evaluate the skill of the physical retrieval for different cloud conditions, each of the simulated clouds was replicated and instrument noise was added. The instrument noise was assumed to be Gaussian with the standard deviation provided by the AERI's noise spectrum (Figure 3.5), and the error was assumed to be uncorrelated across the spectrum. Typically 60 individual spectra were created for each simulated cloud. The physical retrieval was then used to derive the cloud properties from these spectra. An example showing the retrieved parameters for 5 different mixed phase clouds, along with the true values of these parameters, is shown in Figure 8.4. In this example, the effective radius of the water and ice particles is fixed at 7.5

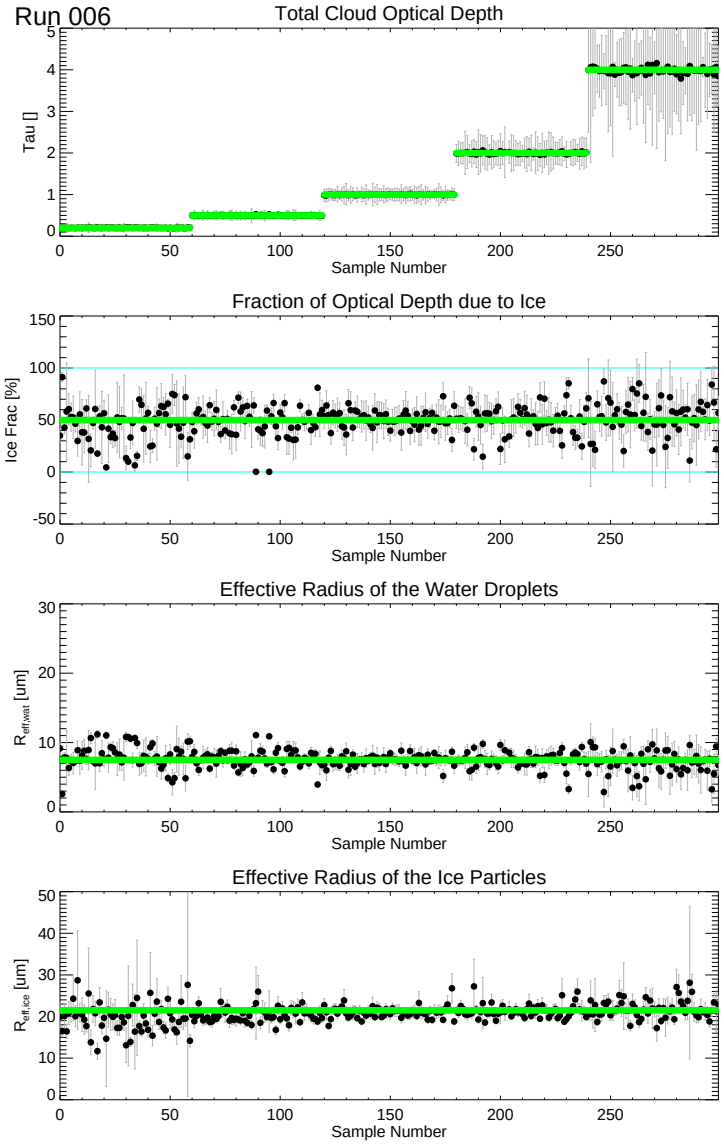

Figure 8.4: Results from the physical retrieval for 5 mixed-phase clouds with different optical depths. There are 60 samples for each cloud. Gray lines represent the "truth."

and 21.5 μm, respectively, and the ice fraction is 0.5 for all 5 cases. The true optical depth, however, approximately doubles for each cloud, going from 0.2 (near the lower limit from Figure 8.2) to 4 (near the upper limit). The error bars shown are 1-σ uncertainties that were propagated by the physical retrieval. The uncertainty in the optical depth grows substantially, in both a relative and absolute sense, for $\tau = 4$. Similarly, there is also more scatter and larger 1-σ error bars in the retrieved f_i, $r_{e,w}$ and $r_{e,i}$ values when the optical depth is 4 or larger. When the optical depth is small (τ = 0.2), there is quite a bit of scatter in the retrieved parameters for f_i, $r_{e,w}$ and $r_{e,i}$ and the associated 1-σ error bars are larger than for clouds where the optical depth is intermediate ($0.5 \leq \tau \leq 2.0$). This indicates that the information content in the spectra for the retrieval of f_i, $r_{e,w}$ and $r_{e,i}$ becomes smaller as the optical depth gets small or large, or equivalently as the cloud emissivity approaches 0 or 1.

To analyze the data more quantitatively, histograms of the retrieved τ, f_i, $r_{e,w}$, and $r_{e,i}$ were created for each simulated cloud. The mean and standard deviation of the retrieved parameters, as well as the mean of the 1-σ error estimates, were computed. An example of these histograms for the third cloud case shown in Figure 8.4 is provided in Figure 8.5. Comparing the mean retrieved value against the true value identifies any biases that may be induced by the physical retrieval. In Figure 8.5, the mean retrieved value is almost identical to the true value for each parameter with the exception of $r_{e,i}$ where the mean value is biased slightly lower than truth; however, this is well within the uncertainty dictated by the standard deviation of the retrieved values. Note also that the magnitude of the mean 1-σ error bar is

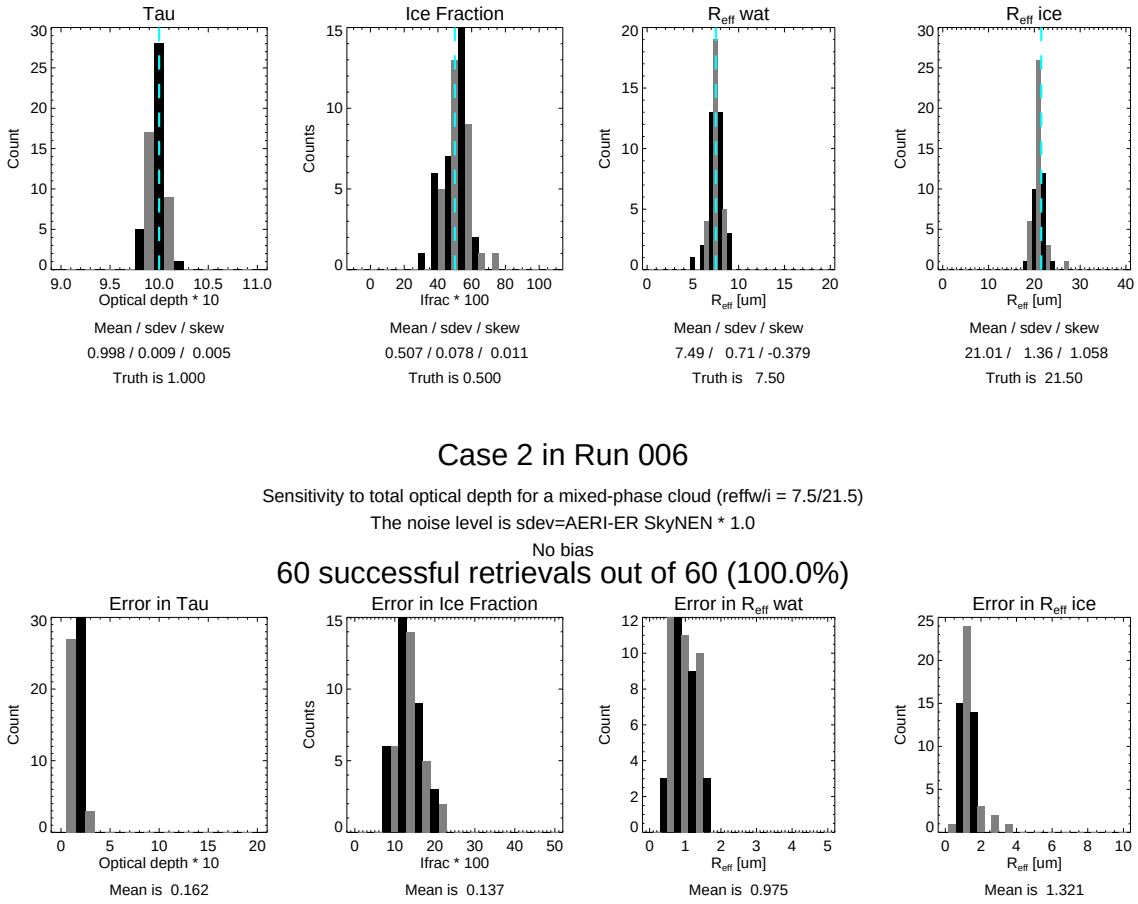

Figure 8.5: Distribution of retrieved values (histograms) versus the true values (dashed lines) for optical depth, ice fraction, and water and ice particle size (upper panels), as well as the 1-σ errors, for the mixed-phase cloud with optical depth of 1 in Figure 8.4.

very similar to the standard deviation of the retrieved parameters, indicating that the uncertainty estimates derived using the optimal estimation approach are reasonable.

This approach was used to test the algorithm's sensitivity to different cloud optical depths, ice fractions, and sizes of the water and ice particles. The true values of the cloud parameters for each ensemble are provided in Appendix B. Appendix C provides the mean and standard deviation of the retrieved values, as well as the mean of the 1-σ error bars for the optical depth, ice fraction, and sizes of the water and ice particles. These simulations were also used to determine a threshold for the RMS difference between the observed and

calculated (from the retrieved parameters) emissivity to serve as a convergence criterion. This threshold value was taken to be 0.010 for the simulations, and the percentage of cases where the retrieval "converged" for each simulation ensemble is given in Appendix C. This provides some measure as to which types of clouds are more challenging for the physical retrieval. The ensembles that had the lowest convergence percentage were the cases where the cloud was all-ice and the effective radius of the ice particles was 13.5 μm. The mean values of the retrieved parameters for the cases that are considered 'converged' in these ensembles are very close to the true values.

Of the four retrieved parameters, the one with the greatest information content in the spectrum is optical depth. Over this set of ensembles, the mean retrieved τ was within 2% of the true value of τ for all cases. The difference between the mean value for the other retrieved parameters and at its true value was much more variable and is a function of the cloud's optical depth. The claim that the information content for τ is higher than the other parameters is also evident by comparing the ratio of the standard deviation of the ensemble to the mean value for each of the retrieved parameters; it is much smaller for τ than for any of the other retrieved parameters.

The results in Appendix C for particle size retrievals (when the cloud is a single-phase cloud) and ice fraction are graphically displayed in Figure 8.6. This figure is broken down into the results for water-only clouds (top), ice-only clouds (middle), and mixed-phase clouds (bottom). These statistics were derived in runs 10-14, 15-19, and 20-24 in Appendix C, respectively. Five different optical depth bins were used: 0.2, 0.5, 1.0, 2.0, and 4.0, and these bins are oriented along the x-axis. For the single-phase clouds, different colored symbols are used for the different true particle sizes. For example, in the liquid-only clouds,

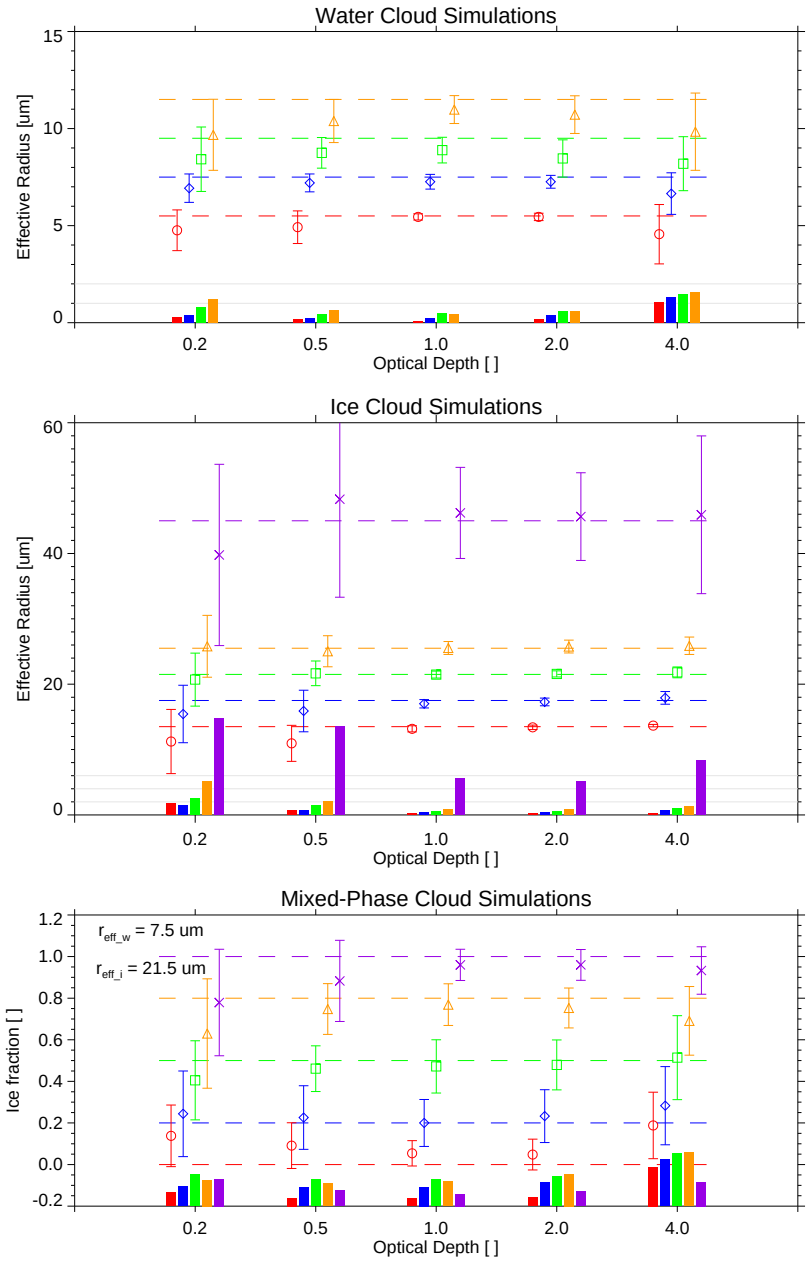

Figure 8.6: Summary of the simulation testing, using the cases listed in Appendix C. Symbols with error bars indicate the mean retrieved value with its standard deviation for the 60 samples in the case. The histograms at the bottom indicate the mean size of the 1-σ error bars. The horizontal dashed lines indicate the true values associated with each colored symbol. The plots are arranged as all-liquid clouds (top), all-ice clouds (middle), and mixed-phase clouds (bottom).

the colors red, blue, green, and orange are associated with the true effective radii of 5.5, 7.5, 9.5, and 11.5 μm, respectively. Colored dashed lines across the plot visually identify the true values. The symbol with the error bar represents the mean and standard deviation of the retrieved effective radius for the ensemble, while the bar at the bottom of the plot indicates the mean size of the 1-σ uncertainty value that is provided by the

optimal estimation technique.

One of the first conclusions that is readily apparent is that the uncertainty in the retrieved particle sizes in the liquid-only and ice-only clouds is larger for the smallest and largest optical depths than for intermediate values of τ. The liquid water simulation results (Figure 8.6, top) indicate that the retrieval algorithm always underestimates the retrieved droplet size. This can be explained by considering the mixed-phase results in the bottom panel of Figure 8.6. In this panel, note how the liquid only clouds (in red circles), which have a true $f_i = 0$, instead have mean values of f_i between 5%-20%. The introduction of a small fraction of ice in these cases results in the underestimation of the size of the liquid water droplets by explaining some of the spectral signature with larger ice particles. This phenomenon becomes more pronounced as the liquid water droplets become larger, explaining why the underestimate of the size of the liquid water droplets increases with true droplet size (Figure 8.6, top).

The retrieved particle size of ice-phase clouds (Figure 8.6, middle) does not show this bias, however, even though the retrieved f_i is often less than unity for these clouds (Figure 8.6, bottom). The algorithm does underestimate the crystal size for crystals below 20 μm when $\tau \leq 0.5$. Interestingly, the physical retrieval is also able to retrieve the crystal size in clouds with large crystals (45 μm and 70 μm – the latter is not shown but the results are in Appendix C) with some accuracy, especially when $\tau \geq 1$, although the uncertainty in these retrieved sizes is significant. When the optical depth was less than unity for these large crystal ice clouds, the retrieval algorithm tended to either correctly classify it as an all-ice cloud or

incorrectly indicate it was an all-liquid cloud – there were very few instances where the algorithm indicated that it was a mixed-phase cloud.

The skill of the algorithm in retrieving the phase of the cloud is illustrated in the bottom panel of Figure 8.6. In this panel, 5 different ice fractions, corresponding to different colors, are used: 0.0 (all-liquid), 0.2, 0.5, 0.8, and 1.0 (all-ice). The clouds have varying optical depths, but the effective radii of the particles are fixed to $r_{e,w}$ = 7.5 μm and $r_{e,i}$ = 21.5 μm. As discussed earlier, the retrieved ice fraction is biased towards the center; i.e., the algorithm tends to always want to include some ice and some liquid in each cloud, which is caused by the uncertainty in the emissivity observations between 400–600 cm^{-1}. This phenomenon is more pronounced when the cloud emissivity is near one of the extremes (i.e., small or large optical depth), where there is less information in the spectrum to separate the two phases. In general, however, the algorithm demonstrates excellent skill in determining the ice fraction, and hence the phase, of the cloud.

The physical retrieval can easily be turned from a "full" retrieval to a single-phase retrieval by modifying the *a priori* values in the parameter file, as indicated in Chapter 7. Run 4 was reprocessed with the algorithm in ice-only mode, and the results were compared to the full retrievals. Naturally, f_i = 1.0 for all values of τ in the ice-only retrieval, whereas it ranged from 0.84 to 0.97 for the full retrieval. The values of τ and $r_{e,i}$ were within 1% of their true values for the ice-only retrievals. Also, the 1-σ uncertainty in τ was about 3-6 times smaller for the ice-only retrievals compared to the full retrievals, and the 1-σ uncertainty in $r_{e,i}$ was about 2-3 times smaller. Similar results occurred when Run 5 (all all-liquid cloud) was reprocessed with the algorithm in liquid-only mode. Again, the retrieved values of τ and $r_{e,w}$

was within 1% of their true values for the liquid-only retrieval. The 1-σ uncertainties in τ and $r_{e,w}$ were reduced 4-15 times for τ and 3-4 times for $r_{e,w}$. These large reductions in the uncertainties in τ and r_e result in much lower uncertainties in the derived integrated water path. Therefore, if accurate observations of the water path are required and there is a priori knowledge of the phase of the cloud, then this algorithm should be run in single-phase mode.

Another investigation performed using these simulated clouds was to ascertain the sensitivity of the results to the number and location of the microwindows used in the physical retrieval. The basic skill of the retrieval algorithm is judged by comparing the mean retrieved parameter against its true value for all parameters in all simulations. As indicated in Chapter 7, the algorithm's skill was essentially the same for different numbers/locations of microwindows, as long as microwindows were chosen in each of the three primary spectral regions. However, the uncertainty in the retrievals (indicated both by the standard deviation of the retrieved values and the size of the 1-σ error bars) was a strong function of the number of channels used. For example, using a subset of 5 microwindows from Table 7.1, which included the channels centered at 18.84, 17.85, 12.20, 11.09, and 8.86 μm, resulted in approximately 4 times larger 1-σ error bars and the standard deviation of the retrieved values increased by approximately a factor of 2. However, the execution time of the algorithm is approximately linear with the number of microwindows used, and thus the retrieval using 5-channels was approximately 4 times faster than the retrieval using the standard 23 channels. Therefore, accuracy can be traded off for execution speed without introducing a bias in the results.

8.3. Validation with real observations

The approach taken to validate the retrieved cloud properties from this algorithm is to validate the results in "simple" single-phase clouds. There are several techniques available to retrieve cloud properties in liquid-only and ice-only clouds, but there are relatively few techniques available for mixed-phase clouds. Some in situ data was collected via aircraft during the FIRE-ACE experiment over the SHEBA ship from May-June 1998 (Lawson et al. 2001), but most of those flights were in clouds that had infrared optical depths above 5. Furthermore, an instrument that makes spectrally resolved observations at the surface between 850-1050 nm was not deployed during this experiment so that comparisons could be made between the algorithm by Daniel et al. (2002) and this AERI algorithm. The retrievals of mixed-phase properties from the millimeter-wave cloud radar and microwave radiometer are promising (Shupe et al. 2001). However, Hobbs et al. (2001) have shown that in some cases the presence of only a few ice crystals in a liquid water cloud adds significant uncertainty in the radar-retrieved water content due to the sensitivity of the 35 GHz radar to large particles.

8.3.1. LIQUID WATER CLOUD VALIDATION

Data collected on 15 May 1998 over the SHEBA ship was used to evaluate the liquid water retrievals from the AERI physical retrieval. From 1900-2400 UTC, a liquid water cloud existed above the ship that had an infrared emissivity less than unity. Several other groups (Lawson et al. 2001, Dong et al. 2001, Shupe et al. 2001) have studied this case, providing multiple data sets for validation. The backscatter and depolarization ratio observed

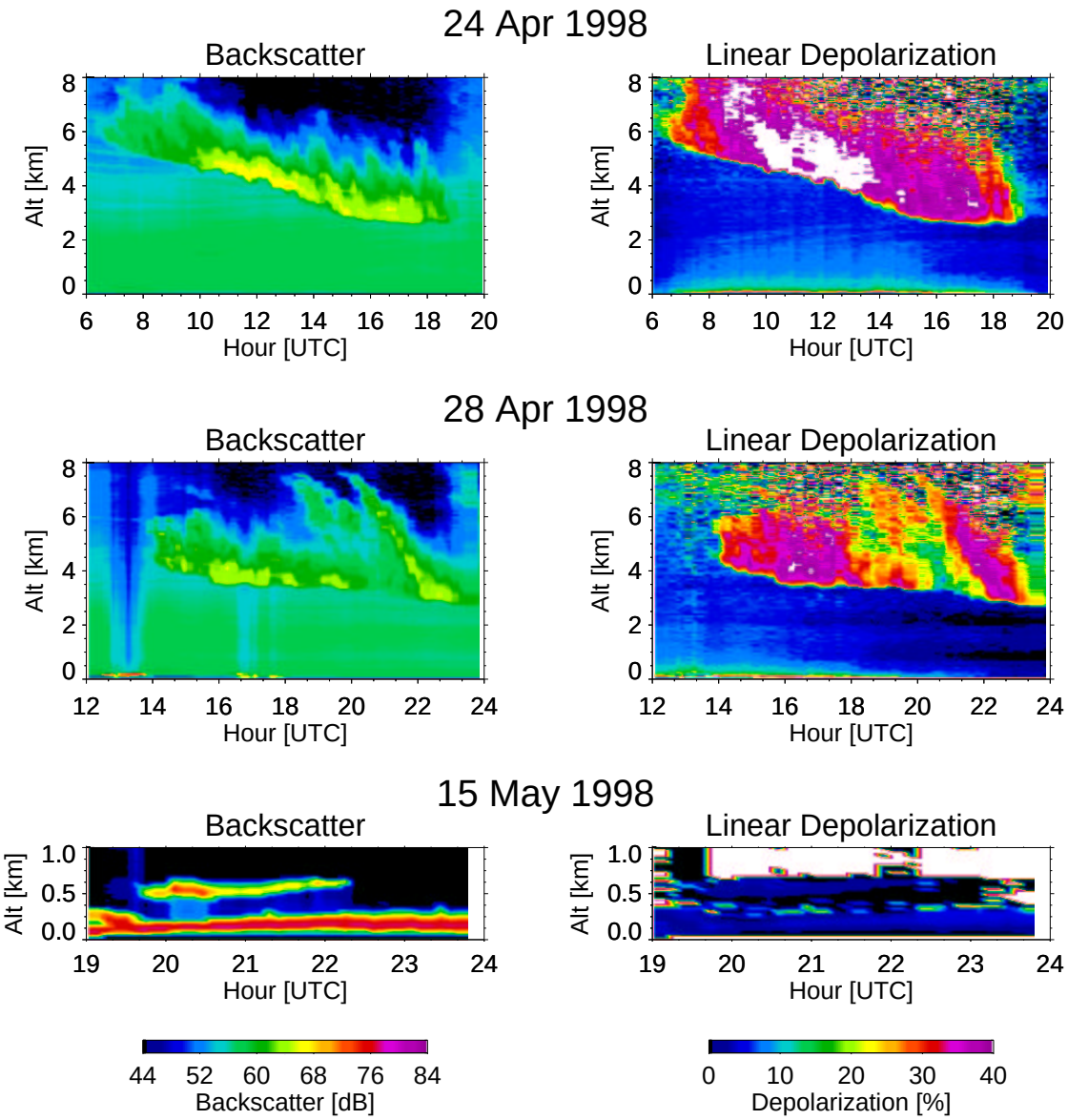

Figure 8.7: Time-height cross-sections of backscatter and depolarization ratio observations from the DABUL for three days during SHEBA.

by the DABUL during this day are presented in Figure 8.7. Note that during this period, a second cloud layer appeared between approximately 1930-2215 UTC. The low depolarization ratio (< 8%) observed by the lidar in the cloud layers from 1900-2400 UTC indicate that nonspherical ice particles are not present.

The LWP and r_e results from the AERI physical retrieval for this period are shown, with the error bars denoting the 1-σ uncertainty in the retrieved values, in Figure 8.8. These results are compared against the standard statistical retrievals that ARM provides with the observed brightness temperature from the microwave radiometer (Liljegren and Lesht 1996). A physical retrieval for the MWR data using an optimal estimation approach was also developed as part of this study, where the forward model is a combination of the Rosenkranz water vapor and oxygen absorption models (Rosenkranz 1998) and Liebe et al. (1991) liquid water absorption model. Westwater et al. (2001) have suggested that using this model combination (Rosenkranz and Liebe) results in more accurate PWV and LWP retrievals than the standard ARM retrieval model. Dong et al. (2001) use the MWR-observed LWP (in this case from standard ARM retrievals) together with solar flux observations and an iterative δ-2 stream model to retrieve r_e; these results are also shown. Retrievals from two different millimeter-wave radar methods are also plotted for comparison. The Frisch et al. (1995) method uses the MWR to constrain the LWP, and by assuming that the droplet concentration and size distribution are constant with height, the effective radius can be retrieved from the radar reflectivity. The forward model used in the MWR retrievals for the Frisch method is the same model combination used in the physical microwave radiometer retrievals (T. Uttal, personal communication, 2002). The Shupe et al. (2001) method is a reflectivity-based regression that is based upon aircraft observations during FIRE-ACE. This method also assumes a constant number density and droplet size distribution with altitude. Finally, observations from an FSSP probe on the C-130 are also provided.

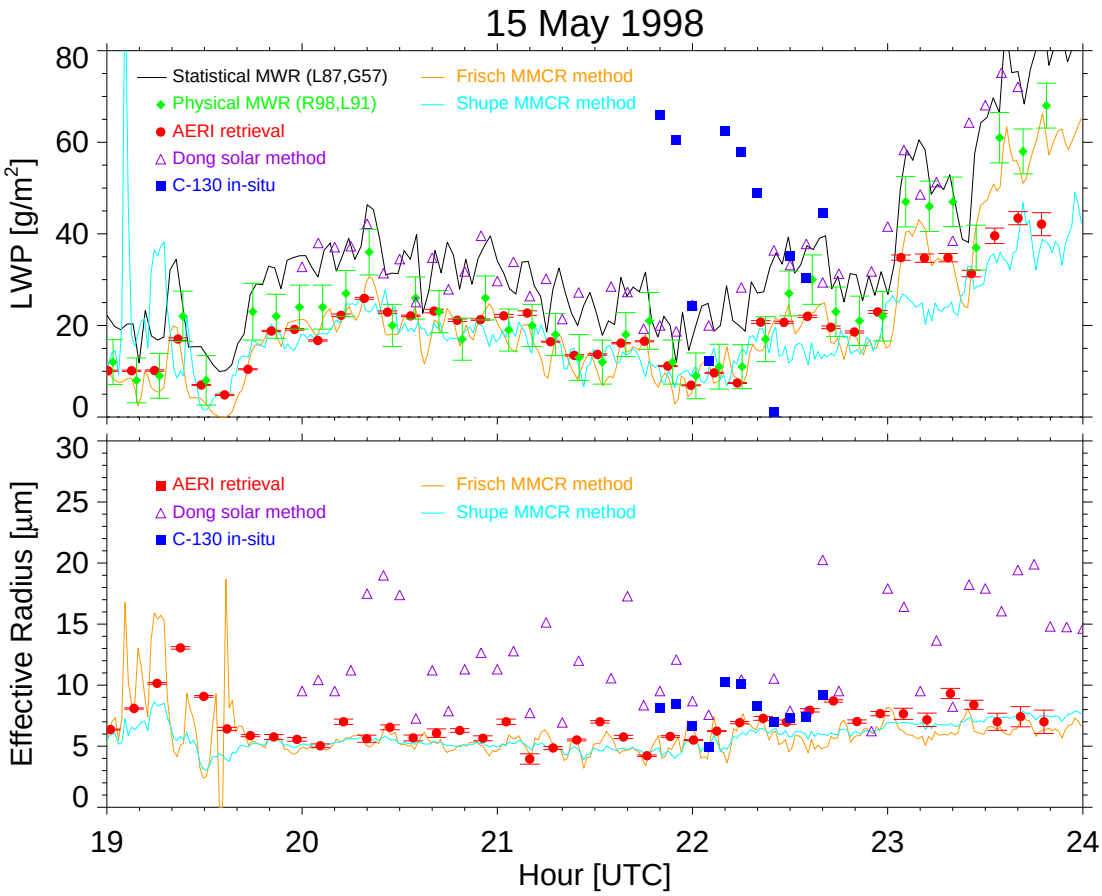

Figure 8.8: Comparison of LWP (top) and effective radius (bottom) measurements from a variety of different techniques for the liquid water cloud on 15 May 1998. See text for details.

The comparison of the different methods to measure LWP shows excellent agreement between the AERI physical retrieval, the MWR physical retrieval, and the two radar methods (Figure 8.8). Note that this agreement is essentially unchanged by the presence of the second cloud layer from 1930-2215 UTC. There is considerable scatter in the FSSP observations of LWP, which makes them not very useful in this evaluation. The Dong et al. method does not retrieve LWP, but rather uses the MWR retrieved value as a constraint to retrieve the effective radius of the droplets; that explains the good agreement between the Dong results and MWR statistical retrievals.

The retrieved droplet size for the AERI and radar methods also show excellent agreement, with the AERI results being slightly higher than the r_e values retrieved from the radar methods. However, the AERI results are in better agreement with the in situ observations made by the aircraft, which lends confidence in the AERI retrievals. The retrieved droplet size by the Dong method overestimates the droplet size, but this bias may be caused by the overestimate of the LWP that resulted from using the statistically-retrieved LWP from the MWR as the constraint.

8.3.2. ICE CLOUD RETRIEVALS – SENSITIVITY TO HABIT

Ice cloud retrievals are more difficult to validate because of the challenges with modeling the shape of the ice crystals. This affects both the evaluation of the retrieved IWP and particle size.

The AERI physical retrieval of IWP and cloud phase is very sensitive to the assumed shape of the ice particles. The ice crystals could be modeled as spheres, allowing the single scattering properties to be computed using Mie theory, or as either droxtals or hexagonal columns, where the single scattering properties have been computed with a combination of FDTD, SSPM, and geometric optics methods. [FTDT calculations are extremely expensive. At the time of this writing, FTDT calculations for hexagon plates is ongoing, with the calculations for bullet rosettes to follow.] Naturally, mixtures of these three habits could be generated, where one crystal type such as droxtals could be used for smaller crystals in a given size distribution and other crystal types for the larger sizes.

An ice-only cloud that was very sensitive to the habit used in the AERI retrievals occurred over the SHEBA ship on 24 April 1998 (Figure 8.7). This cloud is most certainly all ice due to the very large (>30%) depolarization ratio observed by the DABUL. The infrared optical depth of this cloud ranged from 0 to 2.5 and the temperature of the cloud increased from 230 K at 0600 UTC to 250 K by 1900 UTC. Five crystal distributions were used in the AERI retrievals for this day: 1) hexagonal columns for all crystals, 2) droxtals for crystals with effective radii of 16 μm or smaller and hexagonal columns for larger crystals, 3) spheres for crystals with effective radii of 16 μm or smaller and hexagonal columns for larger sizes, 4) spheres for crystals with effective radii of 40 μm or smaller and hexagonal columns used for larger crystals, and 5) spheres for all crystals. The differences in the single scattering

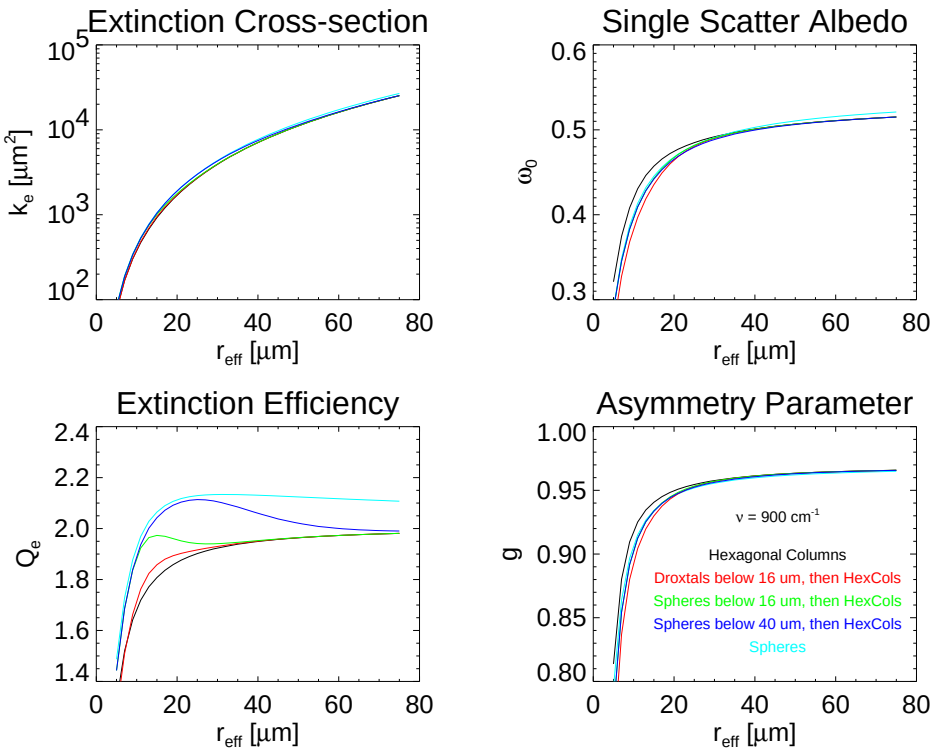

Figure 8.9: Single scattering properties at 900 cm^{-1} as a function of effective radius for the 5 different ice crystal distributions described in the text.

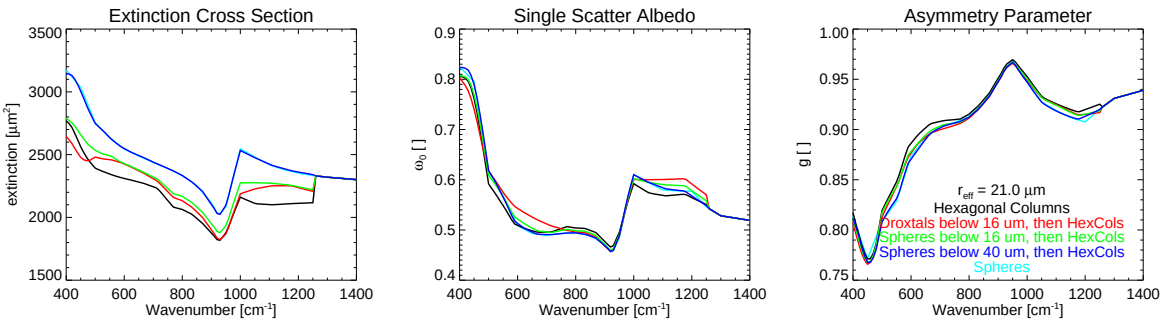

Figure 8.10: Single scattering properties as a function of wavelength for the 5 different ice distributions described in the text. The effective radius of the particle distribution is 21 μm.

properties for these 5 ice crystal distributions as a function of effective radius at 900 cm^{-1} is shown in Figure 8.9, and the spectral dependence of the scattering properties for $r_{e,i}$ = 21 μm is shown in Figure 8.10.

The retrieved ice fraction and particle sizes for the ice and liquid components are shown in Figure 8.11, where the $r_{e,w}$ values have been multiplied by 2 for display. In all 5 cases, the retrieval increasingly tended to err and classify the cloud as a liquid-water only cloud after 1200 UTC. This could be due to changes in the shape of the cloud microphysical properties as the cloud warmed over this period. However, treating the ice particles as spheres or a combination of droxtals and hexagonal columns yielded the best retrievals of ice fraction (i.e., the most values of f_i = 1) over the entire time period. Note also that the retrieved effective radius of the ice particles is very similar for these two distributions. Images collected by the Cloud Particle Imager (CPI) during SHEBA indicated that small (< 40 μm) ice particles in cirrus are largely spheroidal in shape (Lawson et al. 2001), which could explain why droxtals and spheres seem to fit the observations better. Lawson et al. (2001) also reported that CPI observations in Arctic cirrus clouds often showed high concentration of small ice particles with low concentrations of large particles (which were primarily bullet rosettes). However, as will be shown later, even though the two distributions (all spheres and

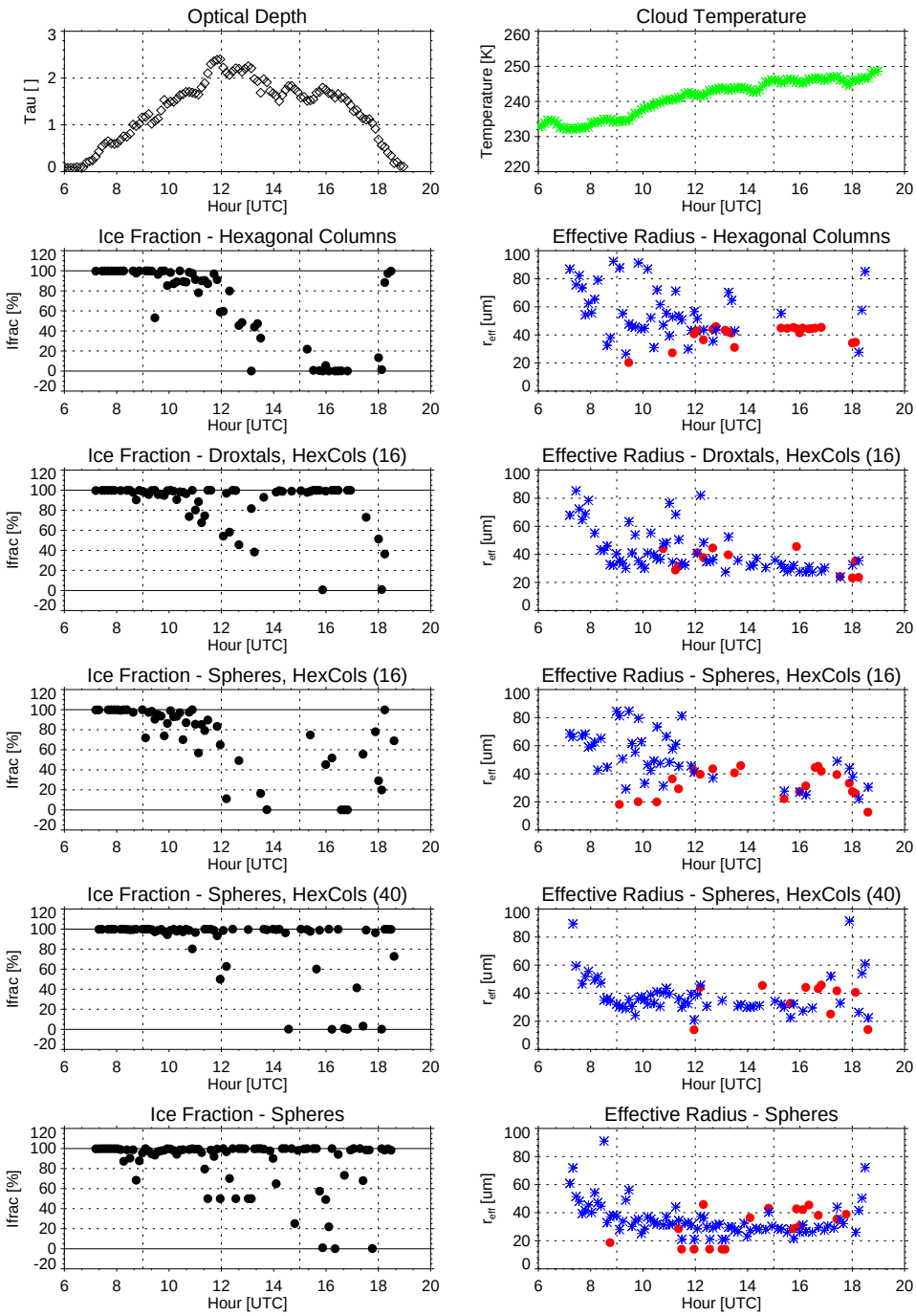

Figure 8.11: Retrieved ice fraction and effective radius during the cirrus event on 24 April 1998. The best results occur when the ice is assumed to be droxtals/hexagonal columns or spheres. The retrieved optical depth and cloud temperature are also provided.

droxtal/hexagonal columns) yielded similar results for ice fraction and particle size, the derived IWP for the two habits are markedly different.

8.3.3. ICE CLOUD VALIDATION

Several millimeter-wave radar based methods have been applied to SHEBA data to retrieve both IWP and effective crystal size. The first technique (Matrosov 1999; henceforth called Matrosov99) is a radar-radiometer technique that uses a sky IR brightness temperature, which is calculated from the AERI at 11 μm, to estimate the cloud optical depth. This optical depth is then used to constrain the retrieval of cloud ice water content (IWC) from the reflectivity observations. The IWC is then integrated over the cloud thickness to provide IWP. Then, using the Brown and Francis (1995) density-size relationship, a characteristic particle size is determined. The visible optical depth is assumed to be twice the infrared optical depth derived from the AERI observations. This assumption is only valid for certain particle sizes and depends on habit, as illustrated in the extinction efficiency image in Figure 8.9.

The second radar-based algorithm retrieves IWC from a reflectivity-based regression using coefficients derived from other multi-measurement techniques (Shupe et al. 2003, to be submitted to *J. Appl. Meteor.*; henceforth referred to as the Shupe method). From these IWC measurements, the IWP and particle size are determined as in the Matrosov99 method. In this case, the visible optical depth is computed as τ = IWP * (0.019 + 1.27 / D_e).

The third radar method uses the Doppler moments observed by the cloud radar. The technique is based upon a relationship between the particle fall speed, which is derived from the radar Doppler velocities, and the particle size (Matrosov et al. 2002; henceforth referred to as Matrosov02). IWC is then derived from the Brown and Francis (1995) relationship, but in the opposite sense compared to the first two radar techniques. The IWC profile is then

integrated to yield IWP. Profiles of extinction, which are integrated over the cloud thickness to yield the shortwave optical depth, are computed following Matrosov et al. (2002).

It should be noted that the effective diameter D_e used for the radar retrievals follows the definition from Mitchell (2002), which is defined as

$$D_e = \frac{1.5\, IWC}{\rho_i\, A} \tag{8.1}$$

where ρ_i is the bulk density of ice and A is the total projected area of the crystals. The total projected area is taken to be one half the visible extinction coefficient, which is computed from the visible optical depth. The effective radius is then D_e / 2. However, this formulation of effective radius is much different than the formulation used in this thesis, which is the ratio of the third moment to the second moment of the size distribution given in equation (5.11). Therefore, some discrepancies in the retrieved effective size of the particles should be expected.

A comparison between these three MMCR-based methods and the AERI retrieval using both spheres and droxtals/hexagonal columns for 24 April 1998 is shown in Figure 8.12. Recall that the lidar backscatter and depolarization data is shown in Figure 8.7. There is some enhanced scatter in the AERI retrievals caused by the occasional misidentification of the cloud's phase as discussed earlier. However, the AERI-retrieved IWP for the case when the ice crystals are assumed to be spherical agrees very well with the Matrosov99 method. If the droxtal/hexagonal column habit is used, the retrieved IWP is about a factor of 2 larger than the IWP derived using from spheres, and is much larger than the IWP retrieved from any of the MMCR-based methods. Note that there is significant differences (factor of 3 or larger) between the IWP derived from the three radar methods.

Another interesting case occurred on 28 April 1998 over the SHEBA ship (Figure 8.13). Again, there is significant spread between the MMCR retrievals of IWP, but this time the Matrosov02 results have the highest IWPs whereas the Matrosov99 method had the highest IWPs on 24 April. The AERI results still demonstrate that the IWP retrieved using the droxtal/hexagonal column habit is approximately twice the IWP retrieved when the ice are modeled as spheres. However, this time, the droxtal/hexagonal column retrievals agree well with the Matrosov99 results, and the spherical IWP retrievals are in very good qualitative agreement with the Shupe reflectivity technique. An interesting, and unexplained, excursion

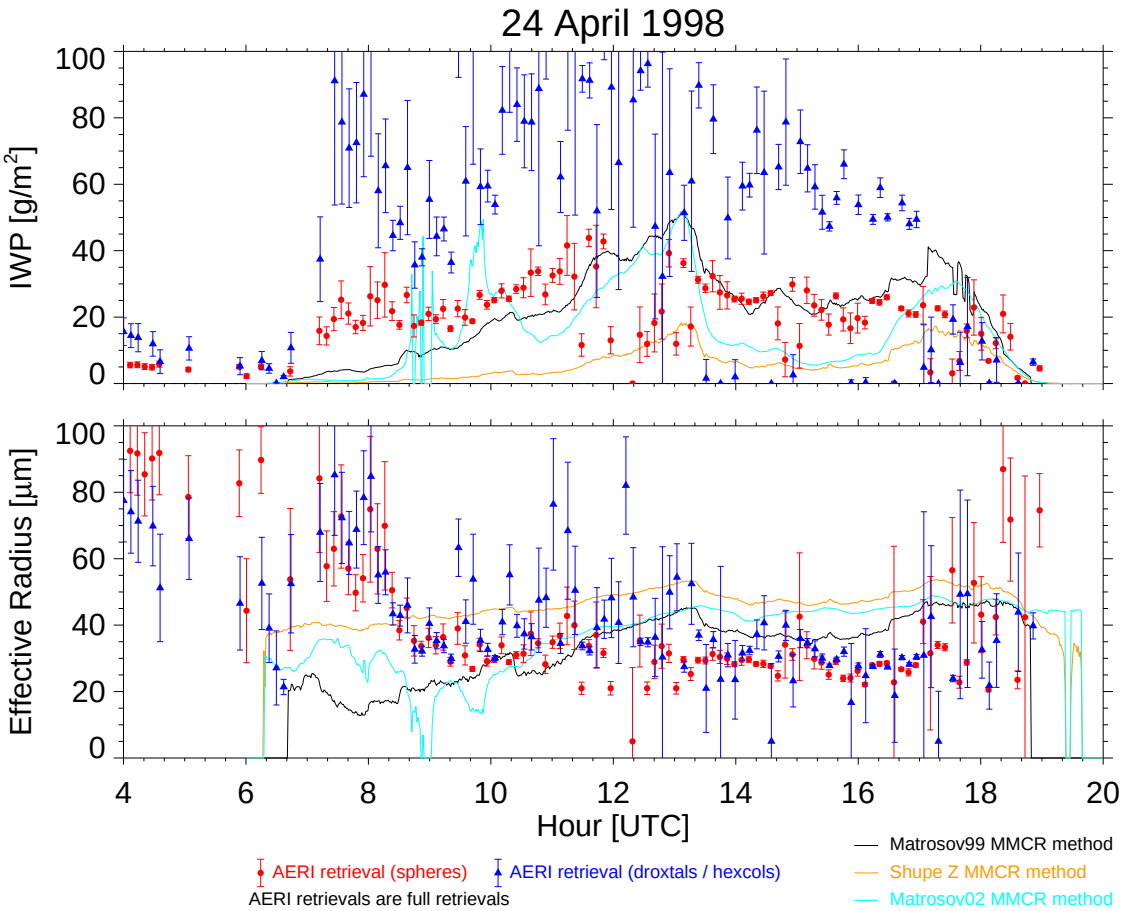

Figure 8.12: Comparisons of IWP and effective radius by various techniques for the cirrus cloud on 24 April 1998. See the text for details.

in the droxtal/hexagonal column retrievals occurred between 1715-1815 UTC and again between 2000–2030 UTC, where the retrieved IWPs are significantly higher than any of the other IWP results. The spherical IWP retrievals do not appear to show significant differences in their character, but the effective radius retrieved using both the spherical and droxtal/hexagonal column habits during these time periods is higher than during the surrounding periods. However, in general the AERI-retrieved IWP values tract the trend in the MMCR-based IWP retrievals very well.

One question that might be asked is "How different are the retrieved results if the algorithm was restricted to perform a single-phase retrieval?" These results are provided in

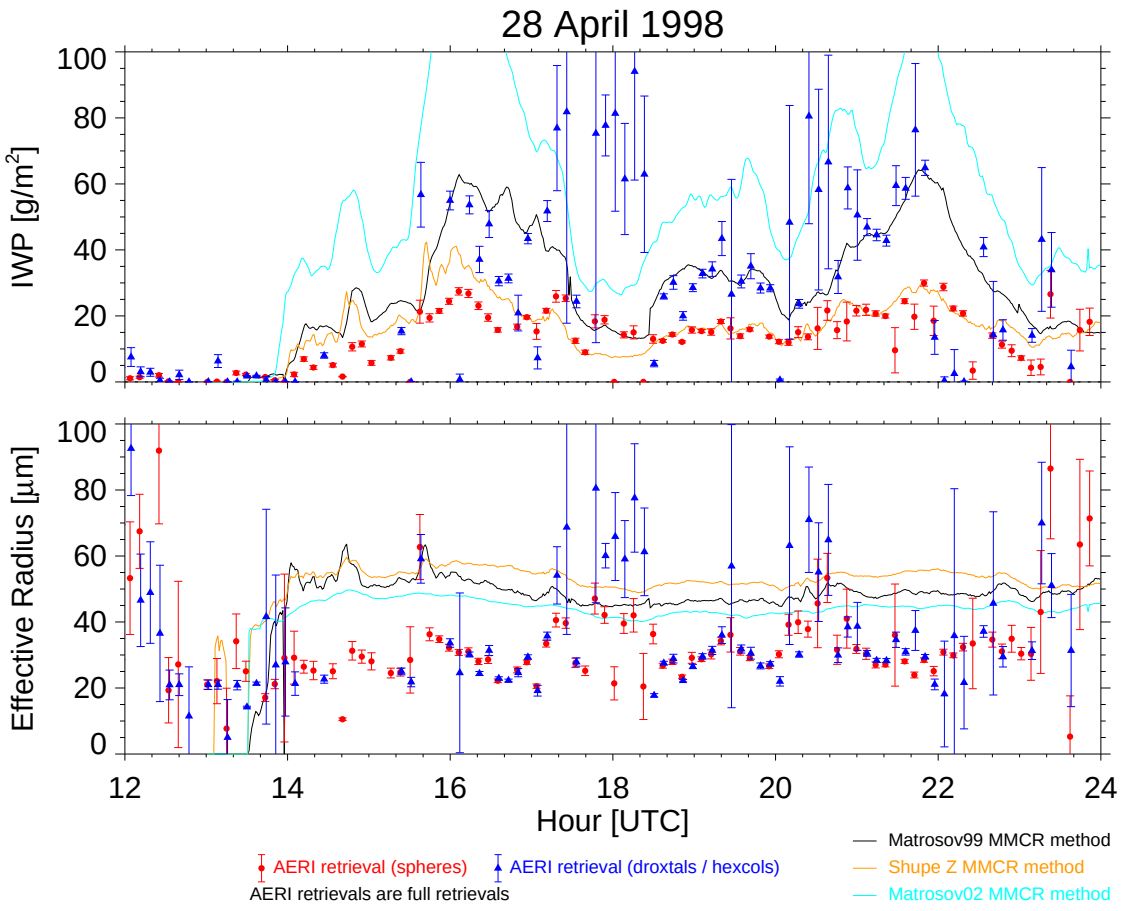

Figure 8.13: Same as Figure 8.12 for 28 April 1998.

Figure 8.14 for 28 April 1998. These results are significantly less noisy than the full AERI retrievals presented in Figure 8.13, but the results are generally the same as the full retrievals. The single-phase retrieval also indicates that that the full retrieval starts to confuse the cloud's phase for this case when the effective radius of the ice particles is greater than approximately 50 μm.

While there is large variability in the MMCR-based IWP results shown in Figure 8.12 and Figure 8.13, the same amount of variability is also demonstrated at the SGP CART site (e.g., Sassen and Mace 2002). Also, the retrievals at the SGP site demonstrate that they bracket in situ observations made by aircraft fairly well (J. Mace, personal communication,

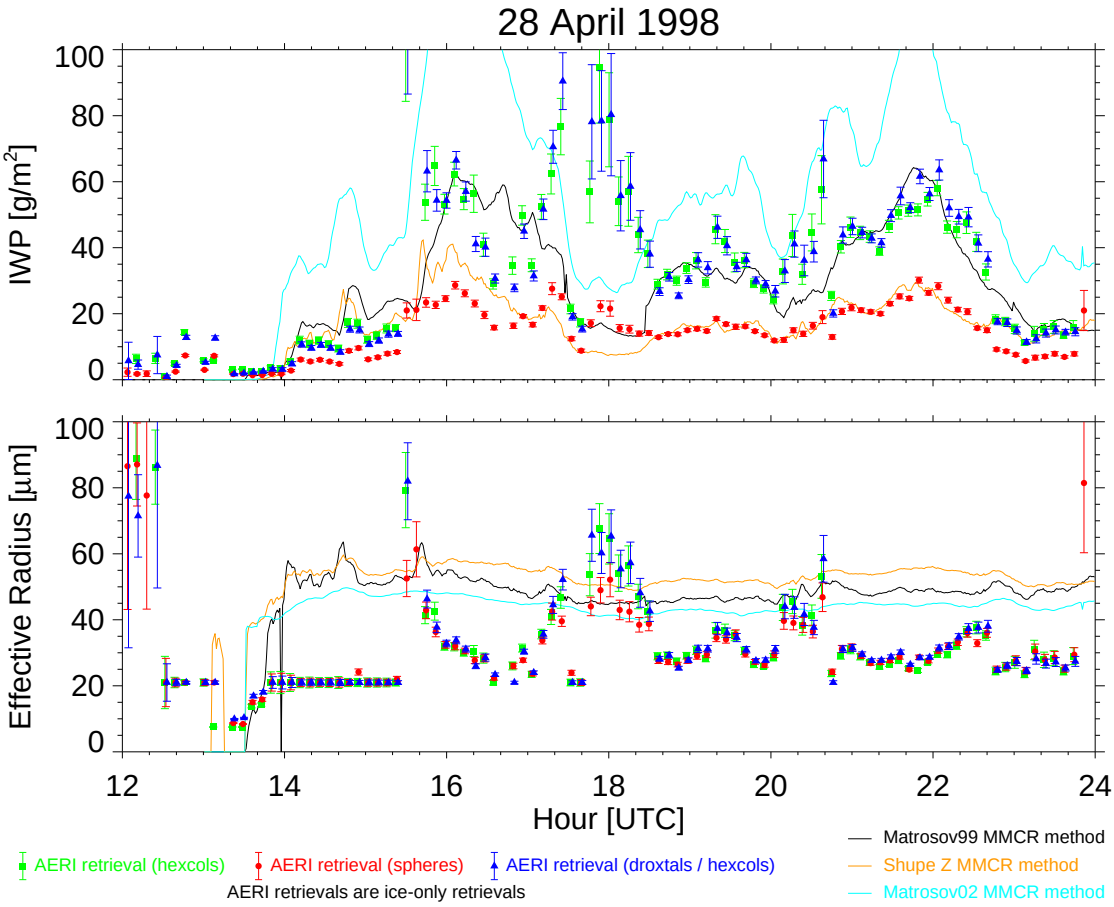

Figure 8.14: Same as Figure 8.13, except the retrieval was constrained to an ice-only retrieval.

2002). Therefore, based upon this observation, it would appear that treating the ice crystals as spheres may represent the actual conditions better than the droxtal/hexagonal column habit, even though the latter habit may be more realistic. In any regard, infrared retrievals of IWP are very sensitive to ice particle habit, and thus large uncertainties in IWP will exist unless the habit of the cloud can be retrieved. The retrieval of ice habit from remote sensing data is beyond the scope of this work.

Chapter 9

9. Results from SHEBA

The SHEBA campaign started in October 1997 and wrapped up in early September 1998. During this period, both the AERI and the DABUL operated normally from late October to early June, with the exception of a few weeks in February when the laser in the DABUL required maintenance. The physical retrieval was applied to the data, and a monthly histogram showing the number of cloudy retrievals per month is shown in Figure 9.1. The decrease in the number of samples in December and January is due to the increased occurrence of clear skies, as these months were the least cloudy during the SHEBA campaign (Intrieri et al. 2001). The DABUL's laser required maintenance during February, which explains the decreased number of cloud samples in that month.

The distribution of retrieved cloud optical depth at 900 cm^{-1} to emissivity is shown in Figure 8.2. As indicated earlier, the variance in the optical depth for a given emissivity value is primarily a function of phase, although the sizes of the water and ice particles also plays a role. When the emissivity is below 0.05 or above 0.95, the cloud emissivity spectrum is nearly gray; therefore, there the uncertainties in the

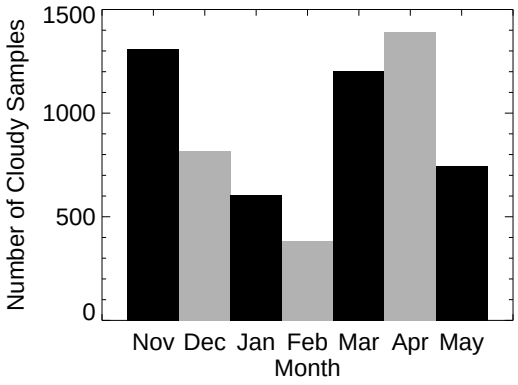

Figure 9.1: Number of valid cloudy retrievals for the SHEBA campaign.

retrieved ice fraction and effective sizes of the water and ice particles are quite large. Therefore, the data were screened to remove all cases where the emissivity at 900 cm^{-1} was not between 0.05 and 0.95. The mean optical depth of the clouds at SHEBA increased in late spring, and applying this screen explains why there were less cloudy retrievals in May than in either March or April (Figure 9.1).

In addition to screening the results by cloud emissivity, some other quality checks were also applied. These checks included ensuring that the AERI's hatch (which protects the fore optics from precipitation) was open, that the final RMS difference between the observed and calculated emissivity was below 0.060, and that the sky variance radiance at 900 cm^{-1} (discussed in Chapter 7) was below 0.1 RU. Also, if the retrieved particle size was the minimum or maximum allowed (as defined in Chapter 7), then the retrieval was thrown out. Finally, only retrievals where the uncertainty in the effective cloud temperature was less than 3 K were kept; this essentially removes any cases where the a multi-layer cloud has a separation between layers of over 2 km.

An example showing the results from the retrieval algorithm is shown in Figure 9.2. Two distinct cloud layers are present on this day: a high cirrus layer from approximately 0600 to 1800 UTC, and a mid-level cloud from 1800 to 2300 UTC. For the cirrus cloud, the effective cloud temperature is below –40 C, and thus the algorithm switched automatically into single-phase mode. Note that the optical depths associated with the cirrus cloud are quite small (less than 0.2). The retrieved particle size for this cirrus cloud ranged from 20 to 60 μm and appears to be correlated with the altitude and/or thickness of the cirrus cloud.

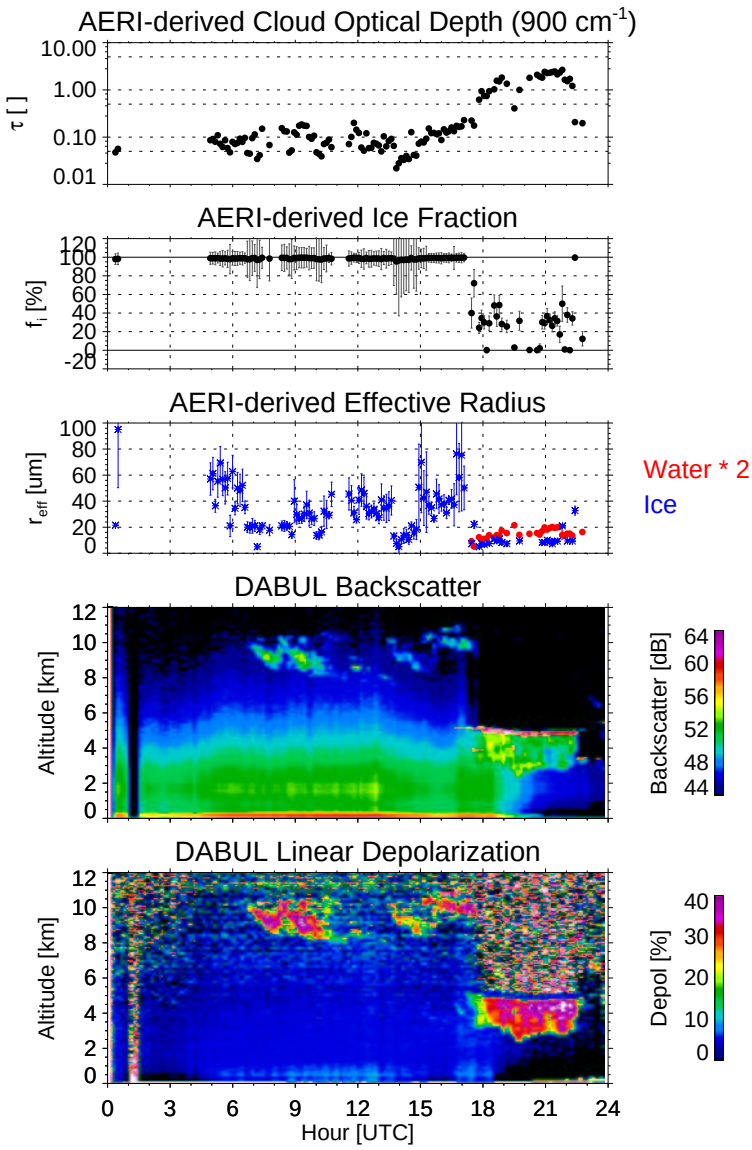

Figure 9.2: Example of the retrieved cloud properties (optical depth, ice fraction, and effective radius for water and ice particles) for 3 March 1998 over the Des Grosilliers. *The DABUL backscatter and depolarization data are also shown. See text for details.*

The mid-level cloud in Figure 9.2 has significantly higher optical depths, with a maximum optical depth approaching 2. The DABUL data demonstrate that there is a layer with high backscatter values at the top of the cloud near 5 km and the depolarization ratio associated with this layer is less than 10% -- this layer is most likely composed of mostly liquid water droplets. However, below this geometrically thin layer is a much thicker (geometrically) layer that extends down to approximately 3 km. This layer has much lower backscatter values than the layer at the top of the cloud, and the depolarization values are around 30% indicating that this layer contains ice crystals. The vertical structure of a geometrically thin liquid water layer over a thicker ice layer is predicted by models (e.g., Jiang et al. 2000, Girard and Blanchet 2001) and noted in

observations (e.g., Pinto 1998, Lawson et al. 2001) of Arctic clouds. The retrieved ice fraction varied from zero to near 40% for this mid-level cloud. The retrieved effective radius for the water droplets ranged from 5 to 10 μm (note that these values were multiplied by 2 on the figure) and the ice particles had an effective radius of approximately 10 μm for the mid-level cloud. Girard and Blanchet (2001), using a single column model with explicit aerosol and cloud microphysics, demonstrated that a mixed-phase Arctic cloud can have oscillations in the ice fraction due to the cyclic behavior in the activation cycle with much less variability in the cloud particle diameter, although the time period for the oscillations in the simulation were much longer than for this observed case.

The distribution of optical depth and ice fraction for the 7 month SHEBA period (November though May) is shown in Figure 9.3. The data show a wide range of optical depths, with a pronounced peak in the distribution around $\tau \sim 3$. The retrieved ice fraction indicates that ice clouds were present approximately 30% of the time during this period, water-only clouds roughly 20% of the time, and mixed-

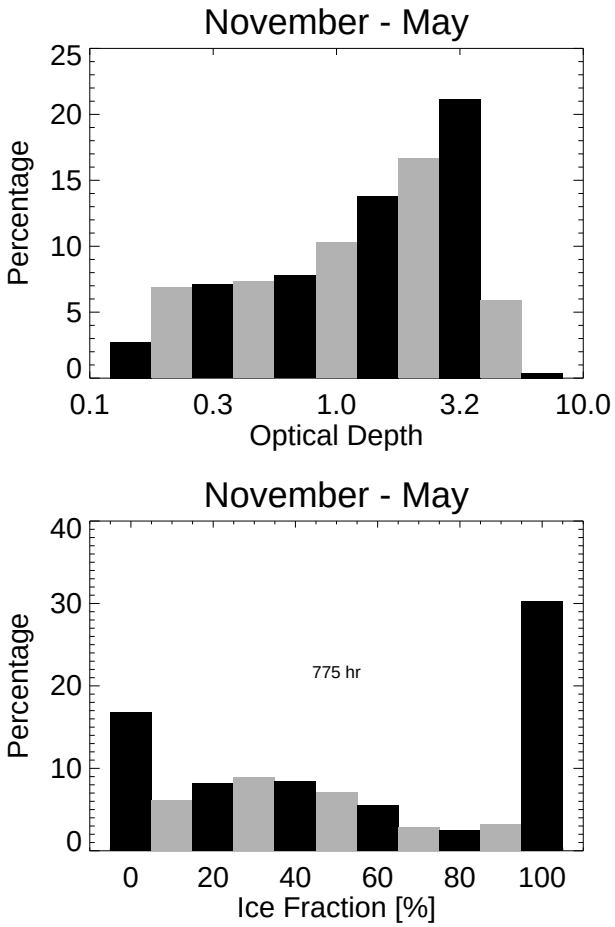

Figure 9.3: Distribution of optical depth and ice fraction during SHEBA.

phase clouds the remaining 50% of the time. Considering the same data plotted against cloud temperature (Figure 9.4), the optical depth data show some correlation with temperature, especially for temperatures below 240 K. The ice fraction data show that a significant number of liquid and mixed-phase clouds exist at temperatures as low as 240 K, but that primarily ice-only clouds exist below this temperature. However, there is no general trend in the retrieved ice fraction with increasing temperature, unlike the somewhat better defined relationship shown in Gregory and Morris (1996, Fig 2), which was derived from mid-latitude frontal cloud observations by Moss and Johnson (1993). The differences in the relationship between ice fraction and cloud temperature between Gregory and Morris (1996) and this work is probably due to different cloud locations, cloud types, and number of samples.

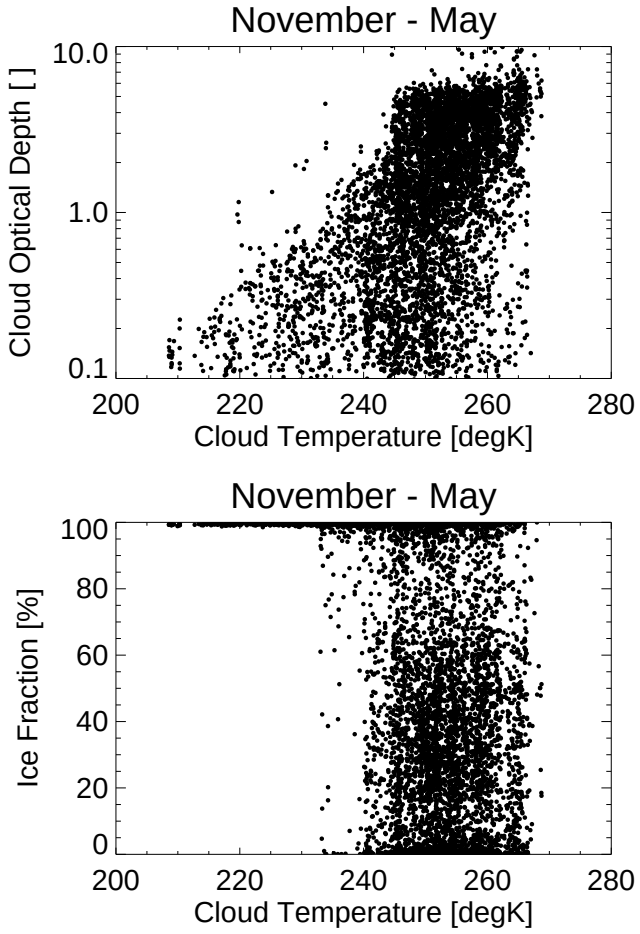

Figure 9.4: Scatterplot of optical depth and ice fraction as a function of cloud temperature during SHEBA.

The distribution of cloud optical depth as a function of ice fraction offers insight into dependency of the optical thickness of the clouds to cloud phase. Figure 9.5 shows

demonstrates that when the cloud is single phase (i.e., either all ice with f_i > 80% or all liquid with f_i < 20%) that there are significantly more optically thin clouds than when the cloud is a mixed-phase cloud (20% < f_i < 80%). The simulations (Figure 8.6) demonstrated that even when the optical depth is below 1 that the retrieval algorithm has good sensitivity to mixed-phase clouds, and therefore optically thin (i.e., τ < 1) mixed-phase clouds appear to have occurred rather sparingly during the SHEBA campaign.

A mixed-phase cloud is in a colloidally unstable state, yet this state can last several hours to several days. There are two common hypotheses that are used to explain the persistence of mixed-phase clouds in the Arctic. The first is the

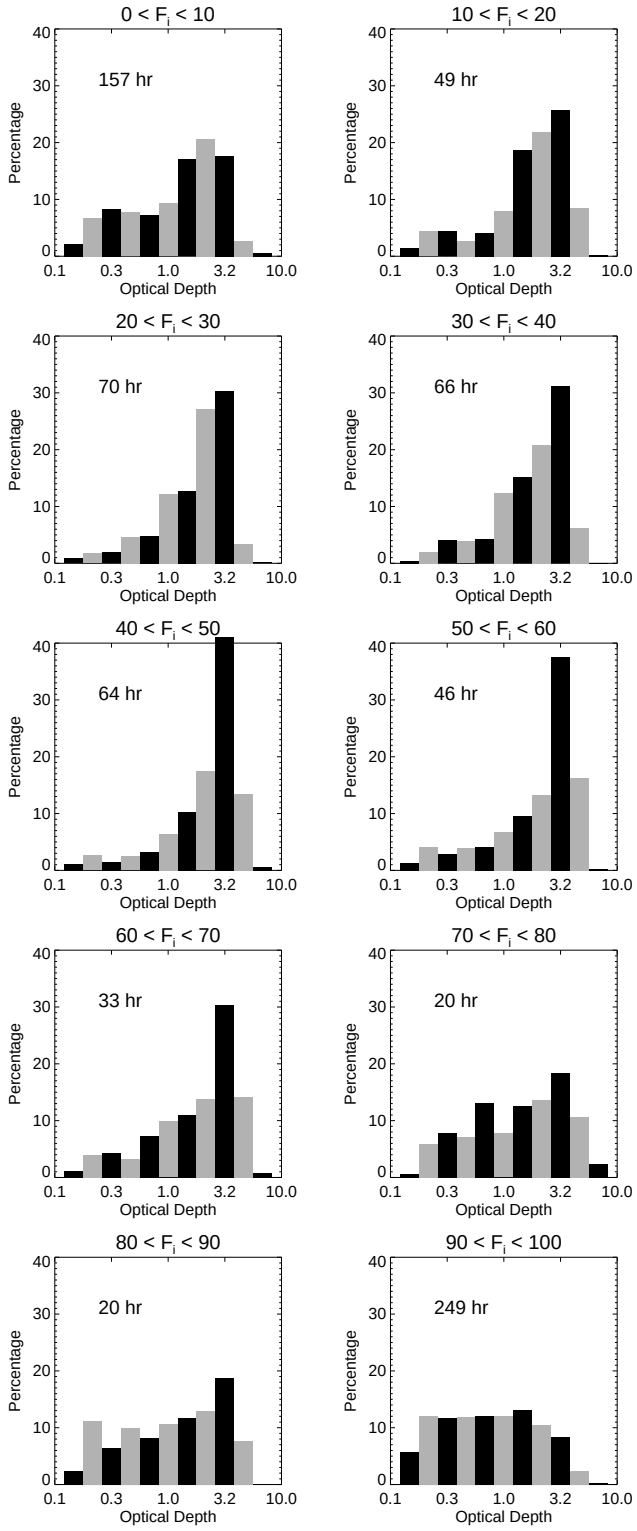

Figure 9.5: Distribution of cloud optical depth for different intervals of ice fraction during SHEBA.

relative paucity of ice nuclei in the Arctic. When there are few ice nuclei, the Bergeron process is very inefficient since the number of ice crystals is too small to absorb the excess water vapor produced by the evaporation of the water droplets; therefore, the ice supersaturation remains very high and the mixed-phase cloud persists (Girard and Blanchet 2001). The second explanation is that a significant convergence of water vapor must be occurring (Pinto 1998). This allows for the rapid regeneration of the liquid water component of the cloud, given that any ice that is present will work to scavenge liquid water droplets. Therefore, it seems likely that for a mixed-phase cloud to persist there must be an abundance of liquid water droplets, and thus a rather high cloud optical depth. If the cloud is optically thin, the number of liquid water droplets is small, and thus the presence of any ice will quickly remove these water droplets leaving the cloud as a single-phase (ice) cloud. Using this reasoning, the AERI observations appear to support the hypothesis that the convergence of water vapor is critical for the mixed-phase clouds to persist.

Another way to view the data in Figure 9.4 is to create distributions of τ and f_i as a function of cloud temperature. This is shown in Figure 9.6. For temperatures below 240 K, the cloud is indeed all ice, but the optical depth of the clouds increases with temperature (which is also shown in Figure 9.4). Significant numbers of liquid water and mixed-phase clouds occur when the cloud temperature is greater than 240 K. Figure 9.6 also demonstrates that as the cloud temperature increases, the optical depth distributions continue to shift towards higher values. Also, the fraction of the ice-only clouds decreases as the cloud temperature increases as more liquid-only and mixed-phase clouds appear. However, the reader should remember that cases of overlapping clouds (i.e., boundary layer clouds with cirrus above them) have been screened out of this data set.

Retrieving the effective particle size is important for the determination of the total water content of the cloud. Figure 9.7 presents distributions of the retrieved effective radii for the water and ice particles in both single and mixed-phase clouds from November through May. Clouds were considered to be a single-phase liquid or ice cloud if the retrieved ice fraction was less than 20% or more than 80%, respectively. These thresholds were suggested in part by the simulations discussed in Chapter 8. There were 207 h, 299 h, and 269 h (or 27%, 39%, and 35% of the total cases) of liquid-only, mixed-phase, and ice-only clouds, respectively, during this 7 month period.

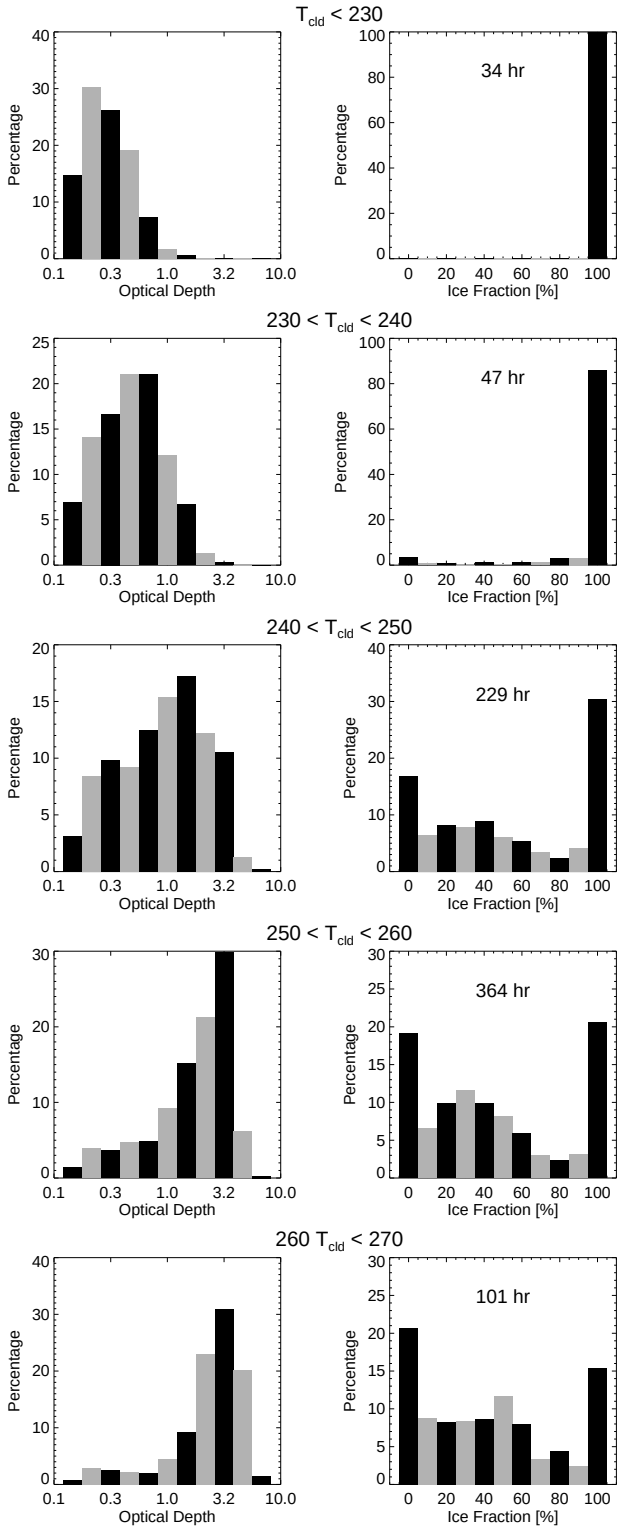

Figure 9.6: Distributions of cloud optical depth and ice fraction for different intervals of cloud temperature during SHEBA.

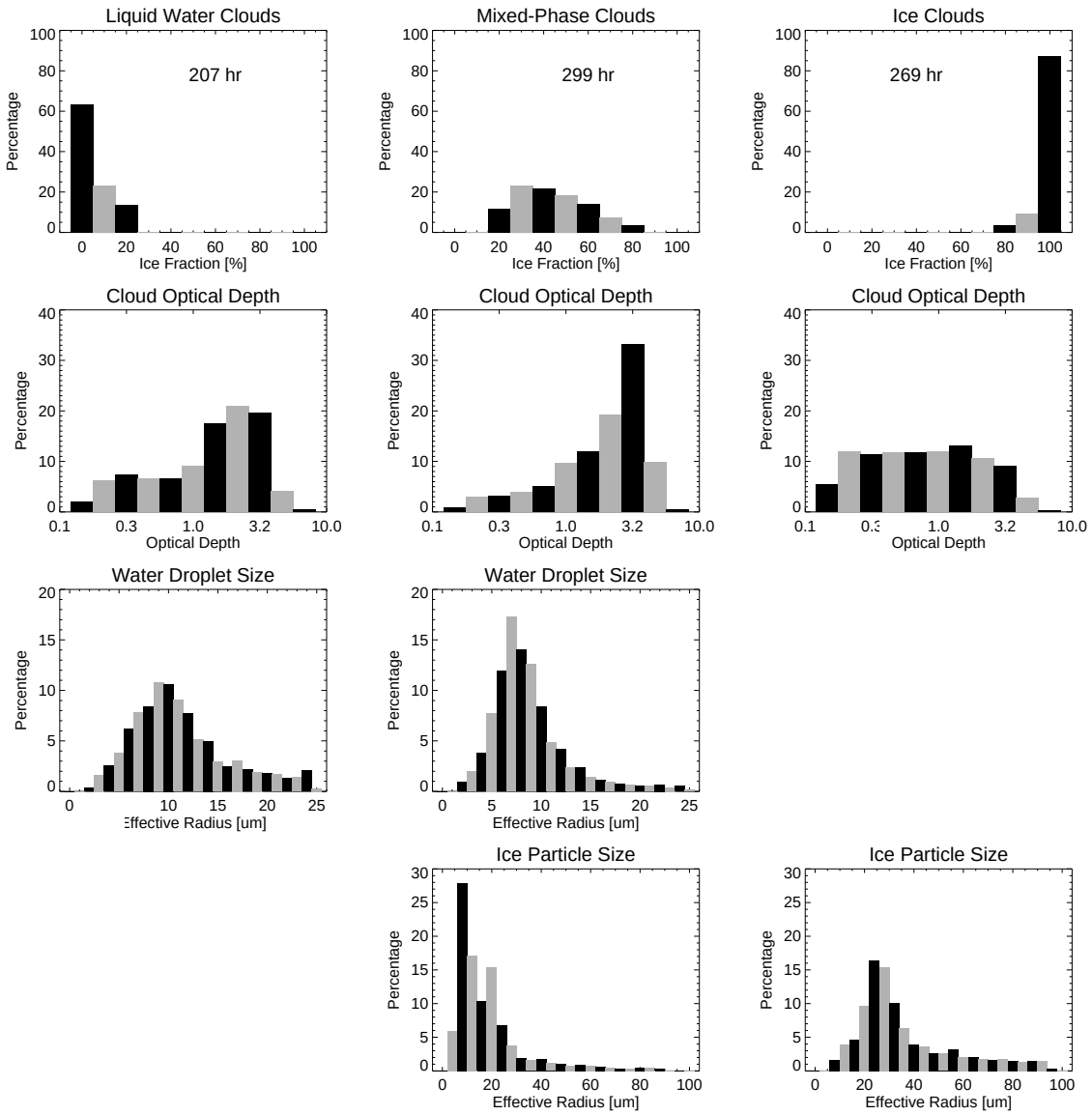

Figure 9.7: Distribution of ice fraction (top row), optical depth (2nd row), effective size of the water droplets (3rd row), and effective size of the ice particles (bottom row) for liquid-only (left), mixed-phase (center), and ice-only (right) clouds during SHEBA.

The distribution of $r_{e,w}$ for the liquid-only and mixed-phase clouds show that the mode effective radius is approximately 10 μm and 7 μm, respectively. There are also significantly more large liquid droplets in the single-phase liquid clouds than in the mixed-phase clouds. The lack of the larger water droplets in the mixed-phase clouds, which results in a shift to a smaller effective radius, is most likely because the larger droplets are more likely to freeze

(possibly splintering or shattering) and are thus removed from the size distribution (Rangno and Hobbs 2001). It should be noted that drizzle droplets have significantly larger effective radii (> 30 μm), but when drizzle conditions occur the cloud is typically opaque in the infrared, and these cases were thus screened out of the data set.

The distribution of the retrieved ice particle sizes for mixed and single-phase clouds for November through May is also shown in Figure 9.7. The effective radii associated with the ice-only cloud shows a mode radius of approximately 25 μm with a significant number of cases with larger effective radii. However, the mode ice particle size for mixed-phase clouds is approximately 10 μm and there are relatively few cases where the retrieved $r_{e,i}$ was larger than 50 μm in a mixed-phase cloud. This result appears inconsistent: one might expect ice particles to grow rapidly to large size (much larger than 10 μm) in the presence of large amounts of supercooled liquid water and thus the effective radius of these ice particles should be much larger. The effective radius is essentially the ratio of the volume to the projected area; therefore, if the ice particles were growing in a manner such that the surface area was increasing faster than the volume (such as by riming or aggregation) then the effective radius would decrease. However, simulations of Arctic clouds suggest that ice crystals grow by vapor deposition and that collision-coalescence plays a much smaller role in ice crystal growth (Harrington et al. 1999, Girard and Blanchett 2001), making the hypothesis of projected area growing faster than volume less likely. However, the use of 'equivalent' spheres can result in smaller effective radii and higher number density for certain ice habits (Grenfell and Warren 1999). Therefore, these results suggest that the shape of the ice particles in the mixed-phase clouds is best represented by a collection of small crystals.

A simulation (in the spirit of Chapter 8) was performed to evaluate if these small ice particles were an artifact of the retrieval or are possibly real, especially since the optical depth of mixed-phase clouds tends to be large. The downwelling radiance was computed for a cloud with an optical depth of 3, ice fraction of 30%, and particle sizes of 9 and 40 μm for water and ice particles, respectively. The physical retrieval was then applied to 60 instances of this radiance spectrum: the results are shown as Run 032 in Appendix C. The retrieved results show little bias and relatively small variability in τ, f_i, and $r_{e,w}$, but there is a significant bias in the retrieved $r_{e,i}$ (30.6 μm) and large uncertainty (σ = 11.0 μm) in this parameter. Therefore, it is hard to draw any significant conclusions about the ice particle size in the mixed-phase clouds in Figure 9.7.

The data collected during SHEBA spanned across the winter to early summer, and thus it is possible to look for any changes in the cloud properties that are associated with the changing seasons. Cloud optical depth, ice fraction, and cloud temperature distributions as a function of month are presented in Figure 9.8. The winter months have the coldest and thinnest clouds, and the clouds tend to become thicker and warmer in the spring. Significant numbers of liquid-phase and mixed-phase clouds exist throughout the winter, making up well over half of the clouds from January through May. Surprisingly, the distribution of the ice fraction is relatively unchanged from January through May, even though the clouds are becoming increasingly warmer. It should be noted that there are no clouds warmer than 0 C in this data set, even in May.

The distribution of effective particle sizes in liquid-only (f_i < 20%) and ice-only (f_i > 80%) clouds is shown in Figure 9.9. The monthly histograms of $r_{e,i}$ show considerable variability, especially for large particle sizes, as a function of month, but there no discernable

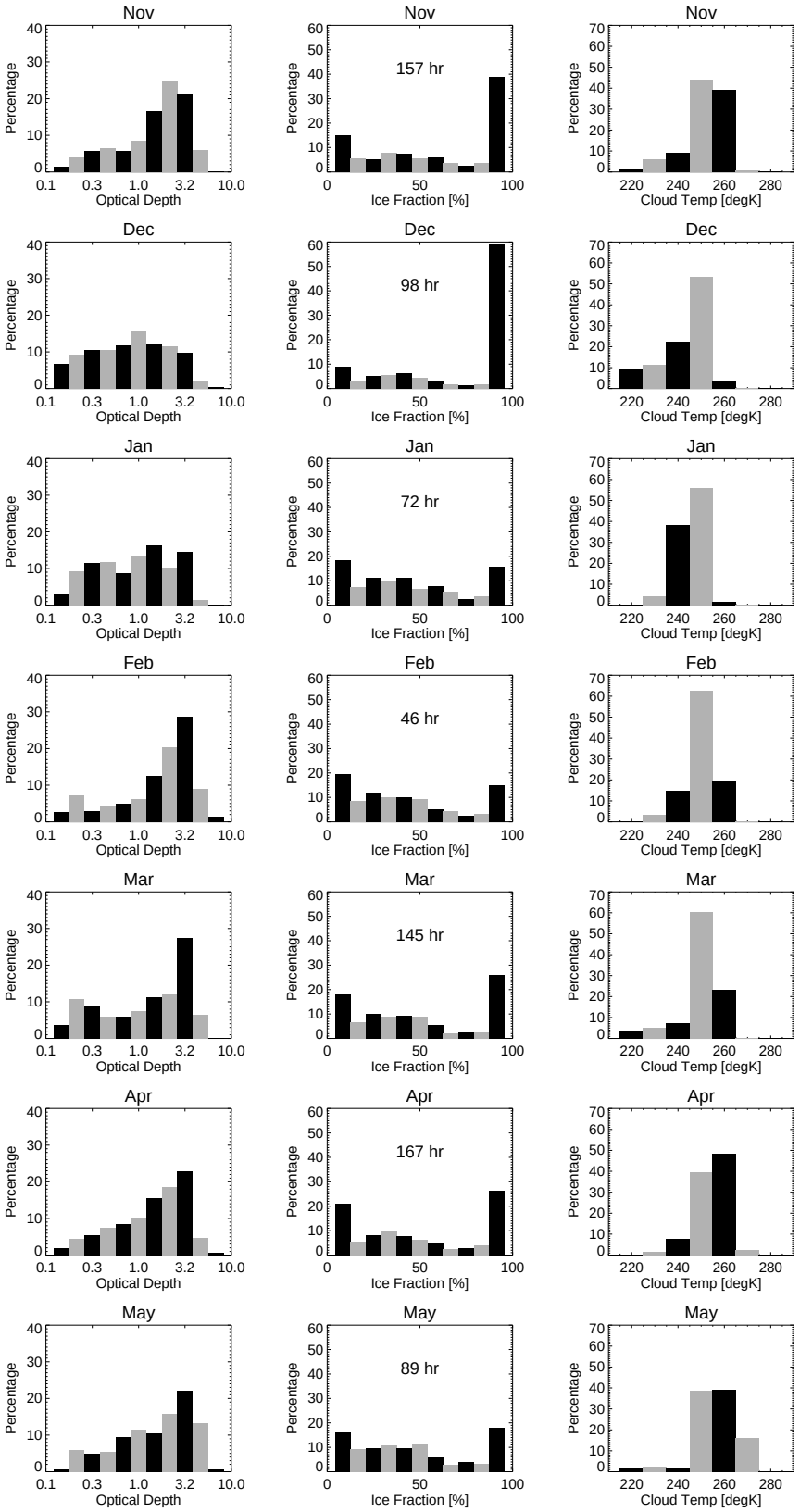

Figure 9.8: Optical depth, ice fraction, and cloud temperature distributions per month during SHEBA.

pattern in the variability. The distribution of $r_{e,w}$ shows that the mode of the distribution is approximately 10 μm in the winter months, and shifts to 7 μm by May. The mode value of approximately 7 μm in May agrees well with April-July mean $r_{e,w}$ value at SHEBA reported by Shupe et al. (2001) and the average May 2000 value at the ARM NSA site (Dong and Mace 2003). The decrease in droplet size from the winter to spring is most likely associated with the increase in anthropogenic aerosols advected to the Arctic from the mid-latitudes (Barrie and Hoff 1986, Sirois and Barrie 1999). Future analysis of the NSA data should indicate how the $r_{e,w}$ changes through the autumn transition season, but the Dong and

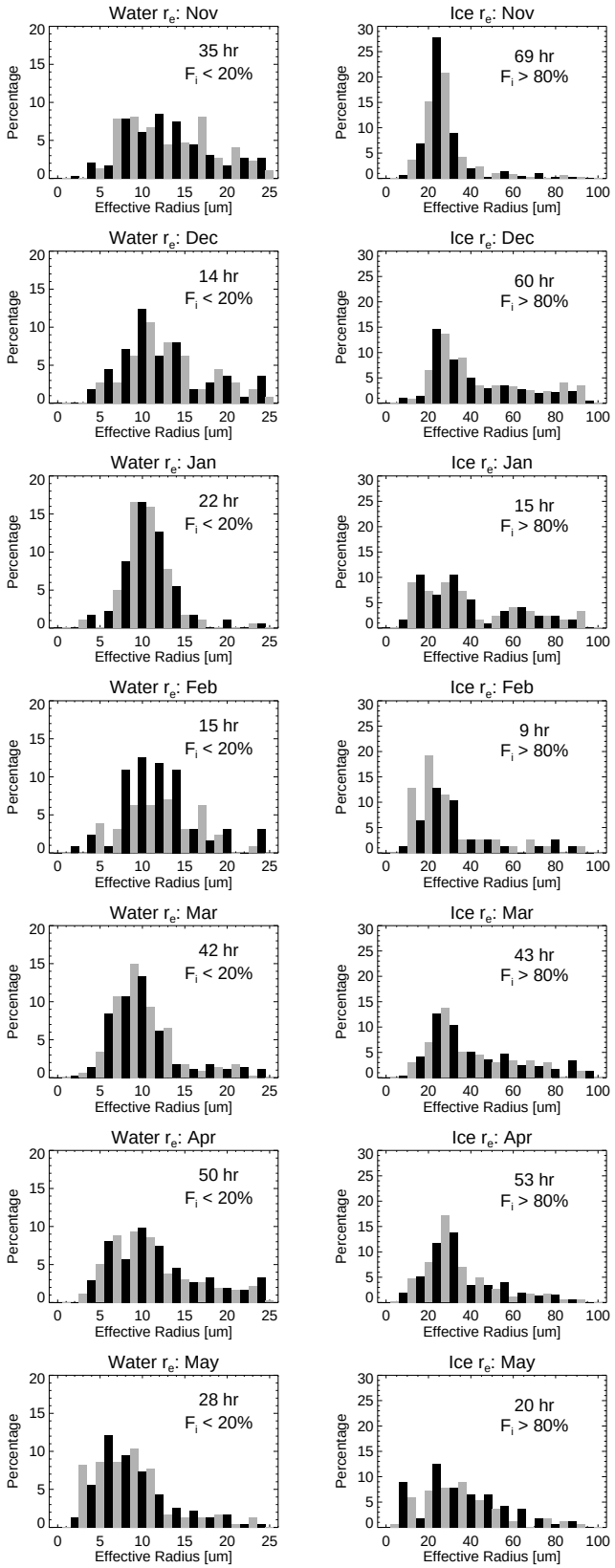

Figure 9.9: Water droplet and ice particle effective radii per month for single-phase clouds as SHEBA.

Mace (2003) results indicate that $r_{e,w}$ increases from approximately 7 μm in May to a maximum of 13 μm in July and then decreases to 11 μm in September. Assuming that the November 1997 – May 1998 SHEBA results from the AERI and the May – September 2000 results from Dong and Mace are consistent (i.e., the cloud properties for each year and site are similar and the two methods yield consistent results relative to each other), this suggests that there may be no noticeable change in $r_{e,w}$ in the autumn.

The retrieved size distributions of the water and ice particles in mixed-phase clouds for November through May is given in Figure 9.10. As indicated earlier, the retrieved ice particle sizes are somewhat suspect due to the significant uncertainty in this parameter when the optical depth is large. However, there are quite a few more optically thin mixed-phase clouds in November-February than in the spring months, and perhaps consequently, there are more larger ice particles in the mixed-phase clouds in these months than in the spring. The mode of $r_{e,w}$ is less variable from winter to spring in the mixed-phase clouds (Figure 9.10) than in the liquid-only clouds (Figure 9.9), although the peak in the distribution does appear to have shifted from approximately 8 μm in January and February to 7 μm in March, April, and May. This apparent shift, which may be related to the change in the aerosol loading from winter to spring, may not be statistically significant due to the fewer samples of mixed-phase clouds in January and February as opposed to the springtime period. The multi-year data set at the NSA site should provide the statistics needed to determine if the mixed-phase clouds do indeed respond to transitional-season aerosol loading.

Statistics of cloud properties from November 1997 – May 1998 from the SHEBA experiment have been used to test the sensitivity of mixed-phase parameterizations in climate

models. The GENESIS global climate model (Thompson and Pollard 1997, Vavrus 2003), which is used by researchers in the Center for Climatic Research at the University of Wisconsin - Madison, uses a parameterization where the cloud is determined to be liquid when its temperature (T_c) > –5 C, ice when T_c < –15 C, and mixed-phase with a linear ice fraction

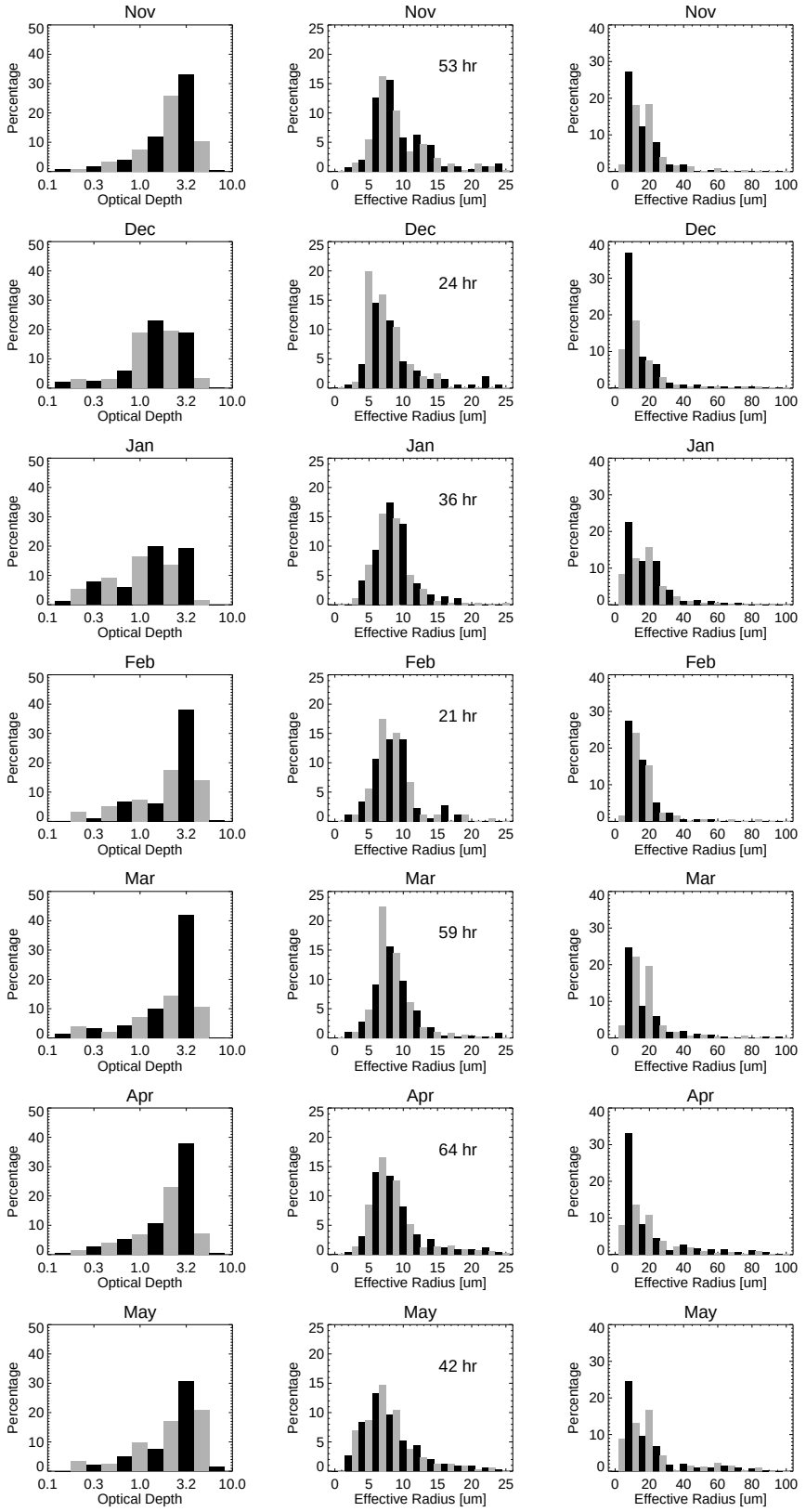

Figure 9.10: Distributions of optical depth and effective size of the water and ice particles for mixed-phase clouds during SHEBA.

for intermediate temperatures. The model can be run with either a fully-coupled atmospheric and mixed-layer ocean model or with the atmospheric model decoupled; keeping them coupled results in more realistic simulation but also requires long integration times to achieve stability. Changing the temperature threshold between the ice and mixed-phase regimes in GENESIS produces markedly different climates. For example, the GENESIS model was modified to use the temperature thresholds in the CCM3 for cloud phase determination (ice clouds for temperatures less than –30 C, water clouds for temperatures greater than –10 C, and mixed-phase clouds in between). The differences between the baseline GENESIS run and the modified GENESIS run show significant differences in both surface temperature and cloud fraction in the Arctic (Figure 9.11). Gregory and Morris (1996) also demonstrated that changing the temperature thresholds associated with cloud phase leads to significant changes in cloud water and zonal mean albedo.

The cloud phase parameterization in the GENESIS model was replaced with a stochastic routine that randomly assigned the cloud phase as a function of cloud temperature for clouds above 70°N. This routine randomly selected the cloud's phase based upon the probability density functions (PDFs) created from the data in Figure 9.6. However, the difference between the baseline GENESIS run and the run with the stochastic cloud phase "parameterization" was almost negligible (S. Vavrus, personal communication, 2003). The most likely reason is that there was no correlation between the phase of a cloud for a particular time step in the model with the next time step. Therefore, incorporation of autocorrelation functions of cloud properties, which can be determined from longer time-series such as the NSA data set, in addition to the cloud phase PDFs may produce significantly different results from the baseline run.

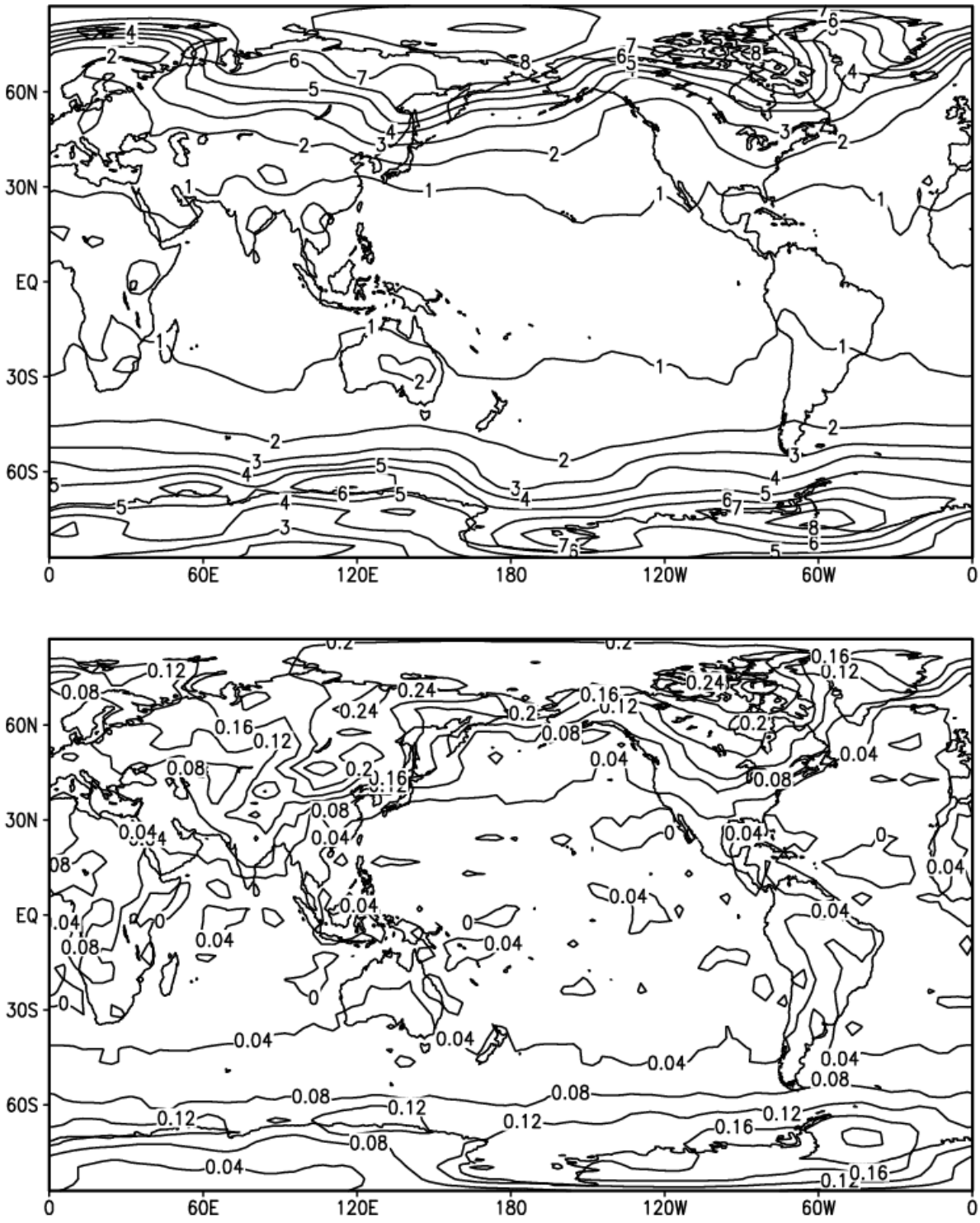

Figure 9.11: Change in surface temperature (top) and cloud fraction (bottom) between the baseline GENESIS run and the run that used CCM3 cloud phase threshold values.

9.1. Excursion: Temperature dependence of liquid water absorption in the microwave

The temperature dependence of the liquid water absorption in the microwave, especially in clouds with temperatures below 0 C, is not well known due to the inherent difficulties of creating supercooled liquid water droplets in a laboratory. Westwater et al. (2001) have shown that up to 30% differences exist between different liquid water absorption models in the microwave, and that using the Liebe et al. (1991) model yields better agreement with in situ observations in the Arctic during FIRE-ACE. Liquid water absorption has no temperature dependence in the infrared. Therefore, it is possible to use collocated LWP observations by the AERI and MWR to characterize and improve the temperature dependence in microwave liquid water absorption models.

The AERI retrievals were run in single-phase mode (to reduce the uncertainties in the retrieved parameters) on 10 days during SHEBA (Table 9.1) where the clouds were primarily liquid water (as determined by the lidar and ice fraction retrieved from the full AERI retrievals). As indicated in Chapter 8, a two-channel optimal estimation physical retrieval was developed using the Rosenkranz (1998) oxygen and water vapor absorption models and the Liebe et al. (1991) liquid water absorption model. The 1-σ noise estimates in the MWR observations was assumed to be 0.2 K in each channel, which was also assumed to be uncorrelated between the channels. The LWP for the MWR and AERI algorithms for these days were then compared (Figure 9.12). It should be noted that the MWR-retrieved LWP values during FIRE-ACE were larger than in situ observations made by aircraft, sometimes by as much as a factor of 2, even when the Liebe91 liquid water absorption model is used (Curry

et al. 2000, Westwater et al. 2001). The data from these 10 days fell into two general classifications: data where the cloud temperature was approximately -8 C and data where the cloud temperature was between -25 and –20 C. Linear regression lines were fit on the LWP scatter plot (Figure 9.12a) for the two cloud temperature clusters, but the difference in the slope of the lines is not statistically significant. The AERI LWP retrievals are significantly lower than the MWR values, which agrees qualitatively with the aircraft observations presented in Figure 10 of Westwater et al. (2001). Figure 9.12b shows a trend in the ratio of the LWP as a function of temperature. The large uncertainty is dictated by the large uncertainty in the MWR results at low LWP, and restricting the analysis to a range where both the MWR and the AERI have the better signal-to-noise (i.e., for LWP between 30 and 50 g m^{-2}) results in a better fit. The regression line should be close to unity at 0 degrees, if the microwave absorption models are accurate at this temperature. However, Westwater et al. (2001) have shown that significant differences exist between the different microwave liquid water absorption models at temperatures as large as 10 C. Extrapolating the linear fit to the 30-50 g m^{-2} data in Figure 9.12b to warmer temperatures shows that the ratio of AERI to MWR LWP is 1 at 12 C. Therefore, the infrared data appear to be consistent with microwave data at warmer (> 10 C) temperatures. There is a significant amount of scatter in the LWP ratios and thus a large degree of uncertainty in the fitted regression line. These results suggest that the liquid water absorption coefficient is actually larger than the values used in any of the three popular microwave absorption models for temperatures less than 10 C. However, more data from both the AERI and MWR over the entire temperature range would be needed to accurately characterize the temperature dependence of the liquid absorption.

Table 9.1: Days during SHEBA when the retrieval was run in a single-phase liquid mode for comparison with the MWR.

5 March	1 May
30 March	2 May
5 April	8 May
26 April	15 May
27 April	19 May

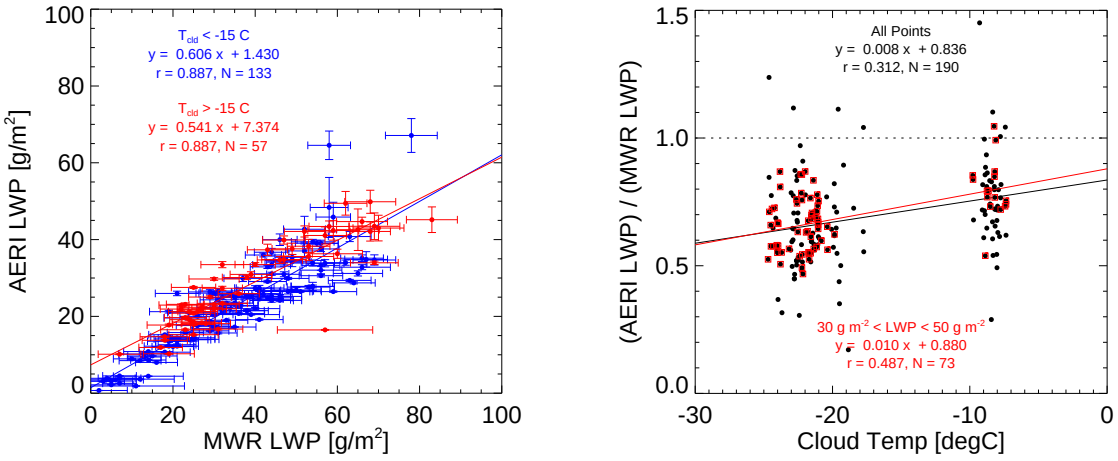

A

Figure 9.12: A: Scatterplot of LWP from the physical MWR retrieval (using the Liebe91 liquid water absorption model) and the AERI retrieved values. B: Ratio of AERI LWP to MWR LWP as a function of cloud temperature. Data in these figures are from clouds that were predominately liquid water.

Chapter 10

10. Summary and Conclusions

The three objectives of this study outlined in Chapter 2 were accomplished. The phase of Arctic clouds, provided that the optical depth at 900 cm^{-1} is less than 5, can be determined from ground-based high-spectral-resolution infrared observations, as long as those observations include measurements in both the 8-13 μm and 17-25 μm regions. A threshold-based phase determination algorithm was developed and applied to data collected during the SHEBA experiment. Simulated data, case studies, and comparisons with a polarization sensitive lidar over the SHEBA campaign were used to validate this algorithm, demonstrating the ability to ascertain phase from the AERI observations. A paper describing this algorithm was recently published (Turner et al. 2003c).

A physical retrieval algorithm, which uses the optimal estimation approach, was developed to retrieve cloud optical depth, ice fraction, liquid and ice water paths, and the effective radius of the water droplets and ice particles from the AERI observations. Simulated data and case studies were used to characterize this retrieval algorithm. Excellent agreement in liquid water path and effective radius of the water droplets was demonstrated for a liquid-only cloud, and good agreement was found in the retrieved ice water path for ice clouds. These studies demonstrated that the algorithm is most sensitive to errors in the PWV and cloud temperature. The retrieved ice fraction is slightly biased towards mixed-phase clouds in many cases because of the uncertainty in the 17-25 μm observations, which results from the uncertainty in the PWV. The retrieved ice fraction also demonstrates sensitivity to the habit

of the ice particles. This sensitivity is manifest primarily in the retrieved ice fraction, as the retrieved optical depth and effective radius of the ice particles is relatively insensitive to the habit (provided the cloud's phase is correctly determined). However, even though the optical depth and size of the ice particles are insensitive to the habit used in the retrieval, the use of different ice habit distributions resulted in significantly different ice water path values.

Cloud microphysical properties were retrieved from 7 months of data collected at SHEBA from November 1997 through May 1998. The cloud was mixed-phase approximately 50% of the time during this period. Distributions of the retrieved optical depth as a function of ice fraction showed that many of the mixed-phase clouds have large infrared optical depths (i.e., approaching the range where the infrared emissivity is 1), while there are many more examples of optically thin liquid-only and ice-only clouds. Analysis of the results as a function of cloud temperature shows that significant numbers of mixed-phase and liquid-only clouds exist at temperatures below 250 K, and that there is no clear relationship between cloud temperature and ice fraction. The distribution of effective radius of the water droplets in both liquid-only and mixed-phase clouds shows a well-defined single-mode distribution, with the mode values being approximately 10 μm and 7 μm, respectively. The smaller droplet size in the mixed-phase clouds may be due to the preferential freezing of the larger liquid water drops, which effectively removes them from the size distribution. The mode value for the liquid-only clouds shows significant seasonal dependence, shifting from larger values of 10 μm in the winter to 7 μm in the spring. One hypothesis is that this shift in particle size is caused by the increase in the advection of aerosols from the mid-latitudes in the spring resulting in higher concentrations of cloud condensation nuclei. The mode radius for the liquid water droplets in mixed-phase clouds shows a slight sensitivity to season,

shifting from mode values around 8 μm in the winter to 7 μm in the spring. This shift to smaller sizes is also most likely associated with the seasonal changes in aerosols. The effective size of the ice crystals in ice-only clouds shows a mode value near 25 μm with a significant number of samples with larger particle sizes. There is no obvious trend in the monthly distributions of crystal size in the ice-only clouds. The sizes of the ice crystals in mixed-phase clouds has a much smaller effective radius (order of 10 μm), which is puzzling since one might expect a few ice crystals (their number is typically restricted due to the scarcity of ice nuclei in Arctic clouds) to grow quickly in the presence of supercooled liquid water. Simulations have shown that the physical retrieval is able to accurately retrieve particle size of both the water and ice components when the infrared optical depth isn't too large; however, most mixed-phase clouds encountered during SHEBA had large optical depths. Therefore, the small ice particle size in mixed-phase clouds is most likely a limitation of the retrieval algorithm in these optically thick clouds.

This study has resulted in a promising new development in cloud retrieval theory, as there are very limited ways to observe microphysical properties in mixed-phase clouds. This algorithm will provide data that will help understand the role Arctic clouds play in the global climate. For example, Wang and Key (2003) have claimed that there are significant trends in the surface temperature, cloud fraction, and PWV for most seasons in the Arctic, as deduced from a 20-year analysis of Advanced Very High Resolution Radiometer (AVHRR) satellite data. Validation of the cloud properties retrieved from the AVHRR, as well as other satellites, is required to truly understand the uncertainties in the satellite results and the inferences drawn from them. Additionally, Lindzen (1997) and Schneider et al. (1999) have shown that the changes in the vertical distribution of the water vapor is critical to climate

change, both for direct forcing and indirect forcing (via cloud modification) points of view. Therefore, it is important to analyze both the clouds and the thermodynamic structure of the Arctic atmosphere simultaneously to properly understand any long-term changes that may be occurring.

The SHEBA results provide some interesting insight into Arctic cloud properties, although the data coverage is less than 1 year. The ARM NSA site offers a possible source of long-term data that could be used to address long-term trends. While a single site may not be representative of the entire Arctic, it provides a critical validation source for satellites, which provide the global view. However, radiosondes are launched infrequently at the NSA site (once per day during the weekdays), and atmospheric state information is required for retrieving cloud properties from the AERI. The AERI observations at the NSA site can provide the needed observations of thermodynamic structure (e.g., Smith et al. 1993a, Feltz et al. 1998, Smith et al. 1999) and cloud properties (this work). However, an integrated approach is required, as the cloud properties (in particular, the cloud emissivity spectrum) need to be determined for accurate retrieval of the thermodynamic profiles.

The next step to improve the retrieval is to simultaneously retrieve both the cloud microphysical properties and PWV. Errors in the PWV lead to significant uncertainties in the cloud property retrievals, and thus retrieving PWV directly should decrease the uncertainty in the retrievals related to this parameter. The recent improvements to the water vapor continuum model in the infrared (Turner et al. 2003b) allow the retrieval of PWV from AERI observations to be done with lower uncertainty. Incorporating the 23.8 and 31.4 GHz brightness temperatures observed by the microwave radiometer into the algorithm will also aid in the retrieval of PWV, as well as reducing the uncertainty in the liquid water component

of clouds as the optical depth gets large. However, before the MWR observations are incorporated into the algorithm, the discrepancy between the AERI and MWR retrieved liquid water path data, which is most likely due to errors in the temperature dependence of the liquid water absorption, must be improved.

Another improvement is to retrieve simultaneously profiles of water vapor, temperature, and cloud properties using an integrated approach. The current approach to retrieve water vapor and temperature profiles from the AERI uses an onion-peeling approach (Smith et al. 1999), which does not readily lend itself to the calculation of uncertainties in the retrieved parameters. Furthermore, cloud properties are required to retrieve thermodynamic profiles between the surface and the cloud. By incorporating the retrieval of profiles of water vapor and temperature with cloud properties into a single retrieval algorithm, the results would be radiometrically consistent and provide the unified data set needed to address the connection between the atmospheric state and clouds.

Clouds play a critical role in the Arctic climate system, and hence in the global climate system. The interaction among the clouds, the over and underlying atmosphere, and the surface are more complex and more uncertain in the Arctic than in mid-latitude and tropical locations. This is due primarily to a lack of observations of Arctic clouds. To complicate matters, a large fraction of the clouds are mixed-phase (the analysis in this thesis suggests approximately 50%), which are significantly more difficult to observe quantitatively and to model. The AERI retrievals developed in this thesis will provide a critical data set from the long-term ARM NSA record. The AERI retrievals will be used in conjunction with the other ARM observation and collocated NOAA Climate Monitoring and Diagnostics Laboratory measurements of aerosol and trace gas amounts to understand the role of aerosols and

boundary layer Arctic stratus clouds, and the internal physical processes of Arctic clouds, and the interactions of the cloud layer and the surface. In addition, the AERI observations are an important component of the upcoming Mixed-Phase Arctic Clouds Experiment (M-PACE), a NSF and ARM funded IOP, which is scheduled for October 2004. The major objective of this experiment is to "*collect the focused set of observations needed to advance our understanding of the dynamical and physical processes in mixed-phase clouds, including the cloud microphysical processes and radiative transfer through clouds*" with the ultimate goal of producing a better understanding of mixed-phase stratus clouds in the Arctic (Verlinde 2003). The research presented in this thesis is timely, pertinent, and important to this goal.

Appendix A: Jacobian formulations in S_ε determination

In Chapter 5, the formulation for cloud emissivity was derived for the case of downwelling radiation shown in equation (5.9). The emissivity can be stated as in equation (7.5), and thus the standard error propagation techniques yield the error as in equation (7.6). This appendix details how the individual Jacobians in equation (7.7) were derived for each component.

To calculate emissivity from downwelling radiation, we need to compute both the clear sky radiance **R** and the surface-to-cloud transmittance **J** from the LBLRTM. Therefore, if we let the LBLRTM be designated by the operator *f*, then we can write

$$f(\mathbf{P}) = \begin{pmatrix} \mathbf{R} \\ \mathbf{J} \end{pmatrix}_{2\mathrm{N}x1} \tag{A.1}$$

where **P** is the PWV. Note that the size of the matrix is indicated in the lower right, where N is the number of microwindows. Therefore, the Jacobian $\mathbf{K}_{\varepsilon\mathbf{f}}$ can be written as

$$\mathbf{K}_{\varepsilon f} = \left(\mathbf{K}_{\varepsilon R}, \mathbf{K}_{\varepsilon J}\right)_{\mathrm{N}x2\mathrm{N}} \tag{A.2}$$

where

$$\left(\mathbf{K}_{\varepsilon R}\right)_{ii} = \frac{\partial \boldsymbol{\varepsilon}_i}{\partial \mathbf{R}_i} = \frac{-1}{\mathbf{J}_i \mathbf{B}_i} \tag{A.3}$$

and

$$\left(\mathbf{K}_{\varepsilon J}\right)_{ii} = \frac{\partial \boldsymbol{\varepsilon}_i}{\partial \mathbf{J}_i} = \frac{\mathbf{I}_i - \mathbf{R}_i}{\mathbf{B}_i \mathbf{J}_i^2}. \tag{A.4}$$

Note that $\mathbf{K}_{\varepsilon R}$ and $\mathbf{K}_{\varepsilon J}$ are NxN diagonal matrices, since emissivity at a given wavelength is not dependent on data from a different wavelength. Now $\mathbf{K}_{fP}$ is written as

$$\mathbf{K}_{fP} = \begin{pmatrix} \mathbf{K}_{RP} \\ \mathbf{K}_{JP} \end{pmatrix}_{2\mathrm{Nx1}} \tag{A.5}$$

where

$$\left(\mathbf{K}_{RP}\right)_i = \frac{\partial \mathbf{R}_i}{\partial \mathbf{P}} \tag{A.6}$$

and

$$\left(\mathbf{K}_{JP}\right)_{ii} = \frac{\partial \mathbf{J}_i}{\partial \mathbf{P}} \tag{A.7}$$

are Nx1 matrices that are found by perturbation.

The first two components of the error equation are much simpler than the third component that was just explained. The Jacobian $\mathbf{K}_{\varepsilon I}$ is a NxN diagonal matrix that is easily computed as

$$\left(\mathbf{K}_{\varepsilon I}\right)_{ii} = \frac{\partial \boldsymbol{\varepsilon}_i}{\partial \mathbf{I}_i} = \frac{1}{\mathbf{J}_i \mathbf{B}_i}. \tag{A.8}$$

The Jacobian $\mathbf{K}_{\varepsilon B}$ is also a NxN diagonal matrix with elements

$$\left(\mathbf{K}_{\varepsilon B}\right)_{ii} = \frac{\partial \boldsymbol{\varepsilon}_i}{\partial \mathbf{B}_i} = \frac{-\left(\mathbf{I}_i - \mathbf{R}_i\right)}{\mathbf{J}_i \mathbf{B}_i^2} \tag{A.9}$$

and the Nx1 matrix

$$\left(\mathbf{K}_{BT}\right)_i = \frac{\partial \mathbf{B}_i}{\partial \mathbf{T}} \tag{A.10}$$

is found by perturbation.

Appendix B: Cloud parameters used in the simulations

Run	T	F	W	I
4.0	0.2	1.00	-1.00	21.50
4.1	0.5	1.00	-1.00	21.50
4.2	1.0	1.00	-1.00	21.50
4.3	2.0	1.00	-1.00	21.50
4.4	4.0	1.00	-1.00	21.50
5.0	0.2	0.00	7.50	-1.00
5.1	0.5	0.00	7.50	-1.00
5.2	1.0	0.00	7.50	-1.00
5.3	2.0	0.00	7.50	-1.00
5.4	4.0	0.00	7.50	-1.00
6.0	0.2	0.50	7.50	21.50
6.1	0.5	0.50	7.50	21.50
6.2	1.0	0.50	7.50	21.50
6.3	2.0	0.50	7.50	21.50
6.4	4.0	0.50	7.50	21.50
10.0	0.2	0.00	7.50	-1.00
10.1	0.2	0.00	9.50	-1.00
10.2	0.2	0.00	11.50	-1.00
10.3	0.2	0.00	5.50	-1.00
11.0	0.5	0.00	7.50	-1.00
11.1	0.5	0.00	9.50	-1.00
11.2	0.5	0.00	11.50	-1.00
11.3	0.5	0.00	5.50	-1.00
12.0	1.0	0.00	7.50	-1.00
12.1	1.0	0.00	9.50	-1.00
12.2	1.0	0.00	11.50	-1.00
12.3	1.0	0.00	5.50	-1.00
13.0	2.0	0.00	7.50	-1.00
13.1	2.0	0.00	9.50	-1.00
13.2	2.0	0.00	11.50	-1.00
13.3	2.0	0.00	5.50	-1.00
14.0	4.0	0.00	7.50	-1.00
14.1	4.0	0.00	9.50	-1.00
14.2	4.0	0.00	11.50	-1.00
14.3	4.0	0.00	5.50	-1.00
15.0	0.2	1.00	-1.00	21.50
15.1	0.2	1.00	-1.00	17.50
15.2	0.2	1.00	-1.00	25.50
15.3	0.2	1.00	-1.00	13.50
16.0	0.5	1.00	-1.00	21.50
16.1	0.5	1.00	-1.00	17.50
16.2	0.5	1.00	-1.00	25.50
16.3	0.5	1.00	-1.00	13.50
17.0	1.0	1.00	-1.00	21.50
17.1	1.0	1.00	-1.00	17.50
17.2	1.0	1.00	-1.00	25.50
17.3	1.0	1.00	-1.00	13.50
18.0	2.0	1.00	-1.00	21.50
18.1	2.0	1.00	-1.00	17.50
18.2	2.0	1.00	-1.00	25.50
18.3	2.0	1.00	-1.00	13.50
19.0	4.0	1.00	-1.00	21.50
19.1	4.0	1.00	-1.00	17.50
19.2	4.0	1.00	-1.00	25.50
19.3	4.0	1.00	-1.00	13.50
20.0	0.2	1.00	7.50	21.50
20.1	0.2	0.80	7.50	21.50
20.2	0.2	0.50	7.50	21.50
20.3	0.2	0.20	7.50	21.50
20.4	0.2	0.00	7.50	21.50
21.0	0.5	1.00	7.50	21.50
21.1	0.5	0.80	7.50	21.50
21.2	0.5	0.50	7.50	21.50
21.3	0.5	0.20	7.50	21.50
21.4	0.5	0.00	7.50	21.50
22.0	1.0	1.00	7.50	21.50
22.1	1.0	0.80	7.50	21.50
22.2	1.0	0.50	7.50	21.50
22.3	1.0	0.20	7.50	21.50
22.4	1.0	0.00	7.50	21.50
23.0	2.0	1.00	7.50	21.50
23.1	2.0	0.80	7.50	21.50
23.2	2.0	0.50	7.50	21.50
23.3	2.0	0.20	7.50	21.50
23.4	2.0	0.00	7.50	21.50
24.0	4.0	1.00	7.50	21.50
24.1	4.0	0.80	7.50	21.50
24.2	4.0	0.50	7.50	21.50
24.3	4.0	0.20	7.50	21.50
24.4	4.0	0.00	7.50	21.50
30.0	0.2	1.00	-1.00	45.00
30.1	0.5	1.00	-1.00	45.00
30.2	1.0	1.00	-1.00	45.00
30.3	2.0	1.00	-1.00	45.00
30.4	4.0	1.00	-1.00	45.00
31.0	0.2	1.00	-1.00	70.00
31.1	0.5	1.00	-1.00	70.00
31.2	1.0	1.00	-1.00	70.00
31.3	2.0	1.00	-1.00	70.00
31.4	4.0	1.00	-1.00	70.00
32.0	3.0	0.30	10.00	40.00
32.1	5.0	0.30	10.00	40.00
32.2	7.0	0.30	10.00	40.00

T: Optical Depth; F: Ice Fraction;
W: Effective Radius for Water; I: Effective Radius for Ice

Appendix C: Results of simulations

Run	Tbar	Tsd	sTbar	Fbar	Fsd	sFbar	Wbar	Wsd	sWbar	Ibar	Isd	sIbar	Cvg
4.0	0.200	0.003	0.018	0.836	0.221	0.090	15.72	8.67	10.15	21.09	2.67	2.18	1.00
4.1	0.498	0.007	0.035	0.890	0.195	0.075	16.16	9.06	9.81	21.08	1.31	1.01	0.98
4.2	0.992	0.006	0.044	0.963	0.064	0.052	12.83	7.95	10.03	21.40	0.49	0.49	0.95
4.3	1.985	0.015	0.092	0.966	0.068	0.054	11.25	7.43	11.09	21.42	0.53	0.44	0.93
4.4	3.955	0.045	0.421	0.940	0.094	0.121	10.43	7.16	11.75	21.59	1.28	0.81	1.00
5.0	0.197	0.003	0.021	0.142	0.121	0.074	6.88	0.63	0.47	15.63	6.85	6.38	0.98
5.1	0.496	0.005	0.031	0.078	0.084	0.040	7.19	0.39	0.24	14.86	6.97	6.67	1.00
5.2	0.992	0.011	0.071	0.080	0.095	0.048	7.14	0.49	0.27	18.12	7.66	9.94	1.00
5.3	1.993	0.019	0.178	0.065	0.082	0.059	7.25	0.41	0.36	17.25	6.68	14.04	1.00
5.4	3.955	0.084	0.943	0.252	0.210	0.183	6.26	1.46	1.32	19.75	4.27	11.78	1.00
6.0	0.201	0.005	0.044	0.448	0.181	0.180	8.05	1.71	1.41	19.53	3.49	4.07	1.00
6.1	0.501	0.008	0.067	0.483	0.141	0.111	7.71	1.20	0.83	20.33	1.63	1.67	1.00
6.2	0.998	0.009	0.162	0.507	0.078	0.137	7.49	0.71	0.97	21.01	1.36	1.32	1.00
6.3	1.999	0.022	0.335	0.496	0.134	0.142	7.50	1.12	1.00	21.29	1.62	1.49	0.98
6.4	3.982	0.072	1.084	0.531	0.170	0.237	7.06	1.64	2.01	21.82	2.16	2.74	1.00
10.0	0.197	0.004	0.015	0.136	0.134	0.053	6.93	0.73	0.38	16.60	6.59	6.73	0.98
10.1	0.196	0.005	0.032	0.230	0.215	0.118	8.42	1.66	0.80	15.41	6.00	5.49	1.00
10.2	0.194	0.005	0.041	0.334	0.216	0.163	9.68	1.83	1.20	17.34	4.79	4.25	1.00
10.3	0.198	0.004	0.012	0.171	0.214	0.042	4.76	1.05	0.26	14.70	6.00	5.12	0.80
11.0	0.496	0.005	0.029	0.073	0.087	0.037	7.20	0.46	0.22	15.65	6.07	6.95	1.00
11.1	0.493	0.007	0.045	0.163	0.134	0.064	8.75	0.79	0.43	17.41	7.08	5.22	1.00
11.2	0.490	0.008	0.056	0.222	0.173	0.085	10.39	1.11	0.62	19.07	5.82	6.18	0.98
11.3	0.495	0.006	0.024	0.130	0.178	0.032	4.92	0.84	0.17	18.40	6.29	5.00	0.65
12.0	0.995	0.010	0.060	0.062	0.076	0.038	7.26	0.38	0.23	16.68	6.29	7.75	1.00
12.1	0.989	0.012	0.119	0.131	0.123	0.084	8.89	0.66	0.48	19.18	6.06	6.79	0.98
12.2	0.990	0.014	0.105	0.120	0.123	0.074	10.98	0.72	0.46	18.41	7.81	10.88	0.95
12.3	0.997	0.007	0.034	0.022	0.045	0.019	5.45	0.16	0.09	15.38	8.01	13.66	0.93
13.0	1.994	0.016	0.190	0.072	0.079	0.063	7.26	0.33	0.37	17.64	6.32	12.50	0.97
13.1	1.973	0.029	0.259	0.207	0.161	0.094	8.46	0.96	0.58	19.62	4.21	4.74	0.95
13.2	1.973	0.031	0.278	0.145	0.150	0.099	10.72	0.97	0.59	21.33	7.28	12.95	0.80
13.3	1.990	0.023	0.073	0.012	0.027	0.022	5.45	0.19	0.16	19.19	7.04	15.69	0.95
14.0	3.965	0.088	0.917	0.191	0.184	0.173	6.65	1.07	1.32	21.12	6.46	13.80	0.97
14.1	3.932	0.086	1.034	0.256	0.200	0.199	8.19	1.39	1.48	20.53	4.99	9.92	0.95
14.2	3.921	0.077	1.107	0.273	0.229	0.216	9.84	1.99	1.57	23.11	7.34	13.09	0.95
14.3	4.038	0.124	0.797	0.229	0.250	0.145	4.56	1.53	1.07	21.62	6.33	15.65	0.88
15.0	0.200	0.004	0.027	0.790	0.294	0.125	16.68	9.46	9.53	20.70	4.06	2.45	0.98
15.1	0.201	0.005	0.027	0.677	0.292	0.123	18.25	8.43	7.00	15.44	4.40	1.50	0.90
15.2	0.200	0.005	0.017	0.789	0.338	0.082	14.01	9.24	6.50	25.80	4.73	5.10	1.00
15.3	0.202	0.004	0.017	0.417	0.349	0.073	15.59	6.16	3.35	11.23	4.91	1.71	0.88
16.0	0.500	0.008	0.041	0.857	0.226	0.084	15.66	7.41	7.65	21.66	1.89	1.49	1.00
16.1	0.501	0.009	0.047	0.819	0.259	0.098	17.19	8.09	9.75	15.90	3.18	0.67	0.80
16.2	0.499	0.009	0.031	0.866	0.259	0.064	14.79	8.65	8.13	25.04	2.38	2.05	1.00
16.3	0.503	0.010	0.038	0.651	0.325	0.072	13.96	4.10	2.50	10.95	2.76	0.65	0.22
17.0	0.995	0.008	0.069	0.941	0.094	0.078	12.35	7.78	8.43	21.47	0.53	0.54	1.00
17.1	0.996	0.009	0.074	0.914	0.129	0.079	13.72	7.44	10.31	17.01	0.64	0.41	0.63
17.2	0.995	0.007	0.061	0.946	0.076	0.069	13.86	9.26	10.71	25.54	0.99	0.89	1.00
17.3	0.990	0.008	0.058	0.932	0.077	0.067	11.33	5.53	5.24	13.17	0.47	0.29	0.22

Run	Tbar	Tsd	sTbar	Fbar	Fsd	sFbar	Wbar	Wsd	sWbar	Ibar	Isd	sIbar	Cvg
18.0	1.989	0.015	0.125	0.959	0.071	0.073	10.55	6.66	9.10	21.57	0.47	0.47	0.97
18.1	1.989	0.016	0.199	0.906	0.105	0.111	13.61	5.10	7.10	17.28	0.59	0.42	0.32
18.2	1.987	0.015	0.129	0.957	0.064	0.075	11.47	6.40	9.47	25.76	0.98	0.81	0.97
18.3	1.979	0.006	0.141	0.944	0.056	0.083	9.72	5.29	4.29	13.40	0.34	0.29	0.10
19.0	3.973	0.050	0.480	0.929	0.139	0.133	9.49	4.31	8.56	21.81	0.83	0.95	0.95
19.1	3.954	0.059	0.415	0.873	0.118	0.115	9.43	3.12	4.31	17.91	0.97	0.68	0.68
19.2	3.974	0.043	0.475	0.944	0.082	0.135	9.98	6.04	10.78	25.88	1.33	1.27	0.95
19.3	3.912	0.039	0.211	0.980	0.021	0.068	7.02	1.35	5.02	13.66	0.18	0.28	0.07
20.0	0.200	0.004	0.027	0.779	0.256	0.131	17.14	8.17	8.33	20.36	3.47	2.17	0.98
20.1	0.202	0.006	0.029	0.630	0.263	0.126	9.73	3.86	1.59	20.33	3.58	3.61	1.00
20.2	0.202	0.005	0.039	0.405	0.190	0.153	8.46	1.65	1.20	19.11	4.81	3.70	1.00
20.3	0.200	0.005	0.026	0.244	0.206	0.096	7.30	1.53	0.61	17.55	6.70	5.27	1.00
20.4	0.197	0.003	0.019	0.138	0.148	0.067	6.88	0.88	0.41	13.41	6.99	5.52	0.95
21.0	0.498	0.007	0.035	0.883	0.195	0.074	15.60	7.97	8.33	20.93	1.45	0.88	0.97
21.1	0.500	0.005	0.055	0.748	0.122	0.109	8.24	2.34	1.35	20.85	1.34	1.08	1.00
21.2	0.502	0.007	0.080	0.461	0.110	0.130	7.97	1.00	0.94	20.12	1.50	1.63	1.00
21.3	0.499	0.009	0.062	0.226	0.153	0.091	7.38	0.96	0.55	18.85	4.00	4.65	1.00
21.4	0.496	0.006	0.030	0.091	0.110	0.039	7.11	0.58	0.25	15.19	7.36	6.00	0.98
22.0	0.992	0.008	0.050	0.960	0.075	0.058	11.44	8.42	9.98	21.37	0.49	0.51	0.98
22.1	0.997	0.010	0.117	0.769	0.100	0.119	7.81	2.14	1.50	21.10	0.92	0.76	0.97
22.2	1.002	0.013	0.155	0.472	0.128	0.128	7.79	1.05	0.88	20.44	2.39	1.49	0.98
22.3	1.000	0.013	0.129	0.200	0.113	0.092	7.55	0.65	0.52	20.17	3.35	4.03	1.00
22.4	0.995	0.007	0.058	0.054	0.061	0.037	7.28	0.27	0.20	15.67	6.23	8.63	1.00
23.0	1.986	0.016	0.117	0.960	0.074	0.069	11.63	7.24	8.83	21.35	0.46	0.47	0.95
23.1	1.997	0.018	0.309	0.753	0.096	0.155	8.20	1.74	1.78	21.35	0.97	0.81	0.97
23.2	2.000	0.022	0.344	0.479	0.120	0.144	7.67	0.92	1.04	21.08	1.39	1.38	0.97
23.3	1.997	0.025	0.313	0.233	0.127	0.115	7.35	0.75	0.67	21.14	4.79	5.65	1.00
23.4	1.993	0.020	0.134	0.048	0.074	0.042	7.31	0.37	0.27	16.55	7.04	17.77	0.98
24.0	3.962	0.039	0.414	0.933	0.114	0.116	10.42	5.98	12.65	21.57	1.13	0.78	0.97
24.1	3.999	0.068	1.093	0.691	0.165	0.258	8.67	2.47	3.15	21.39	1.92	1.72	0.98
24.2	3.998	0.080	1.194	0.514	0.202	0.252	7.22	2.06	2.09	21.11	2.40	3.18	0.97
24.3	3.998	0.083	1.182	0.283	0.188	0.224	7.16	1.25	1.68	21.14	4.95	9.12	1.00
24.4	3.976	0.110	1.024	0.188	0.160	0.188	6.75	0.97	1.36	18.38	4.70	13.48	0.93
30.0	0.200	0.006	0.010	0.595	0.455	0.048	17.07	8.50	6.76	39.78	13.87	14.81	1.00
30.1	0.502	0.012	0.021	0.751	0.391	0.043	13.98	8.66	6.70	48.30	14.99	13.49	1.00
30.2	0.994	0.009	0.029	0.962	0.132	0.037	9.92	7.14	7.72	46.21	6.97	5.58	1.00
30.3	1.985	0.032	0.084	0.965	0.087	0.051	10.49	6.36	11.37	45.64	6.71	5.05	1.00
30.4	3.933	0.162	0.288	0.944	0.130	0.084	9.25	6.51	14.76	45.92	12.07	8.39	1.00
31.0	0.198	0.003	0.018	0.721	0.385	0.088	16.68	8.99	8.40	59.19	23.69	26.05	1.00
31.1	0.496	0.006	0.020	0.838	0.322	0.045	15.37	8.55	8.33	67.91	21.51	17.08	1.00
31.2	0.991	0.013	0.028	0.946	0.183	0.036	11.62	8.24	10.36	68.56	13.86	11.15	1.00
31.3	1.978	0.024	0.070	0.980	0.042	0.044	11.09	7.79	13.11	66.36	11.99	9.39	1.00
31.4	3.799	0.251	0.277	0.930	0.159	0.083	9.66	5.07	15.16	49.72	15.27	7.79	1.00
32.0	2.980	0.068	0.604	0.341	0.176	0.158	9.70	1.44	1.14	30.60	8.52	10.99	1.00
32.1	4.896	0.128	1.544	0.502	0.169	0.264	8.34	1.92	2.50	27.65	6.90	9.31	1.00
32.2	6.902	0.212	3.631	0.524	0.165	0.450	8.32	2.05	4.75	25.48	7.56	11.73	1.00

*X*bar: Mean value of *X*; *X*sd: Standard deviation of *X*; s*X*bar: Mean 1-sigma error bar of *X*; T: Optical Depth; F: Ice Fraction; W: Effective Radius of Water Droplets; I: Effective Radius of Ice Particles; Cnv: Convergence Fraction. Each run consisted of 60 samples.

References

Ackerman, S.A., W.L. Smith, J.D. Spinhirne, and H.E. Revercomb, 1990: The 27-28 October 1986 FIRE IFO cirrus case study: Spectral properties of cirrus clouds in the 8-12-μm window. *Mon. Wea. Rev.*, **118**, 2377-2388.

Ackerman, S.A., E.W. Eloranta, C.J. Grund, R.O. Knuteson, H.E. Revercomb, W.L. Smith, and D.P. Wylie, 1993: University of Wisconsin cirrus remote sensing pilot experiment. *Bull. Amer. Meteor. Soc.*, **74**, 1041-1049.

Ackerman, S.A., W.L. Smith, A.D. Collard, X.L. Ma, H.E. Revercomb, and R.O. Knuteson, 1995: Cirrus cloud properties derived from high spectral resolution infrared spectrometry during FIRE II. Part II: Aircraft results. *J. Atmos. Sci.*, **52**, 4246-4263.

Antikaninen, V., and A. Paukkunen, 1994: Studies on improving humidity measurements in radiosondes. *WMO Tech. Conf. on Instruments and Methods of Observation*, Geneva, Switzerland, WMO Rep. 57, 1-5.

Alvarez, R.J., W.L. Eberhard, J.M. Intrieri, C.J. Grund, and S.P. Sandberg, 1998: A depolarization and backscatter lidar for unattended operation in varied meteorological conditions. *Proc. 10th Symp. Meteor. Obs. Instrum.*, AMS, Boston, MA, 140-144.

Barrie, L.A., and R.M. Hoff, 1986: Five years of air chemistry observations in the Canadian Arctic. *Atmos. Environ.*, **19**, 1995-2010.

Baran, A.J., and S. Havemann, 1999: Rapid computation of the optical properties of hexagonal columns using complex angular momentum theory. *J. Quant. Spect. Rad. Trans.*, **63**, 499-519.

Baum, B.A., P.F. Soulen, K.I. Strabala, M.D. King, S.A. Ackerman, W.P. Menzel, and P. Yang, 2000: Remote sensing of cloud properties using MODIS airborne simulator imagery during SUCCESS. 2. Cloud thermodynamic phase. *J. Geophys. Res.*, **105**, 11781-11792.

Best, F.A., H.E. Revercomb, D.D. LaPorte, R.O. Knuteson, and W.L. Smith, 1997: Accurately calibrated airborne and ground-based Fourier transform spectrometers II: HIS and AERI calibration techniques, traceability, and testing. *Proc. Council for Optical Radiation Measurements (CORM) 1997 Annual Meeting*, National Institute of Standards and Technology (NIST), Gaithersburg, MD.

Bevington, P.R., and D.K. Robinson, 1992: *Data reduction and error analysis for the physical sciences, 2nd Edition.* McGraw Hill, Boston, MA, 328 pp.

Bohren, C.F., and D.R. Huffman, 1983: *Absorption and scattering of light by small particles.* Wiley and Sons, New York, 530 pp.

Brown, P.R.A., and P.N. Francis, 1995: Improved measurements of the ice water content in cirrus using a total-water probe. *J. Atmos. Oceanic Technol.*, **12**, 410-414.

Campbell, J.R., D.L. Hlavka, E.J. Welton, C.J. Flynn, D.D. Turner, J.D. Spinhirne, V.S. Scott, and I.H. Hwang, 2002: Full-time, eye-safe cloud and aerosol lidar observations at Atmospheric Radiation Measurement program sites: instruments and data processing. *J. Atmos. Oceanic Technol.*, **19**, 431-442.

Cess, R.D., and coauthors, 1990: Intercomparison and interpretation of climate feedback processes in 19 atmospheric general circulation models. *J. Geophys. Res.*, **95**, 16601-16615.

Chung, S., S. Ackerman, P.F. vanDelst, and W.P. Menzel, 2000: Model calculations and interferometer measurements of ice-cloud characteristics. *J. Appl. Meteor.*, **39**, 634-644.

Clothiaux, E.E., K.P. Moran, B.E. Martner, T.P. Ackerman, G.G. Mace, T. Uttal, J.H. Mather, K.B. Widener, M.A. Miller, and D.J. Rodriguez, 1999: The Atmospheric Radiation Measurement program cloud radars: Operational modes. *J. Atmos. Oceanic Technol.*, **16**, 819-827.

Clothiaux, E.E., T.P. Ackerman, G.G. Mace, K.P. Moran, R.T. Marchand, M.A. Miller, and B.E. Martner, 2000: Objective determination of cloud heights and radar reflectivities using a combination of active remote sensors at the ARM CART sites. *J. App. Meteor.*, **39**, 645-665.

Clough, S.A., F.X. Kneizys, and R.W. Davies, 1989: Line shape and the water vapor continuum. *Atmos. Res.*, **23**, 229-241.

Clough, S.A., M.J. Iacono, and J.L. Moncet, 1992: Line-by-line calculations of atmospheric fluxes and cooling rates: application to water vapor. *J. Geophys. Res.*, **97**, 15761-15785.

Clough, S.A., and M.J. Iacono, 1995: Line-by-line calculations of atmospheric fluxes and cooling rates: application to carbon dioxide, ozone, methane, nitrous oxide, and the halocarbons. *J. Geophys. Res.*, **100**, 16519-16535.

Collard, A.D., S.A. Ackerman, W.L. Smith, X. Ma, H.E. Revercomb, R.O. Knuteson, and S.-C. Lee, 1995: Cirrus cloud properties derived from high spectral resolution infrared spectrometry during FIRE II. Part III: Ground-based HIS results. *J. Atmos. Sci.*, **52**, 4264-4275.

Curry, J.A., F.G. Meyers, L.F. Radke, C.A. Brock, and E.E. Ebert, 1990: Occurrence and characteristics of lower tropospheric ice crystals in the Arctic. *Int. J. Climatol.*, **10**, 749-764.

Curry, J.A., W.B. Rossow, D. Randall, and J.L. Schramm, 1996: Overview of Arctic cloud and radiation characteristics. *J. Climate*, **9**, 1731-1764.

Curry, J.A., J.O. Pinto, T. Benner, and M. Tschudi, 1997: Evolution of the cloudy boundary layer during the autumnal freezing of the Beaufort Sea. *J. Geophys. Res.*, **102**, 13851-13860.

Curry, J.A., and coauthors: 2000: FIRE Arctic clouds experiment. *Bull. Amer. Meteor. Soc.*, **81**, 5-29.

Daniel, J.S., S. Solomon, R.W. Portmann, A.O. Langford, C.S. Eubank, E.G. Dutton, and W. Madeson, 2002: Cloud liquid water and ice measurements from spectrally resolved near-infrared observations: a new technique. *J. Geophys. Res.*, **107**, doi:10.1029/2001JD000688.

DeSlover, D.H., W.L. Smith, P.K. Piironen, and E.W. Eloranta, 1999: A methodology for measuring cirrus cloud visible-to-infrared spectral optical depth ratios. *J. Atmos. Oceanic Technol.*, **16**, 251-262.

Dong, X., G.G. Mace, P. Minnis, and D.F. Young, 2001: Arctic stratus cloud properties and their effect on the surface radiation budget: Selected cases from FIRE ACE. *J. Geophys. Res.*, **106**, 15297-15312.

Dong., X., and G.G. Mace, 2003: Arctic stratus cloud properties and radiative forcing derived from ground-based data collected at Barrow, Alaska. J. Climate, 16, 445-461.

Downing, H.D., and D. Williams, 1975: Optical constants of water in the infrared. *J. Geophys. Rev.*, **80**, 1656-1661.

Eberhard, W.L., 1995: Theory for dual-wavelength CO2 lidar method to distinguish ice, mixed-phase, and water clouds. *J. Atmos. Oceanic Technol.*, **12**, 130-140.

Ellingson, R.G., and Y. Fouquart, 1991: The intercomparison of radiation codes in climate models (ICRCCM): An overview. *J. Geophys. Res.*, **96**, 8925-8927.

Ellingson, R.G., J. Ellis, and S. Fels, 1991: The intercomparison of radiation codes in climate models (ICRCCM): Longwave results. *J. Geophys. Res.*, **96**, 8928-8953.

Ellingson, R.G., and W.J. Wiscombe, 1996: The spectral radiance experiment (SPECTRE): Project description and sample results. *Bull. Amer. Meteor. Soc.*, **77**, 1967-1985.

Feltz, W.F., W.L. Smith, R.O. Knuteson, H.E. Revercomb, H.B. Howell, and H. Woolf, 1998: Meteorological applications of temperature and water vapor retrievals from the ground-based Atmospheric Emitted Radiance Interferometer (AERI). *J. Appl. Meteor.*, **37**, 857-875.

Frisch, A. S., C. W. Fairall, and J. B. Snider, 1995: Measurements of stratus cloud and drizzle parameters in ASTEX with a Ka-band Doppler radar and microwave radiometer. *J. Atmos. Sci.*, **52**, 2788-2799.

Fu, Q., P. Yang, and W.B. Sun, 1998: An accurate parameterization of the infrared radiative properties of cirrus clouds for climate models. *J. Climate*, **11**, 2223-2237.

Garrett, T.J., L.F. Radke, and P.V. Hobbs, 2002: Aerosol effects on cloud emissivity and surface longwave heating in the Arctic. J. Atmos. Sci., 59, 769-778.

Girard, E., and J.-P. Blanchet, 2001: Simulation of Arctic diamond dust, ice fog, and thin stratus using an explicit aerosol-cloud-radiation model. *J. Atmos. Sci.*, **58**, 1199-1221.

Grant, E.H., J. Buchanan, and H.F. Cook, 1957: Dielectric behavior of water at microwave frequencies. *J. Chem. Phys.*, **26**, 156-161.

Gregory, D., and D. Morris, 1996: The sensitivity to climate simulations to the specification of mixed phase clouds. *Climate Dynamics*, **12**, 641-651.

Grenfell, T.C., and S.G. Warren, 1999: Representation of a nonspherical ice particle by a collection of independent spheres for scattering and absorption of radiation. *J. Geophys. Res.*, **104**, 31697-31709.

Guichard, F., D. Parsons, and E. Miller, 2000: Thermodynamic and radiative impact of the correction of sounding humidity bias in the tropics. *J. Climate*, **13**, 3615-3624.

Han, Y., J.B. Snider, E.R. Westwater, S.H. Melfi, and R.A. Ferrare, 1994: Observations of water vapor by ground-based microwave radiometers and Raman lidar. *J. Geophys. Res.*, **99**, 18695-18702.

Han, Y., J.A. Shaw, J.H. Churnside, P.D. Brown, and S.A. Clough, 1997: Infrared spectral measurements in the tropical Pacific atmosphere. *J. Geophys. Res.*, **102**, 4353-4356.

Harrington, J.Y., T. Reisin, W.R. Cotton, and S.M. Kreidenweis, 1999: Cloud resolving simulations of Arctic stratus. Part II: Transition-season clouds. *Atmos. Res.*, **51**, 45-75.

Herman, G.F., 1980: Thermal radiation in Arctic stratus clouds. *Quart. J. Roy. Meteor. Soc.*, **106**, 771-780.

Herman, G.F., and J.A. Curry, 1984: Observational and theoretical studies of solar radiation in Arctic stratus clouds. *J. Climate Appl. Meteor.*, **23**, 5-24.

Hobbs, P.V., A.L. Rangno, M. Shupe, and T. Uttal, 2001: Airborne studies of cloud structures over the Arctic Ocean and comparisons with retrievals from ship-based remote sensing measurements. *J. Geophys. Res.*, **106**, 15029-15044.

Hu, Y.X., and K. Stamnes, 1993: An accurate parameterization of the radiative properties of water clouds suitable for use in climate models. *J. Climate*, **6**, 728-742.

Huang, H.-L., X. Wu, J. Li, P. Antonelli, R.O. Knuteson, E.R. Olson, K.C. Baggett, and B.J. Osborne, 2001: Simultaneous retrievals of cloud height and emissivity from hyperspectral radiance measurements. Preprints, *Eleventh Conf. Sat. Meteor. Ocean.*, Madison, WI, American Meteorological Society.

Huang, H-.L., W.L. Smith, J. Li, P. Antonelli, X. Wu, R.O. Knuteson, B. Huang, and B.J. Osborne, 2002: Minimum local emissivity variance retrieval of cloud altitude and emissivity spectrum: simulation and initial verification. *J. Appl. Meteor.*, accepted.

Iacono, M.J. E.J. Mlawer, S.A. Clough, and J.-J. Morcrette, 2000: Impact of an improved longwave radiation model, RRTM, on the energy budget and thermodynamic properties of the NCAR community climate model CCM3. *J. Geophys. Res.*, **105**, 14873-14890.

Intrieri, J.M., M.D. Shupe, T. Uttal, and B.J. McCarty, 2002: An annual cycle of Arctic cloud characteristics observed by radar and lidar at SHEBA. *J. Geophys. Res.*, **107** (C10), 8030, doi:10.1029/2000JC000423.

IPCC, 1992: *Climate change 1992: The supplementary report of the IPCC scientific assessment.* Intergovernmental Panel on Climate Change. WMO/UNEP, Cambridge University Press, 200 pp.

Jayaweera, K.O.L.F., and T. Ohtake, 1973: Concentration of ice crystals in Arctic stratus clouds. *J. Rech. Atmos.*, **7**, 199-207.

Jiang, H., W.R. Cotton, J.O. Pinto, J.A. Curry, and M.J. Weissbluth, 2000: Cloud resolving simulations of a mixed-phase Arctic stratus observed during BASE: Sensitivity to concentration of ice crystals and large-scale heat and moisture advection. *J. Atmos. Sci.*, **57**, 2105-2117.

Key, J.R., and J.M. Intrieri, 2000: Cloud particle phase determination with the AVHRR. *J. Appl. Meteor.*, **39**, 1797-1804.

Knap, W.H., P. Stammes, and R.B.A. Koelemeijer, 2002: Cloud thermodynamic-phase determination from near-infrared spectra of reflected sunlight. *J. Atmos. Sci.*, **59**, 83-96.

Knuteson, R.O., B. Whitney, H.E. Revercomb, and F.A. Best, 1999: The history of the Atmospheric Emitted Radiance Interferometer (AERI) prototype during the period April 1994 through July 1995. DOE Tech. Memo. ARM TR-001.1. Available from http://www.arm.gov/docs/ documents/tech_reports/TR-001/TR-001.1.pdf.

Knuteson, R.O., H.E. Revercomb, F.A. Best, N.C. Ciganovich, R.G. Dedecker, T.P. Dirkx, S. Ellington, W.F. Feltz, R.K. Garcia, R.A. Herbsleb, H.B. Howell, W.L. Smith, J.F. Short, D.C. Tobin, and D.D. Turner, 2003: Atmospheric Emitted Radiance Interferometer (AERI): a ground-based Fourier transform spectrometer to measure downwelling infrared radiance. *J. Atmos. Oceanic Technol.*, to be submitted.

Koptev, A.P., and A.I. Voskresenskii, 1962: On the radiation properties of clouds. *Proc. Arctic and Antarctic Res. Inst.*, **293**, 39-47.

Lawson, R.P., B.A. Baker, C.G. Schmitt, and T.L. Jensen, 2001: An overview of microphysical properties of Arctic clouds observed in May and July 1998 during FIRE.ACE. *J. Geophys. Res.*, **106**, 14989-15014.

Liebe, H.J., and D.H. Layton, 1987: Millimeter wave properties of the atmosphere: laboratory studies and propagation modeling. *NTIA Rep. 87-24*, 74 pp. Natl. Telecommun. And Inf. Admin., Washington, D.C.

Liebe, H.J., G.A. Hufford, and T. Manabe, 1991: A model for the complex permittivity of water at frequencies below 1 THz. *Int. J. Infrared Millimeter Waves*, **12**, 659-675.

Liljegren, J.C. and B.M. Lesht, 1996: Measurements of integrated water vapor and cloud liquid water from microwave radiometers at the DOE ARM cloud and radiation testbed in the U.S. southern great plains. *Proceedings of the International Geoscience and Remote Sensing Symposium (IGARSS)*, Lincoln, NB, 1675-1677.

Liljegren, J.C., 2000: Automatic self-calibration of the ARM microwave radiometers. *Microwave Radiometry and Remote Sensing of the Environment*, P. Pampaloni, ed. VSP Press. Also available from http://www.arm.gov/docs/instruments/publications/mwr_calibration.pdf.

Lindzen, R.S., 1990: Some coolness concerning global warming. *Bull. Amer. Meteor. Soc.*, **71**, 288-299.

Lindzen, R.S., 1997: Can increasing carbon dioxide cause climate change? *Proc. Natl. Acad. Sci.*, **94**, 8335-8342.

Luther, F., Ed., 1984: The intercomparison of radiation codes in climate models. World Climate Program Rep. WCP-93, World Meteorological Organization, Geneva, Switzerland, 37 pp. [Available from World Meteorological Organization, 41 avenue Giuseppe Motta, Case postale N° 2300, CH-1211 Geneva 2, Switzerland.]

Luther, F., R.G. Ellingson, Y. Fouquart, S. Fels, N. Scott, and W. Wiscombe, 1988: Intercomparison of radiation codes in climate models (ICRCCM): Longwvae clear-sky results. *Bull. Amer. Meteor. Soc.*, **69**, 40-48.

Mahesh, A., V.P. Walden, and S.G. Warren, 2001: Ground-based infrared remote sensing of cloud properties over the Antarctic plateau: Part II: Cloud optical depths and particle sizes. *J. Appl. Meteor.*, **40**, 1279-1294.

Matrosov, S.Y., 1999: Retrievals of vertical profiles of ice cloud microphysics from radar and IR measurements using tuned regressions between reflectivity and cloud parameters. *J. Geophys. Res.*, **104**, 16,741-16,753.

Matrosov S.Y., A.V. Korolev, and A.J. Heymsfield, 2002: Profiling cloud ice mass and particle characteristic size from Doppler radar measurements. *J. Atmos. Oceanic Technol.*, **19**, 1003-1018.

Maxwell, J.B, 1982: Climate of the Canadian Arctic islands and adjacent water. *Climatol. Stud.*, **30**, 34-52.

Mie, G., 1908: Beiträge zur optik trüber medien speziell kolloidaler metallösungen. Ann. Phys., 25, 377-445.

Miller, N.E., J.C. Liljegren, T.R. Shippert, S.A. Clough, and P.D. Brown, 1994: Quality measurement experiments within the Atmospheric Radiation Measurement program. Proceedings of the 4th Atmospheric Radiation Measurement (ARM) science team meeting. Available from http://www.arm.gov/docs/documents/technical/conf_9403/04_94.pdf.

Miller, E.R., and K. Beierle, 2000: SHEBA GLASS sounding data. SHEBA data archive at JOSS home page. Available at http://www.ofps.ucar.edu/sheba/sndg_correction.

Minnett, P.J., R.O. Knuteson, F.A. Best, B.J. Osborne, J.A. Hanafin, and O.B. Brown, 2001: The marine-atmospheric emitted radiance interferometer: a high-accuracy, seagoing infrared spectrometer. *J. Atmos. Oceanic Technol.*, **18**, 994-1013.

Mishchenko, M.I., J.W. Hovenier, and L.D. Travis, editors, 1999: *Light scattering by nonspherical particles: theory, measurements, and applications*. Academic Press, San Diego.

Mitchell, J.F.B., and W.J. Ingram, 1989: Carbon dioxide and climate: Mechanisms of changes in cloud. *J. Climate*, **5**, 5-21.

Mitchell, D.L., 2002: Effective diameter in radiation transfer: general definition, applications, and limitations. *J. Atmos. Sci.*, **59**, 2330-2346.

Mlawer, E.J., S.J. Taubman, P.D. Brown, M.J. Iacono, and S.A. Clough, 1997: RRTM, a validated correlated-k model for the longwave. *J. Geophys. Res.*, **102**, 16663-16682.

Moran, K.P., B.E. Martner, M.J. Post, R.A. Kropfli, D.C. Welsh, and K.B. Widener, 1998: An unattended cloud-profiling radar for use in climate research. *Bull. Amer. Meteor. Soc.*, **79**, 443-455.

Moss, S.J., and D.W. Johnson, 1993: Aircraft measurements to validate and improve numerical model parameterizations of ice to water ratios in cloud. *Atmos. Res.*, **34**, 1-25.

Nakamura, N., and A.H. Oort, 1988: Atmospheric heat budgets of the polar regions. *J. Geophys. Res.*, **93**, 9510-9524.

Ohtake, T., 1970: Unusual crystal in ice fog. *J. Atmos. Sci.*, **27**, 509-511.

Pilewskie, P., and S. Twomey, 1987a: Discrimination of ice from water in clouds by optical remote sensing. *Atmos. Res.*, **21**, 113-122.

Pilewskie, P., and S. Twomey, 1987b: Cloud phase discrimination by reflectance measurements near 1.6 and 2.2 μm. *J. Atmos. Sci.*, **44**, 3419-3421.

Pinto, J.O., 1998: Autumnal mixed-phase cloudy boundary layers in the Arctic. *J. Atmos. Sci.*, **55**, 2016-2038.

Pinto, J.O., J.A. Curry, and J.M. Intrieri, 2001: Cloud-aerosol interations during autumn over the Beaufort Sea. *J. Geophys. Res.*, **106**, 15077-15097.

Ramanathan, V., R.D. Cess, E.F. Harrison, P. Minnis, B.R. Barkstrom, E. Ahmad, and D. Hartmann, 1989: Cloud-radiative forcing and climate: Results from the Earth Radiation Budget Experiment. *Science*, **243**, 57-63.

Rangno, A.L., and P.V. Hobbs, 2001: Ice particles in stratiform clouds in the Arctic and possible mechanisms for the production of high ice concentrations. *J. Geophys. Res.*, **106**, 15065-15075.

Rauber, R.M., and A. Tokay, 1991: An explanation for the existence of supercooled liquid water at the top of cold clouds. *J. Atmos. Sci.*, **48**, 1005-1023.

Revercomb, H.E., H. Buijs, H.B. Howell, D.D. LaPorte, W.L. Smith, and L.A. Sromovsky, 1988: Radiometric calibration of the IR Fourier transform spectrometers: solution to a problem with the High-Resolution Interferometer Sounder. *Appl. Opt.*, **27**, 3210-3218.

Revercomb, H.E., F.A. Best, R.G. Dedecker, T.P. Dirkx, R.A. Herbsleb, R.O. Knuteson, J.F. Short, and W.L. Smith, 1993: Atmospheric Emitted Radiance Interferometer (AERI) for ARM. Preprints, *Fourth Symp. On Global Climate Change St*udies, Anaheim, CA, Amer. Meteor. Soc., 46-49.

Revercomb, H.E., D.D. Turner, D.C. Tobin, R.O. Knuteson, W.F. Feltz, J. Barnard, J. Bösenberg, S. Clough, D. Cook, R. Ferrare, J. Goldsmith, S. Gutman, R. Halthore, B. Lesht, J. Liljegren, H. Linné, J. Michalsky, V. Morris, W. Porch, S. Richardson, B. Schmid, M. Splitt, T. VanHove, E. Westwater, and D. Whiteman, 2003: The Atmospheric Radiation Measurement Program's water vapor intensive observation periods: Overview, initial accomplishments, and future challenges. *Bull. Amer. Meteor. Soc.*, **84**, 217-236.

Ridgway, W.L., Harshvardhan, and A. Arking, 1991: Computation of atmospheric cooling rates by exact and approximate methods. *J. Geophys. Res.*, **96**, 8969-8984.

Rodgers, C.D., 2000: *Inverse methods for atmospheric sounding*. World Scientific, Singapore, 238 pp.

Rosenberg, V.I., 1972: *Scattering and extinction of electromagnetic radiation by atmospheric particles*. In Russian, 348 pp. Gidrometeoizdat, St. Petersburg, Russia.

Rosenkranz, P.W., 1998: Water vapor microwave continuum absorption: A comparison between measurements and models. *Radio Sci.*, **33**, 919-928.

Rossow, W.B., and L.C. Garder, 1993: Validation of ISCCP cloud detections. *J. Climate*, **6**, 2370-2393.

Rossow, W.B., and R.A. Schiffer, 1999: Advances in understanding clouds from ISCCP. *Bull. Amer. Meteor. Soc.*, **80**, 2261-2287.

Rothman, L.S., and coauthors, 1998: The HITRAN molecular spectroscopic database and HAWKS (HITRAN Atmospheric Workstation): 1996 edition. *J. Quant. Spectros. Radiat. Transfer*, **60**, 665-710.

Rothman, L.S., and coauthors: 2003: The HITRAN Molecular Spectroscopic Database: Edition of 2000 Including Updates through 2001, submitted to J. Quant. Spectrosc. Rad. Transfer.

Sassen, K., 1991: The polarization lidar technique for cloud research: a review and current assessment. *Bull. Amer. Meteor. Soc.*, ***72**, 1848-1866.*

Sassan, K., and G.G. Mace, 2002: Ground-based remote sensing of cirrus clouds. *Cirrus*, D.K. Lynch, K. Sassen, D.O'C. Starr, and G. Stephens, Eds. Oxford University Press.

Schneider, E.K., B.P. Kirtman, and R.S. Lindzen, 1999: Tropospheric water vapor and climate sensitivity. *J. Atmos. Sci.*, **56**, 1649-1658.

Sekelsky, S. and R. McIntosh, 1996: Cloud observations with a polarimetric 33 GHz and 95 GHz radar. *Meteor. Atmos. Phys.*, **59**, 123-140.

Serreze, M.C., R.G. Barry, and J.E. Walsh, 1995: Atmospheric water vapor characteristics at 70°N. *J. Climate*, **8**, 719-731.

Shupe, M.D., T. Uttal, S.Y. Matrosov, and A.S. Frisch, 2001: Cloud water contents and hydrometeor sizes during the FIRE - Arctic Clouds Experiment. *J. Geophys. Res.*, **106**, 15,015-15,028.

Sinda, A., and J.E. Harries, 1997: The Earth's clear-sky radiation budget and water vapor absorption in the far infrared. *J. Climate*, **10**, 1601-1614.

Sirois, A., and L.A. Barrie, 1999: Arctic lower tropospheric aerosol trends and composition at Alert, Canada: 1980-1995. *J. Geophys. Res.*, **104**, 11599-11618.

Smith, W.L., and R. Frey, 1990: On cloud altitude determinations from high resolution interferometers sounder (HIS) observations. *J. Appl. Meteor.*, **29**, 658-662.

Smith, W.L., R.O. Knuteson, H.E. Revercomb, F. Best, R. Dedecker, and H.B. Howell, 1993a: GB-HIS: a measurement system for continuous profiling of the boundary layer thermodynamic structure. Preprints, *Eighth Symp. Meteor. Obs and Instr.*, Anaheim, CA, Amer. Meteor. Soc., J180-J183.

Smith, W.L., X.L. Ma, S.A. Ackerman, H.E. Revercomb, and R.O. Knuteson, 1993b: Remote sensing cloud properties from high spectral resolution infrared observations. *J. Atmos. Sci.*, **50**, 1708-1720.

Smith, W.L., S. Ackerman, H. Revercomb, H. Huang, D.H. DeSlover, W. Feltz, L. Gumley, and A. Collard, 1998: Infrared spectral absorption of nearly invisible cirrus clouds. *Geophys. Res. Lett.*, **25**, 1137-1140.

Smith, W.L., W.F. Feltz, R.O. Knuteson, H.E. Revercomb, H.M. Woolf, and H.B. Howell, 1999: The retrieval of planetary boundary layer structure using ground-based infrared spectral radiance measurements. *J. Atmos. Oceanic Technol.*, **16**, 323-333.

Stamnes, K., S.-C. Tsay, W. Wiscombe, and K. Jayaweera, 1988: A numerically stable algorithm for discrete-ordinate-method radiative transfer in multiple scattering and emitting layered media. *Appl. Opt.*, **27**, 2502-2509.

Stamnes, K., R.G. Ellingson, J.A. Curry, J.E. Walsh, and B.D. Zak, 1999: Review of science issues, deployment strategy, and status of the ARM North Slope of Alaska-Adjacent Arctic Ocean climate research site. *J. Climate*, **12**, 46-63.

Stokes, G.M., and S.E. Schwartz, 1994: The Atmospheric Radiation Measurement (ARM) program: programmatic background and design of the cloud and radiation testbed. *Bull. Amer. Meteor. Soc.*, **75**, 1201-1221.

Strabala, K.I., S.A. Ackerman, and W.P. Menzel, 1994: Cloud properties inferred from 8-12 mm data. *J. Appl. Meteor.*, **2**, 212-229.

Sun, Z., and K.P. Shine, 1995: Parameterization of ice cloud radiative properties and its application to the potential climatic importance of mixed-phase clouds. *J. Climate*, **8**, 1874-1888.

Tao, X., J.E. Walsh, and W.L. Chapman, 1996: An assessment of global climate model simulations of arctic air temperatures. *J. Climate*, **9**, 1060-1076.

Thompson, S.L., and D. Pollard, 1997: Greenland and Antarctic mass balances for present and doubled atmospheric CO2 from the GENESIS version 2 global climate model. *J. Climate*, **10**, 871-900.

Tobin, D.C., F.A. Best, P.D. Brown, S.A. Clough, R.G. Dedecker, R.G. Ellingson, R.K. Garcia, H.B. Howell, R.O. Knuteson, E.J. Mlawer, H.E. Revercomb, J.F. Short, P.F.W. van Delst, and V.P. Walden, 1999a: Downwelling spectral radiance observations at the SHEBA ice station: water vapor continuum measurements from 17 to 26 mm. *J. Geophys. Res.*, **104**, 2081-2092.

Tobin, D.C., H.E. Revercomb, R.O. Knuteson, W.F. Feltz, and F.J. Murcray, 1999b: Weak water vapor spectral lines in the 8-12 μm atmospheric window. Proc. 9th Atmospheric Radiation Measurement (ARM) Science Team Meeting, San Antonio, TX. Available online at http://www.arm.gov/docs/documents/technical/conf_9903/tobin-99.pdf.

Tobin, D.C., R.O. Knuteson, and H.E. Revercomb, 2000: Observed and calculated downwelling longwave spectral radiances at the SHEBA ice station: prelude to an Arctic AERI/LBLRTM QME. Proc. 10th Atmospheric Radiation Measurement (ARM) Science Team Meeting, San Antonio, TX. Available online at http://www.arm.gov/docs/documents/technical/conf_0003/tobin-dc.pdf.

Turner, D.D., B.M. Lesht, S.A. Clough, J.C. Liljegren, H.E. Revercomb, and D.C. Tobin, 2003a: Dry bias and variability in Vaisala radiosondes: The ARM experience. *J Atmos. Oceanic Technol.*, **20**, 117-132.

Turner, D.D., D.C. Tobin, S.A. Clough, P.D. Brown, R.G. Ellingson, M.J. Mlawer, R.O. Knuteson, H.E. Revercomb, T.R. Shippert, W.L. Smith, and M.W. Shephard, 2003b: The QME AERI LBLRTM: A closure experiment for downwelling high spectral resolution infrared radiance. *J. Climate*, submitted.

Turner, D.D., S.A. Ackerman, B.A. Baum, H.E. Revercomb, and P. Yang, 2003c: Cloud phase determination using ground-based AERI observations at SHEBA. *J. Appl. Meteor.*, **42**, 701-715.

Twomey, S., 1977: *Atmospheric aerosols*. Elsevier Scientific Pub. Co., New York, 302 pp.

Uttal, T., and coauthors, 2002: Surface heat budget of the Arctic Ocean. *Bull. Amer. Meteor. Soc.*, **83**, 255-275.

Vavrus, S., 2003: The impact of cloud feedbacks on Arctic climate change forced by increased CO2. *Preprints, 7th Conf. Polar Meteor. Oceanography*. Hyannis, MA, Amer. Meteor. Soc.

Verlinde, H., 2003: Mixed-phase Arctic clouds experiment (M-PACE): Executive summary. Available from http://www.meteo.psu.edu/~verlinde/mpace.html.

Wang, J., H.L. Cole, D.J. Carlson, E.R. Miller, and K. Beierle, 2002: Corrections of humidity measurement errors from the Vaisala RS80 radiosonde – application to TOGA COARE data. *J. Atmos. Oceanic Technol.*, **19**, 981-1002.

Wang, X., and J.R. Key, 2003: Recent trends in Arctic surface, cloud, and radiation properties from space. *Science*, **299**, 1725-1728.

Warren, S., 1984: Optical constants of ice from the ultraviolet to the microwave. *Appl. Opt.*, **23**, 1206-1225.

Welch, R.M., S.K. Cox, and J.M. Davis, 1980: Solar radiation and clouds. Meteorological Monographs, Vol 17, No 39, 96 pp. Amer. Meteor. Soc.

Westwater, E.R., Y. Han, M.D. Shupe, and S.Y. Matrosov, 2001: Analysis of integrated cloud liquid and precipitable water vapor retrievals from microwave radiometers during the Surface Heat Budget of the Arctic Ocean Project. *J. Geophys. Res.*, **106**, 32019-32030.

Wetherald, R.T., and S. Manabe, 1988: Cloud feedback processes in a general circulation model. *J. Atmos. Sci.*, **45**, 1397-1415.

Witte, H.J., 1968: Airborne observations of cloud particles and infrared flux density in the Arctic. MS Thesis, 102 pp., Dept. of Atmos. Sci., University of Washington, Seattle, Washington.

Wiscombe, W.J., 1976: Extension of the doubling method to inhomogeneous sources. *J. Quant. Sepctrosc. Radiat. Transfer*, **16**, 477-489.

Wiscombe, W.J., 1980: Improved Mie scattering algorithms. *Appl. Opt.*, **19**, 1505-1509.

Yang, P., and K.N. Liou, 1996: Geometric-optics-integral-equation method for light scattering by nonspherical ice crystals. *Appl. Opt.*, **35**, 6568-6584.

Yang, P., K.N. Liou, M.I. Mishchenko, and B.C. Gao, 2000: Efficient finite-difference time-domain scheme for light scattering by dielectric particles: application to aerosols. *Appl. Opt.*, **39**, 3727-3737.

Yang, P., B.C. Gao, B.A. Baum, Y.X. Hu, W.J. Wiscombe, S.C. Tsay, D.M. Winker, and S.L. Nasiri, 2001: Radiative properties of cirrus clouds in the infrared (8-13 μm) spectral region. *J. Quant. Spect. Rad. Trans.*, **70**, 473-504.

Yang, P., H.-L. Wei, B.A. Baum, H.-L. Huang, A.J. Heymsfield, Y.X. Hu, B.-C. Gao, and D.D. Turner, 2003a: The spectral signature of mixed-phase clouds composed of non-spherical ice crystals and spherical liquid water droplets in terrestrial window region. *J. Quant, Spect. Rad. Transfer*, **79-80**, 1171-1188.

Yang, P., B.A. Baum, A.J. Heymsfield, Y.X. Hu, H.-L. Huang, S.-C. Tsay, and S.A. Ackerman, 2003b: Single-scattering properties of droxtals. *J. Quant. Spect. Rad. Transfer*, **79-80**, 1159-1169.

Yang, P., M.G. Mlynczak, H.-L. Wei, D.P. Kratz, B.A. Baum, Y.X. Hu, W.J. Wiscombe, A. Heidinger, and M.I. Mishchenko, 2003c: Spectral signature of cirrus clouds in the far-infrared region: Single scattering calculations and radiative sensitivity study. Submitted to *J. Geophys. Res.*

†